Ph.D DISSERTATION

# A STUDY ON MICROWAVE ACTIVE INTEGRATED PROBES APPLICABLE TO CANCER DETECTION AND TREATMENT

암 진단 및 치료에 적용 가능한 마이크로파 능동 집적 탐침에 관한 연구

BY

KIHYUN KIM

FEBRUARY 2015

SCHOOL OF ELECTRICAL ENGINEERING AND

COMPUTER SCIENCE COLLEGE OF ENGINEERING

SEOUL NATIONAL UNIVERSITY

# Abstract

This thesis presents miniaturized microwave active integrated probe systems applicable to cancer detection and treatment. To realize broadband detection and low-power hyperthermia, planar-type coaxial probes and heat applicators have been integrated with active circuits for permittivity measurement and microwave generation, respectively. Each integrated system is implemented on a single platform using Microelectromechanical Systems (MEMS) and monolithic microwave integrated circuit (MMIC) technologies for miniaturization and integration.

First, a complex permittivity measurement technique using an integrated multi-state reflectometer (MSR) is proposed for cancer detection application. The broadband MSR covering both 2 and 16 GHz bands consists of a dual-band phase-locked loop, a directional coupler, an impedance tuner, two RF power detectors, and a micromachined silicon planar probe with an open-ended coaxial aperture. All the active and passive circuit components have been integrated on the micromachined probe platform in a small form factor of 6.8 mm × 50 mm × 0.6 mm. The performance of the fabricated integrated probe has been evaluated by comparing the measured permittivities of 0.9% saline, pork muscle, fat, and xenografted human breast cancer with the reference data.

For low-power microwave hyperthermia, a *Ku*-band active integrated heat

applicator is demonstrated. A planar-type coaxial applicator has been fabricated using silicon micromachining technology, on which a *Ku*-band voltage controlled oscillator (VCO), a driver amplifier, and a power amplifier (PA) have been integrated. A directional coupler and power detectors are employed for power monitoring. The fully integrated heat applicator has been realized in a small footprint of 8 mm × 56 mm. *In-vitro* and *in-vivo* ablation experiments on pork muscle, fat, and human-cancer xenografted nude mouse demonstrate the feasibility of low-power hyperthermia using *Ku*-band microwaves.

Finally, an active integrated heat applicator for magnetic nanoparticle (MNP)-assisted hyperthermia is developed. The effect of the MNP on microwave hyperthermia has been analyzed by a coupled electromagnetic-thermal analysis. The optimum frequency for hyperthermia is determined by the coupled analysis. A 2-GHz source module consisting of a VCO and a PA has been implemented in MMIC's and integrated on the heat applicator platform. A dual-channel log detector and a directional coupler have been also employed to monitor the power levels during hyperthermia. Experiment results show not only sufficient heating performance of the integrated applicator, but also the effectiveness of the MNP for low-power and cancer-specific microwave hyperthermia.

# Contents

# List of Figures

xi

xii

# List of Tables

# Chapter 1

# Introduction

## 1.1    Motivation

Cancer is a major cause of mortality and morbidity throughout the world. Despite extensive efforts to conquer cancer, the survival rate of patients has not been significantly improved. For this reason, various researches on alternative methods have been conducted to achieve accurate diagnosis and appropriate treatment. Among the alternative methods, microwave cancer detection and ablation have recently attracted much attention due to cost-effectiveness, ease of use, and high sensitivity [1], [2]. The microwave methods are based on the fact that cancerous and normal tissues have an obvious difference in their electromagnetic properties [3], [4]. It has been shown in [1] and [5] that broadband electrical parameters, such as relative permittivity, conductivity, and relaxation frequency, can be effectively used

to detect small-size breast cancers. Also, shown in [6] is the possibility of low-power hyperthermia using *Ku*-band microwaves.

The microwave methods for diagnostic or therapeutic purposes can be categorized into invasive (interstitial) and noninvasive ones. In the invasive method, microwave is delivered through a probe or applicator inserted into the tumor. On the other hand, the noninvasive method is generally achieved by multiple applicators or antennas that transmit microwave energy from the outside of the body. Even though the noninvasive method offers advantages such as lack of pain and discomfort during operation, the excessive path loss of the human body at microwave frequencies sets the fundamental limit. The quality of detected electromagnetic information could be significantly degraded, thus decreasing the diagnostic accuracy of cancer detection. In addition, during treatments with noninvasive applicators, it is difficult to treat deep-seated small tumors without overheating the surrounding healthy tissues since microwave field cannot be precisely focused through a lossy medium of tissue. As a result, the invasive method presents advantages in comparison to the noninvasive one with regard to localized detection and treatment, and minimal normal tissue damage.

For minimally invasive detection and treatment, the probe or applicator should be implemented in a small form factor, which is possible by employing miniaturization and integration techniques. Further reduction in the overall size and,

2

more importantly, the cost of the system can be achieved by co-integrating the probe or applicator, and active circuits on the same platform. Active integrated systems eliminate the need for external cables, thereby reducing the path loss between the signal source and target tissue, and offer additional benefits such as portability and ease of use. In this research, active integrated probes applicable to cancer detection and treatment are investigated for the minimally invasive microwave methods.

## 1.2    Microwave Cancer Detection

There have been various studies to apply microwaves to a cancer diagnostic system, which are based on the distinct dielectric properties of malignant tumors. A near-field microwave imaging method using the frequency of 700 MHz was proposed to detect relatively large tumors (~ 1 cm) [7]. A clinical prototype of a microwave imaging system was developed and applied to breast cancer patients [8]. Despite the efforts, the microwave method for practical clinical application has still a number of limitations in terms of spatial resolution and accuracy.

Based on the broadband characterization of dielectric properties, metastasized breast cancer cells in lymph nodes rather than bulk cancer tissues were accurately detected using microwaves in the frequency range from 0.5 to 30 GHz [5]. Although this study showed the possibility of the microwave detection of small-sized cancer, the proposed method lacks practicality due to the requirement of a broadband vector network analyzer (VNA). This shortcoming can be overcome by adopting a scalar measurement-based reflectometer with a relatively simple configuration.

## 1.3    Microwave Hyperthermia

Microwave hyperthermia is a treatment procedure in which the target tissue temperature is elevated to the range of 43-45 °C [9]. The key mechanism for microwave hyperthermia is based on the fact that electromagnetic waves absorbed by biological tissues are transformed into heat energy by increased kinetic energy of the absorbing molecules. So far, microwave hyperthermia has been performed using low-frequency bands, i.e. ISM (Industry, Scientific, Medical) bands (433 MHz, 900 MHz, and 2.4 GHz) [10]-[13]. Due to the inherent low heating efficiency, high microwave power of several tens of watts is required to achieve the desired amount of thermal dose for successful treatment. These high-power hyperthermia systems utilize the heat applicators in the form of three-dimensional structures, and require bulky external microwave sources, thus increasing the cost and size of the system.

To mitigate these limitations, low-power microwave hyperthermia has been investigated using less than a few watts in the frequency range of 15-20 GHz, where the dielectric loss shows the highest contrast between the cancerous and normal tissues [6], [14]. The short wavelength helps to reduce the size of the applicator as well as to achieve localized heating with low collateral damage. The use of low power allows one to realize the microwave sources in the form of monolithic microwave integrated circuits (MMIC's), which can be integrated together with the applicator. The advantages of low-power microwave hyperthermia can be enhanced

by using magnetic nanoparticles (MNP's) [15]. The MNP improves microwave power absorption in cancer cells due to its magnetic loss, thereby increasing the heating efficiency and material sensitivity during hyperthermia therapy. This would allow further reduction in the microwave source power. However, there have been few detailed reports on the effect of the MNP's on microwave hyperthermia and their dependence on the frequency spectrum.

## 1.4 Outline of Thesis

The main objective of this thesis is to demonstrate miniaturized microwave active integrated probe systems applicable to cancer detection and treatment. For this purpose, coaxial probes for complex permittivity measurement and heat applicators for cancer ablation are implemented in a two-dimensional planar structure. Microwave active circuits are fabricated using MMIC technology for system miniaturization, and integrated on the probe and applicator platforms.

In chapter 2, an active integrated probe for permittivity measurement is presented. To reduce the system complexity caused by the vector measurement, a complex permittivity measurement technique using a multi-state reflectometer (MSR) based on scalar power measurement is proposed. The active integrated probe is realized by integrating the MSR on the micromachined probe. The validity of the integrated probe is verified by comparing the measured complex permittivities of 0.9% saline, pork muscle, fat, and human breast cancer with the reference values.

In chapter 3, a *Ku*-band active integrated heat applicator for cancer ablation is demonstrated. A *Ku*-band source module and power detectors are integrated on the micromachined applicator platform. The feasibility of low-power hyperthermia using *Ku*-band microwaves is validated in the thermal ablation experiments on pork muscle, fat, and human-cancer xenografted nude mouse.

In chapter 4, an active integrated heat applicator for MNP-assisted hyperthermia is presented. To enhance heating efficiency and material sensitivity, MNP is employed in microwave hyperthermia. A coupled electromagnetic-thermal analysis is proposed to investigate the effect of the MNP's on microwave hyperthermia and to find the optimum frequency for MNP-assisted hyperthermia. The integrated applicator is developed by integrating a microwave source and power monitoring circuits on a spiral heat applicator. Experiment results show not only sufficient heating performance of the integrated applicator, but also the effectiveness of MNP's for low-power and cancer-specific microwave hyperthermia.

# Chapter 2

# Active Integrated Probe for Cancer Detection

## 2.1    Introduction

Recently, cancer detection using microwaves has attracted much attention as a cost-effective and simple alternative diagnostic method [5], [16], [17]. These studies are based on the fact that there is large contrast in the electromagnetic properties, i. e., broadband complex permittivities, between cancerous and normal tissues [3], [4]. It has been shown in [1] and [5] that the electrical parameters, such as relative permittivity, conductivity, and relaxation frequency, extracted at multiple frequency bands (1-2 GHz, 16-18 GHz) can be effectively used to detect the breast cancers.

In general, the complex permittivity of biological material can be estimated from the reflection coefficients measured using a vector network analyzer (VNA).

9

However, since VNA is a general-purpose test system with a capability of high-resolution vector measurement over a wide frequency bandwidth, it is very expensive and bulky, making miniaturization almost impossible. The purpose of this work is to demonstrate an active integrated probe system to measure the permittivity of biological material. One potential application may be a hand-held cancer detection device that can be used inside the operation room.

To avoid the system complexity caused by the vector measurements, a reflectometer based on scalar power measurement has attracted extensive interest [18], [19]. The reflectometer measures S-parameters based on the power readings of the incident and scattered waves through its multi-port or multi-state network. A number of six-port reflectometers have been reported, yielding promising results over various frequency ranges [20]-[24]. However, since they are based on the fixed passive components, they show limited accuracy to cover wide frequency and impedance ranges to be effectively used for broadband cancer detection. Also, no attempts have been made to develop an integrated system using this approach, where the reflectometers are integrated with the probes and the detection circuits. In this work, multi-state reflectometer (MSR) approach [19] has been employed to demonstrate a fully integrated probe system. Compared with a multi-port reflectometer using fixed passive networks, MSR can offer better accuracy over a wide frequency since the active reconfigurable network can transform the material

impedances to the optimum values for each frequency point. It also lends itself to easy integration in a small form factor since it requires fewer number of bulky directional couplers and power detectors.

The accuracy of the permittivity measurement heavily depends on the choice of the probe structure. Open-ended coaxial probes have been widely used for the biological material due to their broadband and nondestructive nature [25], [26]. To warrant integration with the planar active circuits, various planar-type coaxial probes have been proposed [27], [28]. The introduction of micromachining technology in [29] allowed the fabrication of a planar coaxial probe with fine precision, which helped extend the frequency bandwidth. In this work, we have used microelectromechanical systems (MEMS) approach to demonstrate a miniaturized MSR system integrated on the planar coaxial probe platform. Based on the work of [1] and [5], which demonstrated high-accuracy breast cancer detection using the permittivity information at 2 and 16 GHz, the MSR is designed to operate in two sub-bands. This is made possible by integrating dual-band phase-locked loop (PLL). The rest of the components, such as directional coupler, impedance tuner, power detector, and probe, are designed to cover the entire frequency range from 2 to 16 GHz. The fully integrated MSR including all the RF components is realized in a small form factor of 6.8 mm × 50 mm × 0.6 mm, which is less than a fraction of the size of VNAs or reflectometers reported to date. To the best of our knowledge, this is

11

the first demonstration of an active integrated broadband reflectometer for complex permittivity measurement of biological material.

The operation principle of the proposed active integrated probe for complex permittivity measurement is illustrated in section 2.2 followed by the design and fabrication of each circuit component in section 2.3. Experimental verification of the integrated probe is presented in section 2.4.

## 2.2 Principle of Operation

The simplified block diagram of the proposed MSR integrated on a probe platform is shown in Fig. 2.1. The MSR is a reconfigurable four-port network as depicted by the dashed box, which consists of a directional coupler, an impedance tuner, and two RF power detectors, all integrated on MEMS probe platform with an open-ended coaxial aperture. It is similar in concept to a conventional MSR for impedance measurement [19], but is an advanced implementation in that the measurement ports are integrated in MSR. Since the active integrated probe system does not require external cabling and connections, the entire system stays intact through various calibration and measurement steps, which helps to enhance the overall measurement accuracy.
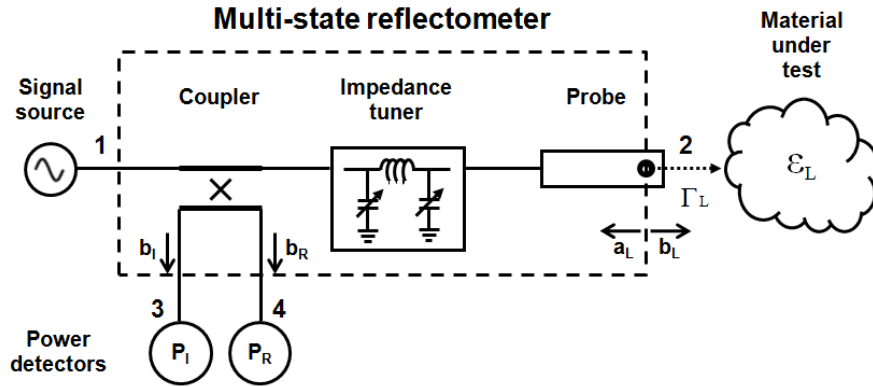


Fig. 2.1 Block diagram of the proposed multi-state reflectometer integrated on the probe platform.

## 2.2.1  Multi-State Reflectometer

An RF signal fed into port 1 is delivered to material under test (MUT) at port 2 through the four-port network, and the power detectors at port 3, 4 measure the coupled waves ($b_I$, $b_R$). With an analogy to a six-port reflectometer analysis, the detected power readings can be expressed as a linear combination of the incident wave, $b_L$ and the reflected wave, $a_L$, at port 2. Thus, the operation of the MSR in a particular state $k$ can be described by the following bilinear equation [19]:

$$\frac{P_R^{(k)}}{P_I^{(k)}} = g^{(k)} \left| \frac{1 + A^{(k)} \cdot \Gamma_L}{1 + B^{(k)} \cdot \Gamma_L} \right|^2 \quad (k = 1, 2, \cdots, n) \tag{2.1}$$

where $k$ is the state identifier of the four-port network set by the impedance tuner, and $A^{(k)}$, $B^{(k)}$, and $g^{(k)}$ are system constants of the MSR to be determined through a calibration. $\Gamma_L$ denotes the reflection coefficient of the MUT seen at the aperture of the probe, and $P_I^{(k)}$, $P_R^{(k)}$ are the measured scalar power readings at port 3 and 4, respectively.

As generally understood, the locus of $\Gamma_L$ in equation (2.1) represents a circle on the Smith chart. Hence, the intersection point of the loci for more than three states corresponds to the reflection coefficient. However, to estimate the permittivity of MUT from the extracted $\Gamma_L$, one needs to find the relationship between $\varepsilon_L$ and $\Gamma_L$.

Since the admittance ($Y_L$) at the probe aperture is a function of the aperture size of the probe as well as of the permittivity of MUT, the problems involve multi-dimensional integration as shown below [30]:

$$Y_L = j \frac{2\kappa^2}{\omega\mu_0 \left[\ln(b/a)\right]^2} \int_a^b \int_a^b \int_0^\pi \cos\phi' \frac{e^{-j\kappa r}}{r} d\phi' d\rho' d\rho$$

$$\kappa = \omega\sqrt{\mu_0 \varepsilon_L} , \; r = [\rho^2 + \rho'^2 - 2\rho\rho'\cos\phi']^{1/2} \tag{2.2}$$

where $a$ and $b$ are the inner and outer radii of the coaxial aperture, respectively.

## 2.2.2  Governing Equation for Complex Permittivity

To constitute a governing equation for permittivity measurement, it is necessary to review the relationship between the reflection coefficient at the probe aperture and the complex permittivity of the MUT. The probe-MUT interface impedance can be modelled as a simple capacitor since the radiation effect can be neglected due to the small aperture size of the micromachined probe. The load impedance at the probe interface, $Z_L$, can then be expressed as follows [27], [31], [32]:

$$Z_L(\omega,\varepsilon) \cong \left[j\omega\, C_f(\omega) + j\omega C(\omega,\varepsilon)\right]^{-1}$$

$$= \left[j\omega\, C_f(\omega) + j\omega\varepsilon C_0(\omega)\right]^{-1} \tag{2.3}$$

15

where $C_f(\omega)$ is the fringing field capacitance inside the probe, which is thus independent of the MUT, and $\varepsilon C_0(\omega)$ represents the fringing field through the MUT. Since the reflection coefficient of the MUT has bilinear relationship with its admittance, the complex permittivity of the MUT can also be expressed as a bilinear equation with the reflection coefficient [27], [32]:

$$\frac{(\varepsilon_L - \varepsilon_A)(\varepsilon_B - \varepsilon_C)}{(\varepsilon_L - \varepsilon_B)(\varepsilon_C - \varepsilon_A)} = \frac{(\Gamma_L - \Gamma_A)(\Gamma_B - \Gamma_C)}{(\Gamma_L - \Gamma_B)(\Gamma_C - \Gamma_A)} \tag{2.4}$$

where $\varepsilon_A$, $\varepsilon_B$, and $\varepsilon_C$ are the known complex permittivities of the three calibration materials, and $\Gamma_A$, $\Gamma_B$, and $\Gamma_C$ are the corresponding reflection coefficients to be measured during calibration process. Using equation (2.4), we can rewrite equation (2.1), and derive the governing equation of the MSR for complex permittivity [33] as

$$\frac{P_R^{(k)}}{P_I^{(k)}} = g^{(k)} \left| \frac{1 + A^{(k)} \cdot \varepsilon_L}{1 + B^{(k)} \cdot \varepsilon_L} \right|^2 \qquad (k = 1,\ 2,\ \cdots,\ n). \tag{2.5}$$

Here, $A^{(k)}$, $B^{(k)}$, and $g^{(k)}$ are new system constants of the MSR in a state $k$, which can be identified through calibration.

### 2.2.3 Determination of Complex Permittivity

The governing equation (2.5) can be rearranged with the complex variables, $\varepsilon_L$, $q^{(k)}$, and $r^{(k)}$ as

$$\left|\varepsilon_L - q^{(k)}\right|^2 = r^{(k)^2} \quad (k = 1, 2, \cdots, n). \tag{2.6}$$

$\varepsilon_L$, the complex permittivity, forms a circle at each state $k$, centered at $q^{(k)}$ with a radius $r^{(k)}$ similarly to that of six-port reflectometer [22]. $q^{(k)}$ and $r^{(k)}$ are given by

$$
\begin{aligned}
q^{(k)} &= \frac{P_R^{(k)} B^{(k)*} - P_I^{(k)} g^{(k)} A^{(k)*}}{P_I^{(k)} g^{(k)} \left|A^{(k)}\right|^2 - P_R^{(k)} \left|B^{(k)}\right|^2} \\
r^{(k)^2} &= \frac{P_I^{(k)} P_R^{(k)} g^{(k)} \left|A^{(k)} - B^{(k)}\right|^2}{\left[P_I^{(k)} g^{(k)} \left|A^{(k)}\right|^2 - P_R^{(k)} \left|B^{(k)}\right|^2\right]^2}.
\end{aligned}
\tag{2.7}
$$

Ideally, $\varepsilon_L$ can be found by drawing three circles with different states ($k$'s) and locating the intersection point. However, redundancy in the form of over-determined system is generally required due to the measurement errors. So, in this work, $n$ ($n \geq$ 3) circles are plotted in the complex permittivity plane and the point showing the smallest error defined by the sum of squared distance errors, $f(\varepsilon_L)$, is identified as $\varepsilon_L$,

such that

$$\frac{\partial f(\varepsilon_{\mathrm{L}})}{\partial \mathrm{Re}(\varepsilon_{\mathrm{L}})} = \frac{\partial f(\varepsilon_{\mathrm{L}})}{\partial \mathrm{Im}(\varepsilon_{\mathrm{L}})} = 0 \tag{2.8}$$

where $f(\varepsilon_{\mathrm{L}}) = \sum_{k=1}^{n} \left[ \left| \varepsilon_{\mathrm{L}} - q^{(k)} \right| - r^{(k)} \right]^2$.

For enhanced accuracy, iterative calculation is repeated until the average squared distance error, $f(\varepsilon_L)/n$, becomes smaller than a preset error target. To help with the convergence, the outliers are excluded at each iteration step. Fig. 2.2 shows an example plot of 11 circular loci for 0.9% saline measured using the proposed MSR at 16 GHz. The triangular point (47.85-j33.45) represents the extracted $\varepsilon_L$ using equation (2.8) while the circular one is the reference data (46.71-j35.39) [34]. Very close agreement can be found, validating the extraction method of this work.
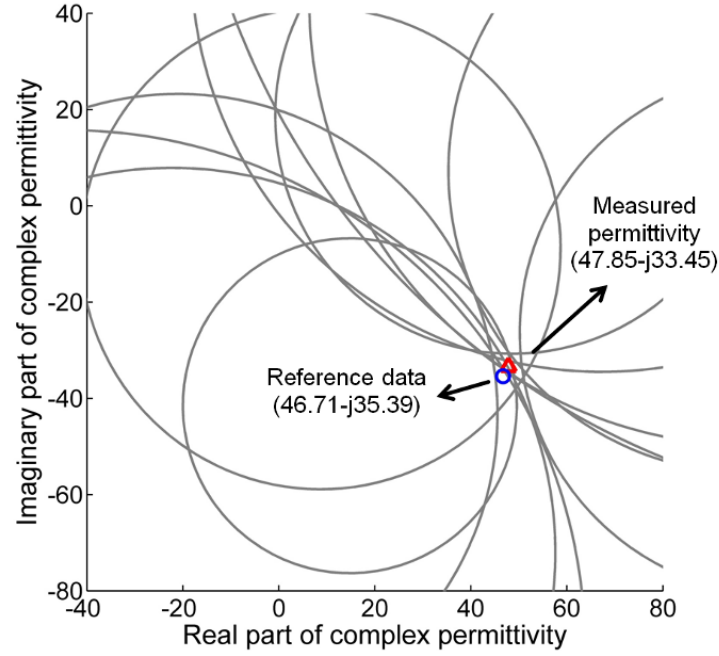
Fig. 2.2 Complex permittivity of 0.9% saline extracted at 16 GHz from the 11 circular loci and the comparison with the reference data.

## 2.2.4 Calibration

The system constants, $A^{(k)}$, $B^{(k)}$, and $g^{(k)}$ in equation (2.5) can be determined by measuring calibration materials with known permittivities. Because there are five scalar unknowns for each state $k$, the power readings of five different calibration materials are required to estimate the system constants. For each state, $k$, one needs to find the solution set satisfying the following coupled equations:

$$f_i\left(A^{(k)}, B^{(k)}, g^{(k)}\right) = \left[\frac{P_R^{(k)}}{P_I^{(k)}}\right]_i - g^{(k)}\left|\frac{1 + A^{(k)} \cdot \varepsilon_i}{1 + B^{(k)} \cdot \varepsilon_i}\right|^2 = 0 \qquad (2.9)$$

where $\varepsilon_i$ is the complex permittivity of the $i^{\text{th}}$ calibration material ($1 \leq i \leq 5$), and $[P_R^{(k)}$ / $P_I^{(k)}]_i$ is the measured power ratio of $i^{\text{th}}$ material at state $k$. The solutions of the nonlinear coupled equations are obtained using Matlab.

## 2.3    Design and Fabrication

An integrated MSR system is realized by integrating the circuit components shown
in Fig. 2.1 and RF signal source on a micromachined probe platform. For accurate
breast cancer detection, the MSR of this work is targeted to measure the permittivity
data at both low (2 GHz) and high (16 GHz) band frequencies [1], [5]. This presents
special challenges in terms of the component design; all the components in Fig. 2.1
should cover a very broad bandwidth from 2 to 16 GHz. The details of the
component design are elaborated in the following subsections.

### 2.3.1   Micromachined Planar Coaxial Probe

The planar probe with an open-ended coaxial aperture is a key component for
permittivity measurements. It not only provides the interface between the MSR
system and MUT at the aperture, but also serves as a motherboard on which the
other circuits are integrated. Since the electrical characteristics of the probe are
highly sensitive to the dimensions of the aperture [28], a high-resolution fabrication
technique is required for accurate permittivity measurement. In this work, silicon
bulk micromachining is employed for this purpose. It also provides the possibility of
further miniaturization and monolithic integration with other circuits.

Following the design methodology presented in [28], the aperture dimensions
are determined to minimize the sensitivity of the extracted permittivity to the errors

21

of the measured power readings. The radii of the inner and outer conductors of the aperture are selected to be 0.2 mm and 0.3 mm, respectively. With these aperture dimensions, the corresponding admittance of the open-ended aperture becomes $1.334 \times 10^{-7} + j0.0011$ S at 16 GHz, which provides the smallest measurement uncertainty. The small-sized aperture also minimizes the radiation effect.

Since the probe transfers the signal to and from the aperture, it should also work as a transmission line supporting broadband signal transmission up to over 20 GHz. The concept of substrate integrated waveguide (SIW) has been applied to extend the transmission bandwidth [35], [36]. The overall structure and cross-sectional view of the probe structure are shown in Fig. 2.3, which basically corresponds to the configuration of the asymmetric shielded strip line. To cover the required bandwidth, one needs to suppress the higher-order mode of the strip line, which is the $TE_{10}$ mode of the rectangular waveguide.

The cut-off frequency of $TE_{10}$ mode is

$$f_c = \frac{c}{2w\sqrt{\mu_r \varepsilon_r}} \tag{2.10}$$

where $c$ is the velocity of light in free space, $w$ is the width of the probe substrate, and $\varepsilon_r$, $\mu_r$ are relative permittivity and permeability of the substrate, respectively. From equation (2.10), the width of the probe should be minimized for broadband

transmission. However, this also minimizes the footprint of the motherboard, making the active circuit integration virtually impossible. This problem is solved by asymmetric arrangement of shielded strip line using SIW approach [36]. The effective width of top ground plane in the shielded-strip line is reduced to 1.5 mm by placing via arrays along the line, while maintaining the width of the probe platform to 6.8 mm. This configuration guarantees single-mode propagation up to 23.8 GHz.

The fabrication process steps of the micromachined probe are shown in Fig. 2.4. We used 300-μm-thick double-side-polished high resistive silicon (HRSi) wafers as top and bottom substrates. First, the signal lines and the ground plane on the bottom substrate were defined with 3-μm-thick gold layers by electroplating process (See Fig. 2.4(a) and (b)). After patterning, via holes were formed using dry-etching process (See Fig. 2.4(c)), which was selected over wet-etching for better dimensional control. Dry-etched via holes also require much smaller capture pad area, which help minimize the transmission line discontinuity. The aperture was formed on the backside ground plane of the bottom substrate before it was bonded to the top substrates, which helped improve the manufacturing yield. On the top plane of the bottom substrate, benzocyclobutene (BCB) was coated and patterned as a bonding layer (See Fig. 2.4(d)). The top substrate was then bonded with the bottom substrate through BCB bonding layer (See Fig. 2.4(e)). The ground plane surrounding the signal line is provided by the bottom metal plane and silver epoxy

sprayed on the surface of the top substrate (See Fig. 2.4(f)). The top and bottom substrates are electrically interconnected through the silver epoxy-filled via holes. Fig. 2.5 shows the photograph of the fabricated silicon MEMS probe motherboard. The length, width, and thickness of the Si motherboard are 50 mm, 6.8 mm and 0.6 mm, respectively.
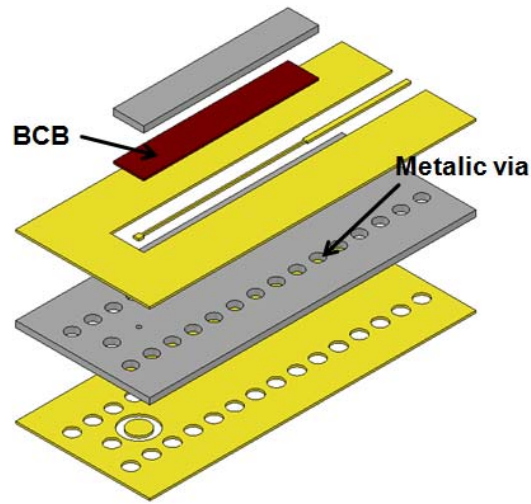
(a)
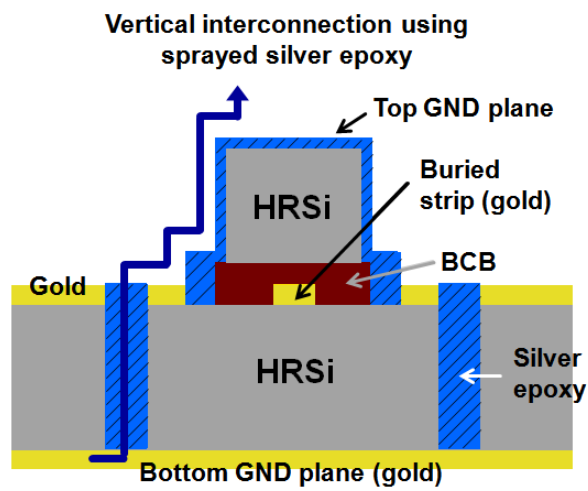


(b)

Fig. 2.3 (a) Three-dimensional view of the proposed probe structure. (b) Cross-sectional view of the probe structure.
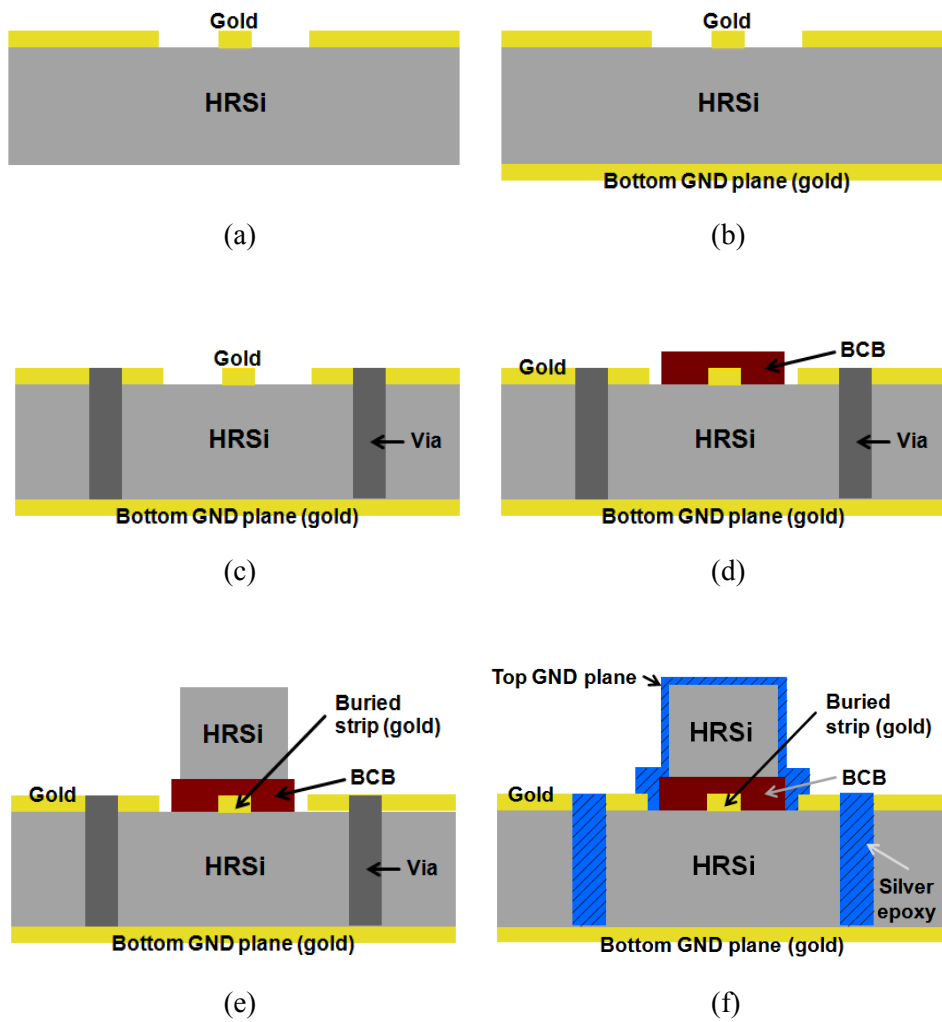
Fig. 2.4 Fabrication process of the micromachined probe.
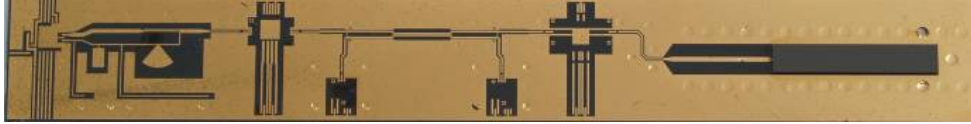
(a)



(b)
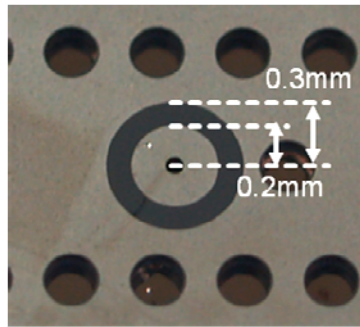


(c)

Fig. 2.5 Photograph of the fabricated probe motherboard: (a) top side, (b) bottom side, and (c) enlarged view of the probe aperture.

To evaluate the performance of the micromachined probe, we measured the complex permittivity of 0.9% saline from 0.5 to 26.5 GHz. A commercial VNA (Agilent PNA E8361A) was used to measure S-parameters using the fabricated probe as the interface to MUT. The liquid calibration method presented in [37] was performed by measuring air, methanol, and distilled water as calibration standard materials. Using the method presented in [37], the complex permittivity of 0.9% saline was extracted. Fig. 2.6 shows the comparison with the reference data from [34]. As can be seen in Fig. 2.6, the measured permittivity values show good agreement with the reference data up to 22 GHz, over which higher-order modes kick in and cause scatters in the data. This shows that the SIW-based probe has sufficient bandwidth for permittivity measurement targeted for this work.
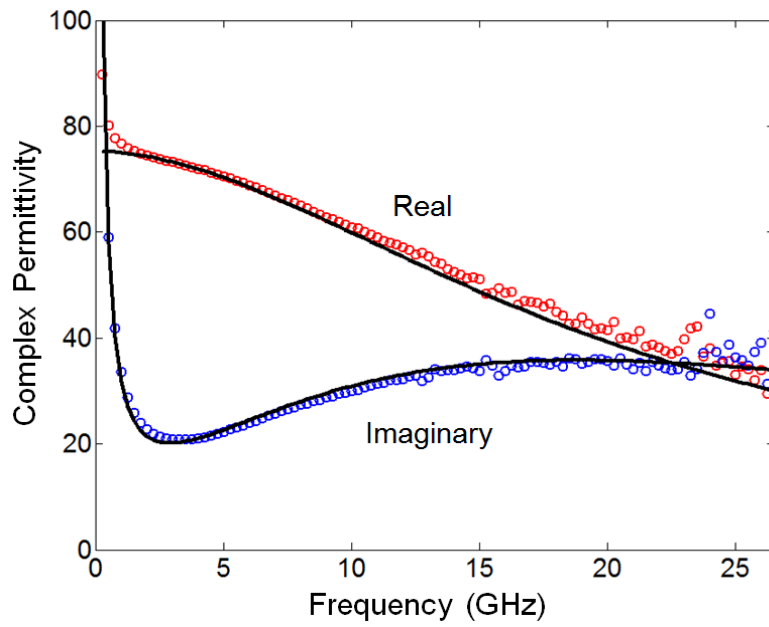
Fig. 2.6 Measured complex permittivity of 0.9% saline from 0.5 to 26.5 GHz using the micromachined probe and VNA.

## 2.3.2 Impedance Tuner

An impedance tuner presents various impedances to the probe so that multiple states can be generated for MSR operation. The simplified schematic of the tuner is depicted in Fig. 2.7(a). The tuner is a 6-bit digital tuner, where 64 impedances are generated by controlling on/off states of six switches. Even though only three states are required for MSR operation, 64-state capability is employed in this work to secure sufficient redundancy for high-accuracy measurement over a broad bandwidth. In order to accurately measure the permittivity of biological materials, which typically show lossy dielectric characteristics, we have performed a sensitivity analysis and set the maximum tuner impedance range at $|\Gamma| \sim 0.7$.

The tuner design is based on the double-stub tuner configuration proposed in the previous work [38]. Various admittances of shunt stubs (Y1, Y2) are generated by changing the states of the switches at the end of shunt stubs (SW1, SW2, SW5, SW6). The loaded series lines (TL1-TL3) connecting the two shunt stubs function as an impedance transformer. If a single series line with a fixed electrical length and characteristic impedance ($Z_0$) were used, it would provide required tuning range only near the center frequency. In this work, the series lines are loaded with switchable capacitors (SW3, SW4) to change the electrical length and $Z_0$ according to the frequencies.

The tuner was fabricated using commercial 0.15-μm GaAs pHEMT foundry

process. GaAs pHEMT technology was used instead of Si CMOS due to its favorable Q-factors and lower $R_{on}$-$C_{off}$ product, resulting in wider VSWR coverage. The unit transistor size used for a switch is set to $8 \times 40$ μm, considering both on-state resistance ($R_{on}$) and off-state capacitance ($C_{off}$). The photograph of the fabricated tuner is shown in Fig. 2.7(b). The die size is 3.1 mm $\times$ 1.8 mm including the probe pads. The measured impedance constellations at 2, 8, and 16 GHz are plotted in Fig. 2.8, showing spread-out impedance distribution.
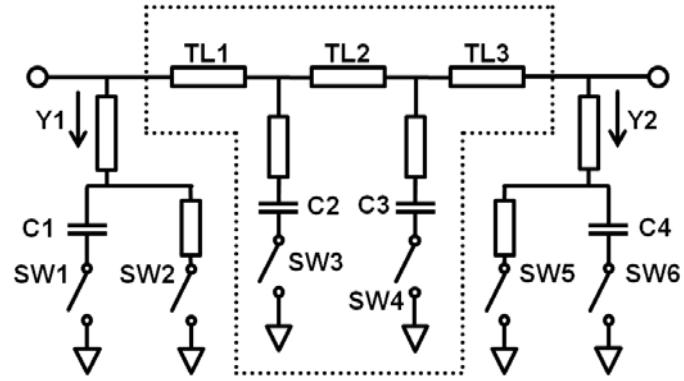
(a)
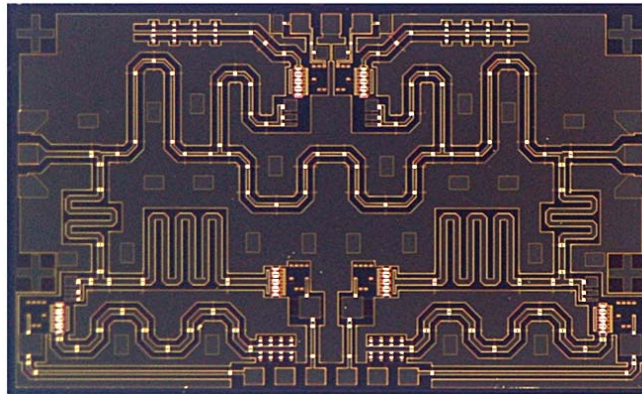


(b)

Fig. 2.7 (a) Schematic diagram of the broadband impedance tuner. (b) Die photograph of the fabricated impedance tuner (size: 3.1 mm × 1.8 mm).

(a)



(b)



(c)
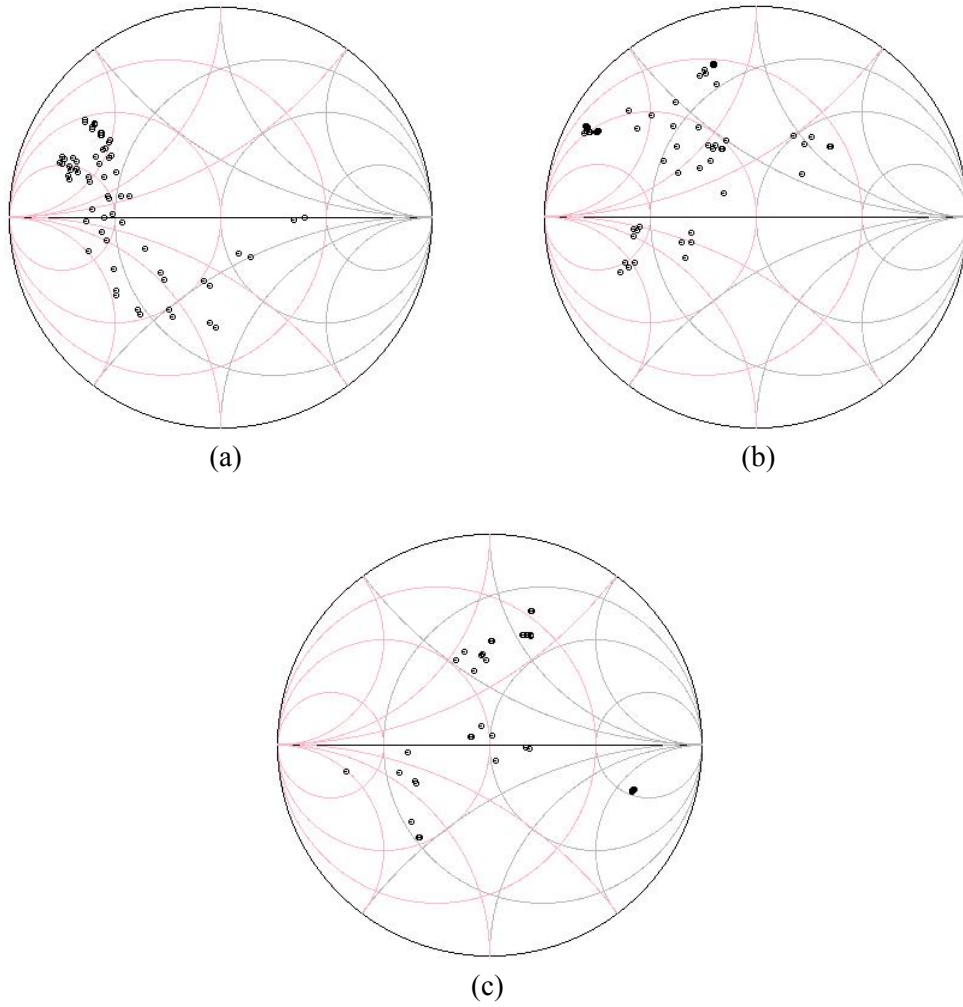
Fig. 2.8 Measured impedance constellations of the impedance tuner at: (a) 2 GHz, (b) 8 GHz, and (c) 16 GHz.

### 2.3.3 Directional Coupler

To cover a wide frequency range from 2 to 16 GHz, a symmetrical three-section coupled line coupler shown in Fig. 2.9(a) is designed following a broadband design principle used for filters and impedance transformers [39]-[42]. As is well known, microstrip-based coupler implementation suffers from degraded directivity due to the mismatch of even- and odd-mode wave velocities. The problem of poor directivity becomes more severe as the frequency gets higher. In this work, we have tried to compensate for high-frequency directivity degradation by introducing capacitors (C1, C2) at the ends of each coupled line section [43]. The port matching has been improved by adding a shunt capacitor (C3) at each port. The coupling level of each section including the capacitance loading is designed to achieve equi-ripple coupling.

The proposed broadband coupler was fabricated on the same silicon substrate as the probe. The photograph of the fabricated coupler is shown in Fig. 2.9(b). The capacitances (C1, C2, C3) in the coupler are realized using interdigital capacitors considering their small capacitance values (<tens of fF). Fig. 2.10 shows the measured S-parameters up to 20 GHz using on-wafer probing. The measured coupling is 8.6±1.2 dB in the frequency range of 3.1-16.6 GHz. The return loss and isolation are better than 19.2 dB and 23.7 dB, respectively. A larger coupler with more sections could have flattened the coupling characteristics down to 2 GHz.

However, since the coupler still shows good return loss (22.8 dB) and directivity (16.3 dB) at 2 GHz, and the loss of the components after the coupler is smaller for low frequencies, the weaker coupling (12.3 dB) does not degrade MSR performance at 2 GHz.
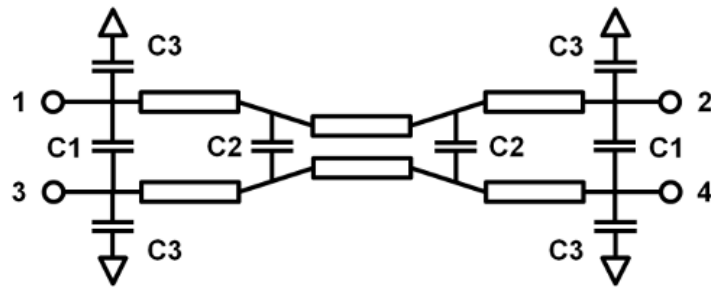


(a)



(b)

Fig. 2.9 (a) Schematic diagram of the broadband directional coupler. (b) Photograph of the broadband coupler fabricated on Si MEMS substrate.
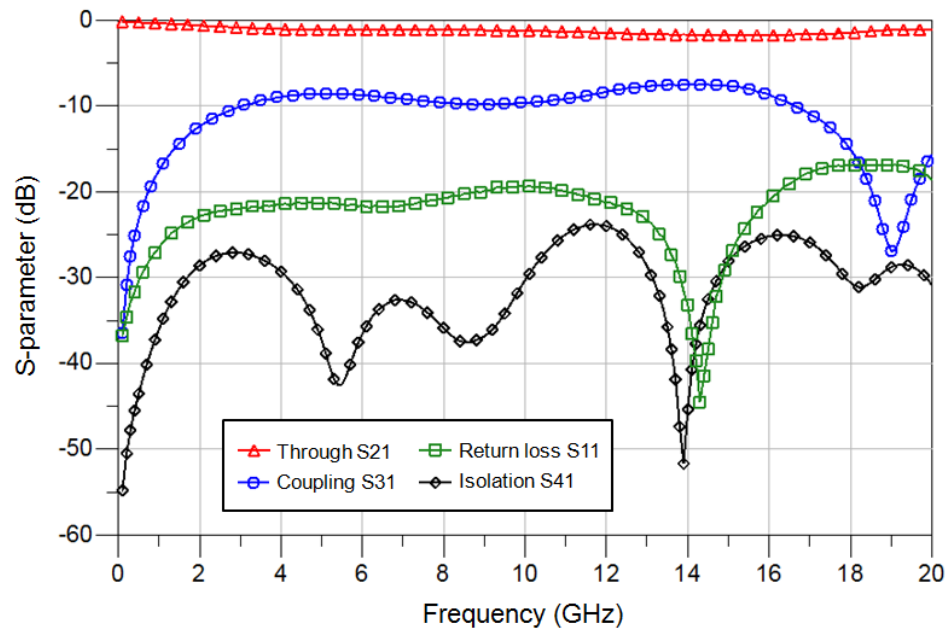
Fig. 2.10 Measured S-parameters of the broadband coupler.

### 2.3.4  Power Detector

Since the measured power readings by the power detectors determine the location

and radius of the permittivity circles (see equation (2.7)), accurate power detection is

very important. The trade-off in the detector design is bandwidth versus dynamic

range. In this work, a simple half-wave rectifier using a single diode and an RC low-

pass filter (LPF) is employed due to its small parasitic capacitance, resulting in large

bandwidth. The dynamic range limitation is mitigated by boosting the incident signal

level using a power amplifier after PLL in the source block. The power detector was

fabricated using the same GaAs process as the impedance tuner. The diode used in

the detector is a Schottky diode with an anode size of $2 \times 10$ μm. The detector chip

size is 1.1 mm $\times$ 0.7 mm including all the pads. The photograph of the fabricated

power detector is shown in Fig. 2.11. As shown in Fig. 2.12, the detector shows

uniform response from 2 to 16 GHz with the sensitivities higher than 0.24 mV/dB at

the input power of -30 dBm over the entire frequency range.
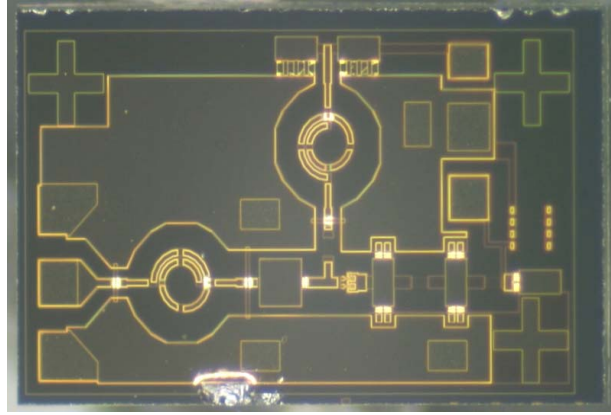
Fig. 2.11 Die photograph of the fabricated power detector.
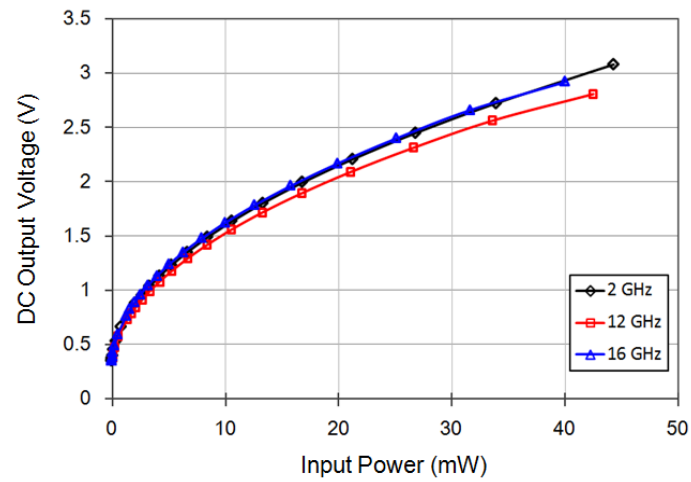


Fig. 2.12 Measured DC output voltage versus RF input power using the fabricated power detector from 2 to 16 GHz.

## 2.3.5  Signal Source

For signal purity and stability, a PLL approach is adopted for a signal source. As shown in the block diagram of Fig. 2.13, it consists of a 16-GHz voltage controlled oscillator (VCO), a divide-by-8 frequency divider, a divide-by-32 low-frequency divider, a phase detector, a LPF, and buffer amplifiers. 16-GHz signal from the VCO is phase-locked to 62.5-MHz reference signal through the divide-by-256 divider. The buffer amplifier after the VCO delivers the output signal to 16 GHz high-band output port and also provides isolation from its load. For dual-band operation, 2-GHz output signal from the divided-by-8 frequency divider is branched out and amplified by another buffer amplifier. The PLL was fabricated using 0.13-μm CMOS process (IBM 8RF-DM with 1 poly and 8 metal layers). The size of the entire chip is 0.9 mm × 1.0 mm. The measurement of the PLL showed a locking bandwidth of 1.6 GHz around 16 GHz, and the output power of -5 dBm.

The low- and high-band signals from the PLL are combined using a power combiner integrated on the probe motherboard. The combiner consists of a LPF for 2-GHz signal and a band-pass filter for 16 GHz, the outputs of which are combined to feed the subsequent power amplifier (see Fig. 2.14(b)). The isolation between the ports is 12 dB and harmonic suppression from the PLL is better than 20 dB. The band selection of the PLL output is implemented by turning on and off the buffer amplifiers. The photographs of the PLL chip and the entire signal generator are

shown in Fig. 2.14.

For accurate power reading, it is important to guarantee that the power level delivered to the power detector after the reflection from MUT stays within the dynamic range of the detector. After link budget calculation, it is determined that the output power from the signal generator block should be higher than 8 dBm. For this purpose, a broadband power amplifier covering from 2 to 16 GHz has been designed. For broadband coverage, we have employed the stacked FET approach presented in our previous work [44], [45]. Compared with current combining, voltage combining based on the stacked amplifiers presents much larger load impedance, which allows the output matching to be realized in the low Q-region and offers broadband power performance.

As in the case of the detector and tuner, the amplifier was fabricated using 0.15-μm GaAs pHEMT foundry. The chip size is 2.3 mm × 1.4 mm. The size of each FET in the amplifier is 8 × 100 μm, and three FETs are stacked. The saturated output power is more than 12.5 dBm from 2 to 16 GHz. Measured output power from the entire signal source block is shown in Fig. 2.15. The output power was higher than 9.1 dBm from 2 to 16 GHz, meeting the minimum requirement of 8 dBm.
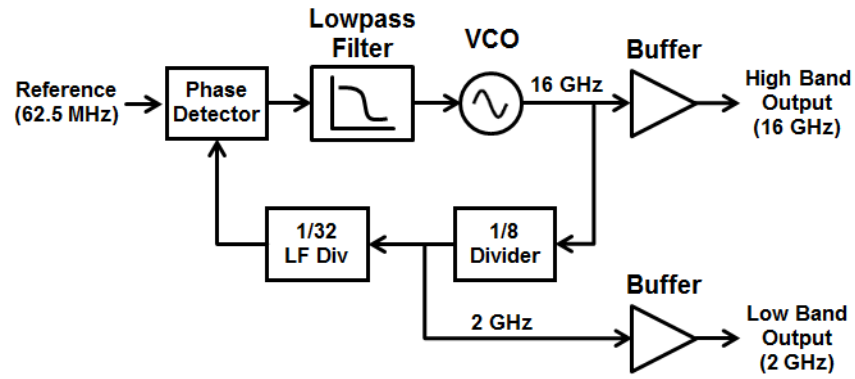
Fig. 2.13 Block diagram of the dual-band PLL.



(a)                                                    (b)
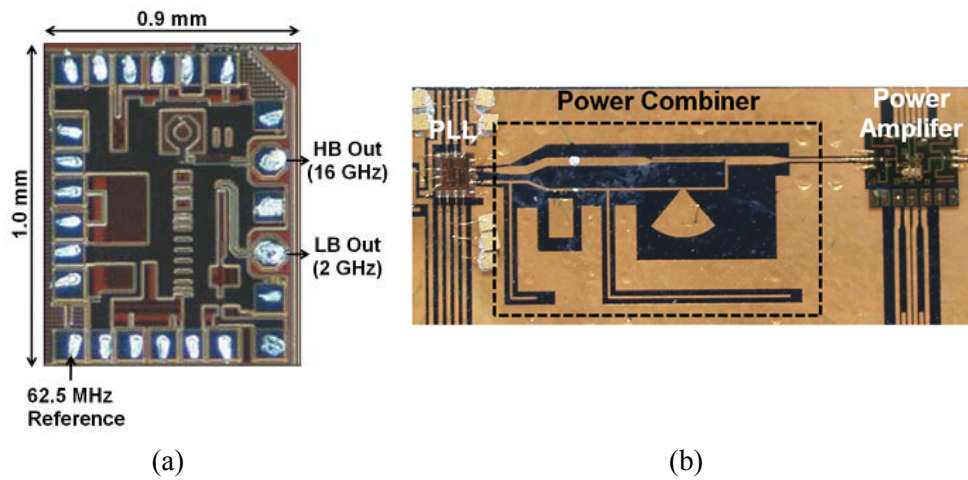
Fig. 2.14 (a) Photograph of the PLL fabricated using 0.13-μm CMOS process (size: 0.9 mm × 1.0 mm). (b) Photograph of the assembled signal generator showing the details of the dual-band power combiner.

41
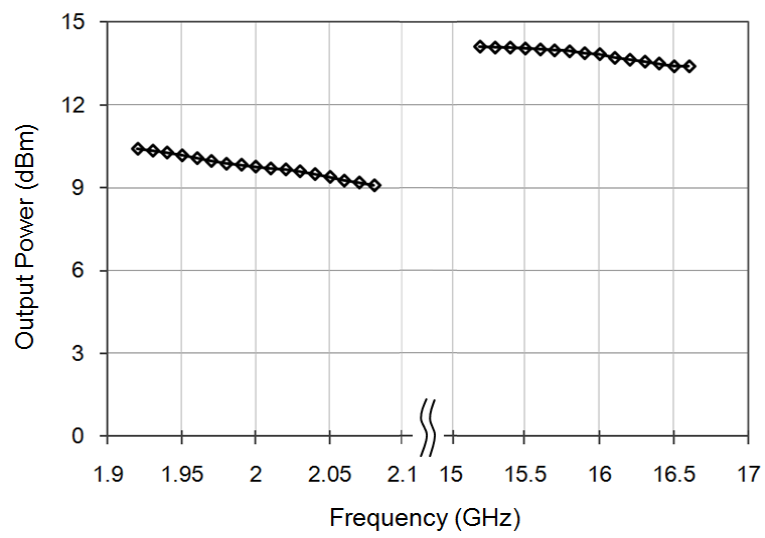
Fig. 2.15 Measured output power of the signal generator block.

## 2.3.6 Active Integrated Probe System

RF block of MSR is fully integrated on a MEMS probe platform as shown in Fig. 2.16. For this purpose, monolithic microwave integrated circuit (MMIC) chips such as PLL, power amplifier, impedance tuner and power detectors are integrated on the probe motherboard. The performances of the individual circuit components are summarized in Table 2.1. All the circuits are interconnected using the wire bonds. For better manufacturability, the die can also be flip-chipped for vertical connection as demonstrated in [46]. DC and baseband circuitry is realized on the printed circuit board (254-μm-thick RO4350B), on which the probe motherboard is mounted together with the bypass capacitors. The reference frequency signal for the PLL is fed through an SMA connector, and the bias voltages and control signals are supplied to the module via the pin header connectors. The similar connectors are used to read the DC voltages from the power detectors.
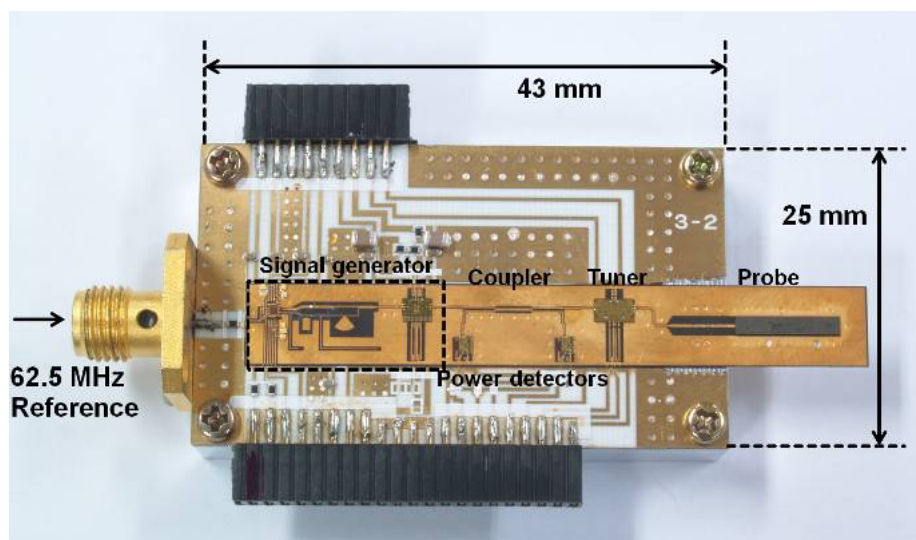
Fig. 2.16 Photograph of the entire MSR module assembled on the PCB with the connectors installed.

TABLE 2.1

<small>PERFORMANCES OF THE CIRCUIT COMPONENTS FOR THE ACTIVE INTEGRATED</small>

<small>PROBE</small>

| Circuit | Topology | Technology | Performances |
|---------|----------|------------|--------------|
| Probe | Planar coaxial | Si MEMS | BW: ~23.6 GHz <br> (Single mode propagation) |
| Impedance tuner | 6-bit digital tuning | GaAs pHEMT | BW: 2-16 GHz ($|\Gamma|_{max} > 0.7$) |
| Power detector | Source-connected FET diode detector | GaAs pHEMT | BW: 2-18 GHz <br> Sensitivity > 0.24 mV/dB <br> (@ -30 dBm) |
| PLL | Dual-band | Si CMOS | BW: 1.9-2.08, 15.2-16.6 GHz <br> $P_{out}$: -5 dBm |
| Driver amplifier | Stacked-FET | GaAs pHEMT | BW: 2-16 GHz <br> $P_{sat} > 12.5$ dBm |
| Coupler | Multi-section coupled line | Si MEMS | BW: 3.1-16.6 GHz <br> Coupling: 8.6±1.2 dB <br> Isolation > 23.7 dB |

BW: Bandwidth

## 2.4    Measurement Results

To validate the proposed MSR and active integrated probe, complex permittivity measurements were conducted using the experimental setup shown in Fig. 2.17. The reference signal is injected to the PLL using an Agilent 33250A function generator. A digital multimeter (Agilent 34401A) is used to read the output DC voltages from the power detectors at each tuner state. RF power levels are then calculated from the measured DC voltages using the calibration table obtained during detector calibration. The state of the impedance tuner is controlled by the embedded switches in an Advantech USB-4761 module. All the instruments are controlled by a PC using the Agilent VEE (Visual Engineering Environment) program. Fig. 2.18 shows a photograph of MSR measuring the complex permittivity of 0.9% saline. Other than the aforementioned DC instruments, no RF equipments are required to measure the permittivity at 2 and 16 GHz.

As the first step of the measurement, calibration is performed at each tuner/MSR state, $k$, to find the system constants, $A^{(k)}$, $B^{(k)}$, and $g^{(k)}$ (equation (2.5)) following the method shown in section 2.2. Five calibration standards are used for this purpose: distilled water, acetone, air, ethanol, and methanol. After calibration, 0.9% saline is used as MUT to verify the accuracy of the proposed MSR probe. Saline is used as verification material since it has similar electrical property as biological materials and the reference permittivity data are readily available [34].
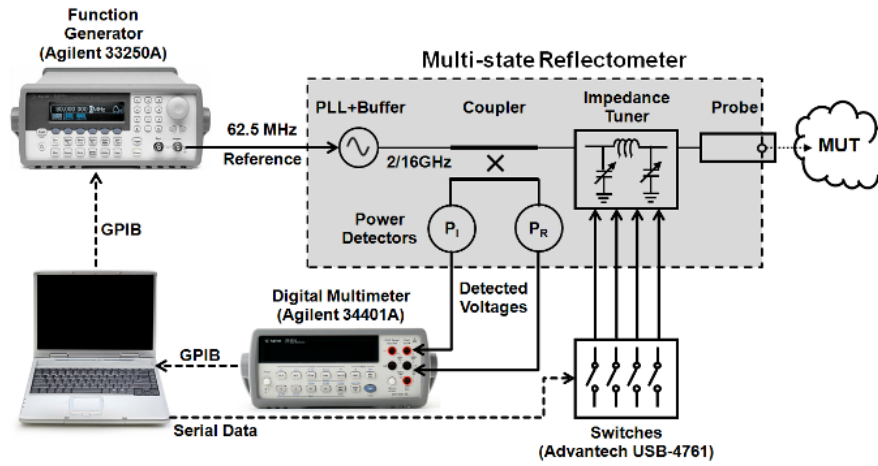
Fig. 2.17 Test setup for complex permittivity measurements using the proposed MSR.



Fig. 2.18 Photograph of the MSR in contact with the 0.9% saline for complex permittivity measurement.

Dual-band measurement is performed at a low-band of 1.9-2.08 GHz and high-band of 15.2-16.6 GHz. The complex permittivities are extracted by solving equation (2.8) using the Newton-Raphson method. The measured complex permittivity of 0.9% saline is shown in Fig. 2.19, and is compared with the reference data. The circles and crosses represent the measured real and imaginary permittivities of 0.9% saline, respectively, while the solid line and dashed line are the reference permittivity data [34]. The measured complex permittivity is well matched with the reference data, showing the standard deviation less than 4.5% and 4.1% at 2 and 16 GHz, respectively.

We have also used pork muscle, fat, and human breast cancer using nude mouse xenografted model to further verify the integrated MSR probe. Pork muscle and fat have similar permittivities as human breast cancer and fat, respectively [1], [14], [47], which allows one to use them to emulate the human cancer and fat. For measurement of the samples, the planar probe can be inserted into MUT after incision, as demonstrated in [27]. In Figs. 2.20, 2.21, and 2.22, the measured data of pork muscle, fat, and cancer are compared with those taken using a commercial VNA (Agilent PNA E8361A) and open-ended coaxial probes [48], [49]. The data from pork muscle shows similar level of accuracy as 0.9% saline. The variance is relatively higher for pork fat due to its small permittivity values. The error can be reduced by using calibration materials with similar permittivity values as MUT.
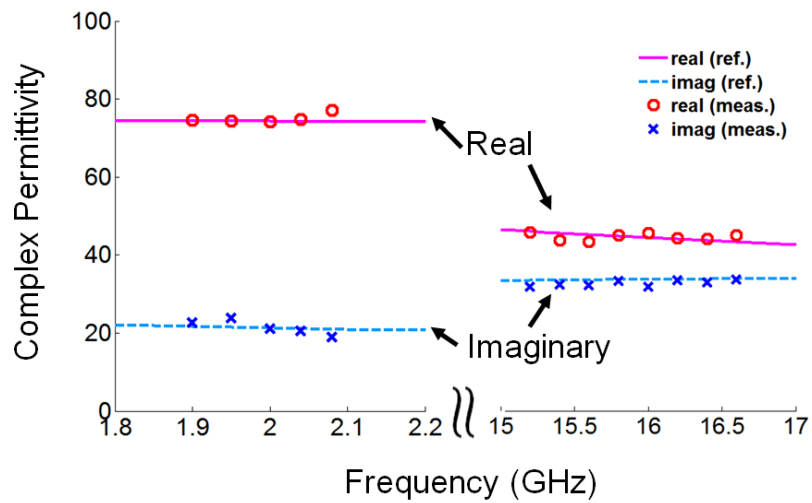
Fig. 2.19 Measured complex permittivities of 0.9% saline at 1.9-2.08 GHz and 15.2-16.6 GHz.
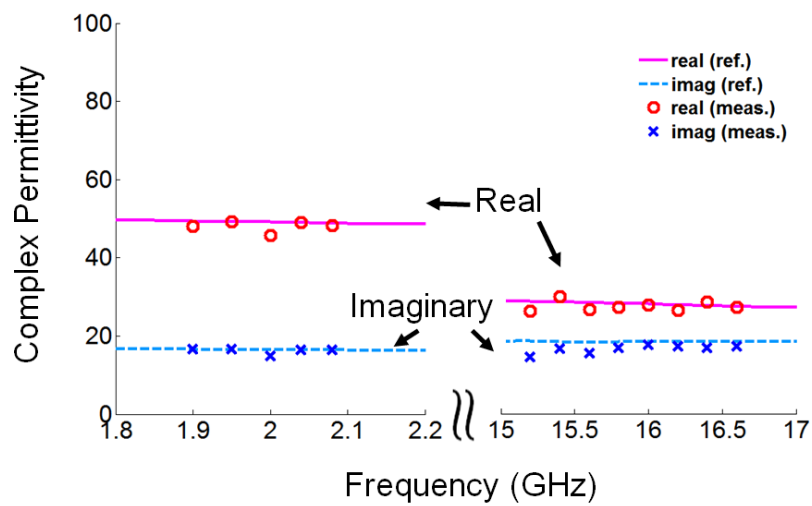


Fig. 2.20 Measured complex permittivities of pork muscle at 1.9-2.08 GHz and 15.2-16.6 GHz.

49
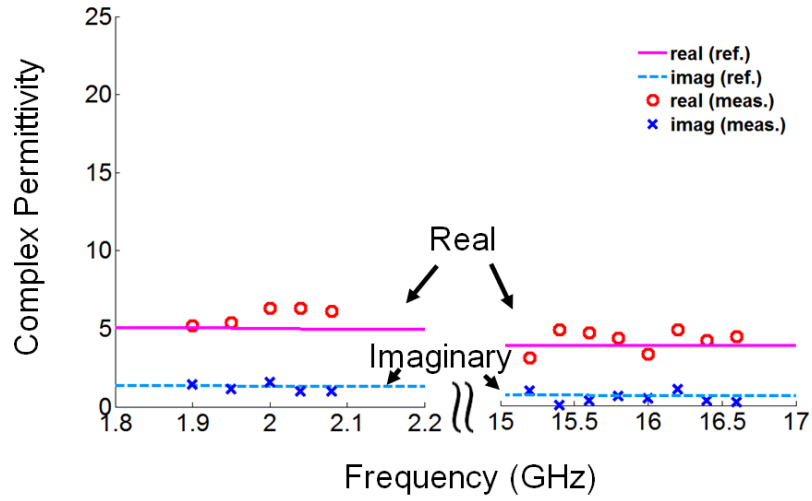
Fig. 2.21 Measured complex permittivities of pork fat at 1.9-2.08 GHz and 15.2-16.6 GHz.
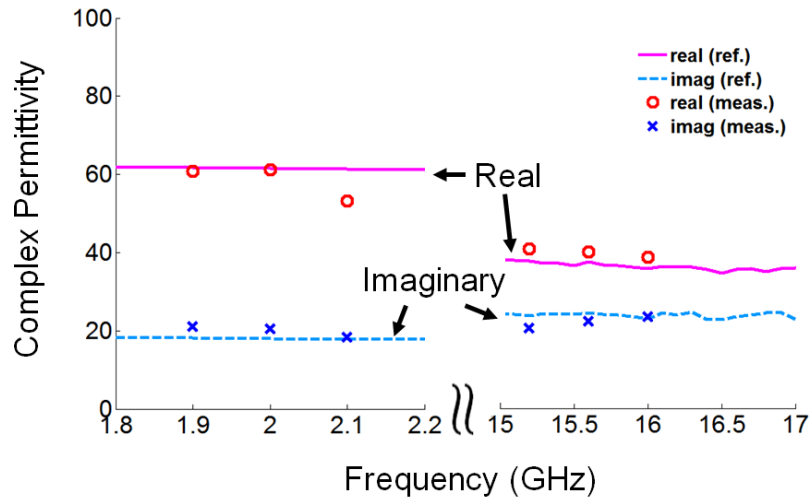


Fig. 2.22 Measured complex permittivity of *ex-vivo* human breast cancer using nude mouse xenografted model at 1.9-2.08 GHz and 15.2-16.6 GHz.

To assess the wideband performance of the proposed integrated probe, we have disconnected the integrated PLL and employed an external synthesizer (Agilent E8257D) to sweep the frequencies continuously from 2 to 20 GHz. For each frequency point with 2-GHz step, calibration is performed using the same calibration standards at 64 tuner/MSR states. Fig. 2.23 shows the measured complex permittivity of 0.9% saline from 2 to 20 GHz. As can be seen in Fig. 2.23, the measured values show good agreement with the reference data from 2 to 16 GHz, demonstrating the broadband capability of the proposed MSR probe. Degraded performance above 16 GHz is mainly attributed to the bandwidth limitation of the coupler and the reduced tuning range of the impedance tuner at high frequencies.
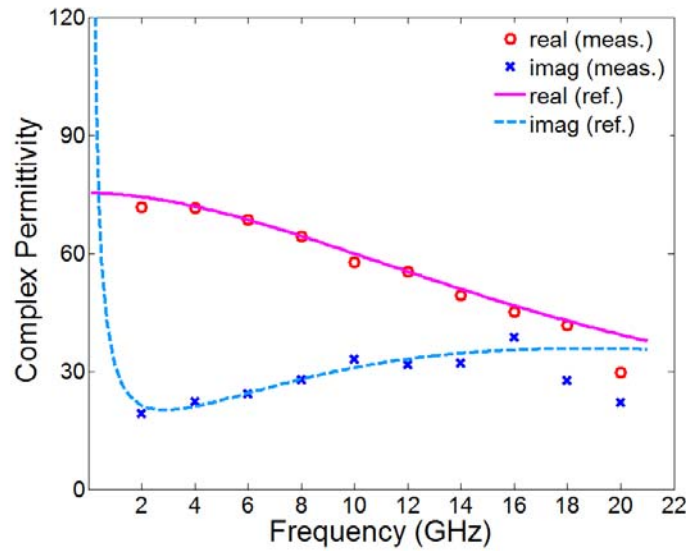


Fig. 2.23 Measured complex permittivity of 0.9% saline from 2 to 20 GHz using an external signal source.

## 2.5    Summary

A fully integrated miniaturized MSR has been developed for dual-band complex permittivity measurement. Since the MSR has to cover both 2 and 16 GHz bands, the unit RF components have been designed with multi-octave broadband characteristics. For example, SIW concept has been applied to the micromachined planar coaxial probe to avoid higher-order modes up to 23 GHz. Loaded series transmission line is used together with two switchable shunt arms to realize broadband impedance tuners. Dual-band PLL and broadband power amplifier using the stacked-FET structure are used as a signal source block to generate the clean RF signals with the transmit power higher than 9 dBm at 2 and 16 GHz. The entire active and passive circuits have been integrated on the micromachined planar probe motherboard to implement a fully integrated MSR in a small form factor of 6.8 mm × 50 mm × 0.6 mm. The active integrated MSR of this work does not only provide vast cost savings compared to the commercial VNA, but also offer the unique advantage of miniaturization – small enough to be used as a hand-held device for ultimate portability.

To demonstrate the accuracy of the proposed MSR for permittivity measurements of biological material, we measured 0.9% saline, pork muscle, fat, and *ex-vivo* human breast cancer cells at 1.9-2.08 GHz and 15.2-16.6 GHz. The measured results show good agreement with the reference data for 0.9% saline and

VNA measurement data for pork muscle, fat, and human breast cancer, respectively. The overall frequency characteristics of the MSR are also verified using an external frequency synthesizer that sweeps the frequency of the incident wave from 2 to 16 GHz.

Successful medical application of microwaves should allow easy application of the microwave methods to the practical clinical environment. The integrated MSR of this work opens doors to a new practical method of biological material characterization in terms of ease of use, compactness, and cost-effectiveness.

# Chapter 3

# *Ku*-Band Active Integrated Heat Applicator for Cancer Ablation

## 3.1    Introduction

Throughout the years, microwave hyperthermia has attracted much attention as an alternative method for cancer ablation due to safeness and ease of use [2], [50]-[52]. Many researches have been carried out in this respect, yielding promising results. Clinical trials have shown the effectiveness of the microwave method for cancer ablation [2], [52]. Nevertheless, the existing microwave hyperthermia system has limitations in practical applications because of poor heating efficiency and excessive power requirement. It has generally utilized the low-frequency spectrum below 5 GHz, where electromagnetic power absorption efficiency of cancer cells is relatively low [11]. In order to provide sufficient thermal dose for complete tumor ablation,

high microwave power of several tens of watts is needed [53], [54], thus resulting in severe collateral damage to healthy tissues near the passage of the applicator. In consideration of the clinical use, the requirement of high-power microwave poses a potential risk both to the patients and clinicians. In addition, expensive and bulky microwave source and heat applicator to handle the required power are obstacles to overcome in practical applications.

In order for microwave methods to find proliferation, microwave heating efficiency should be increased, thereby reducing the required source power. Broadband permittivity characterization shows that cancer cells have a higher dielectric loss than normal tissues and the loss difference reaches its peak in the frequency range from 15 to 20 GHz as shown in Fig. 3.1 [1]. Therefore, the use of *Ku*-band frequencies can result in high-efficiency/low-power hyperthermia with only a few watts of power [6]. Moreover, the short wavelength helps to reduce the overall size and cost of the hyperthermia system through high-level integration. Recently, the feasibility of a partially integrated hyperthermia applicator has been demonstrated on a conventional PCB at *K*-band [14]. This work presents a microwave active integrated heat applicator for cancer ablation. Monolithic microwave integrated circuits (MMIC's) for microwave power generation are integrated on a micromachined silicon applicator to implement a fully integrated hyperthermia system.
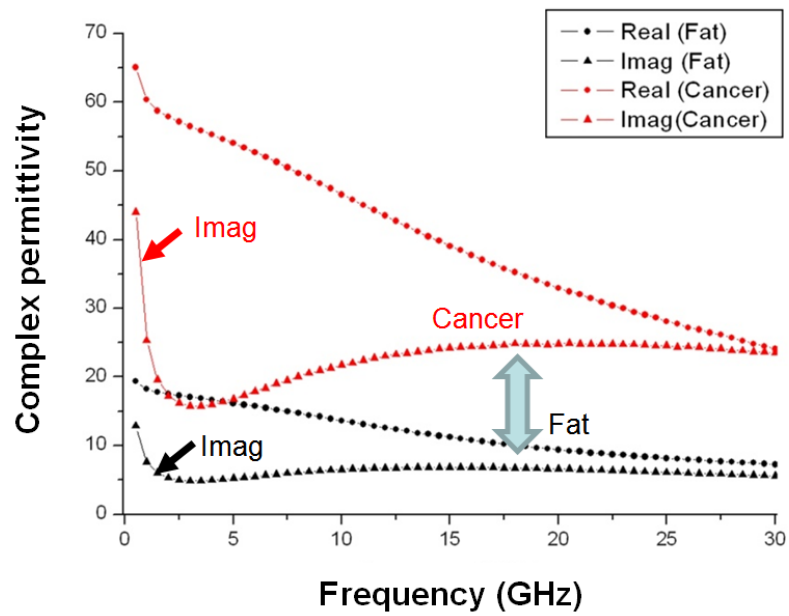
Fig. 3.1 Measured complex permittivities of cancer and fat.

## 3.2    Design and Fabrication

An active integrated applicator system is realized by integrating the circuit components shown in Fig. 3.2 on a micromachined applicator platform. A *Ku*-band source module consisting of a voltage controlled oscillator (VCO), a driver amplifier, and a power amplifier (PA) is implemented in MMIC's to facilitate integration and miniaturization. A directional coupler and two power detectors are employed to monitor delivered and reflected power during hyperthermia. The details of the component design are presented in the following subsections.
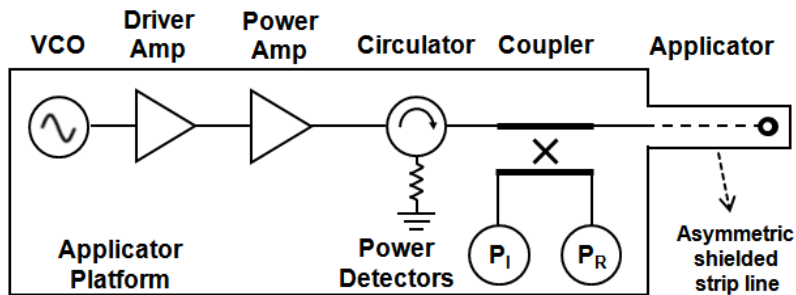


Fig. 3.2 Block diagram of the *Ku*-band active integrated hyperthermia system implemented on the heat applicator platform.

### 3.2.1 Micromachined Planar Coaxial Applicator

The heat applicator is based on an open-ended planar coaxial aperture structure presented in [27]. The applicator platform doubles in function as a microwave radiator as well as a motherboard for active circuit integration. In this work, silicon bulk micromachining is employed as the applicator platform since it provides ultimate miniaturization and integration capability with other circuits.

The overall structure and cross-sectional view of the MEMS applicator platform are shown in Fig. 3.3. The applicator has a similar structural configuration to the MEMS probe for permittivity measurement presented in chapter 2. The radii of the inner and outer conductors of the aperture on the bottom surface of the applicator are determined to be 0.9 and 2 mm, respectively, considering radiation efficiency and material selectivity at *Ku*-band [6]. To guarantee single-mode propagation up to *Ku*-band, the shielded strip line in the applicator has asymmetric arrangement using substrate integrated waveguide (SIW) approach [35]. The effective width of top ground plane of the strip line is reduced to 2.1 mm by placing via arrays along the line while the width of the applicator platform is 8 mm.

The applicator has been fabricated based on the same process as that for permittivity measurement probe (See Fig 2.4). Double-side-polished high resistive silicon (HRSi) wafers with 300-μm thickness were used as top and bottom substrates. The signal lines were defined with 3-μm-thick gold layers by electroplating process.

The substrates were bonded together through benzocyclobutene (BCB) bonding layer after gold patterning and dry-etched via hole forming. The ground plane surrounding the signal line is provided by the bottom metal plane and silver epoxy sprayed on the surface of the top substrate. Fig. 3.4 shows the photograph of the fabricated silicon MEMS applicator. The length, width, and thickness of the fabricated applicator motherboard are 56 mm, 8 mm, and 0.6 mm, respectively.
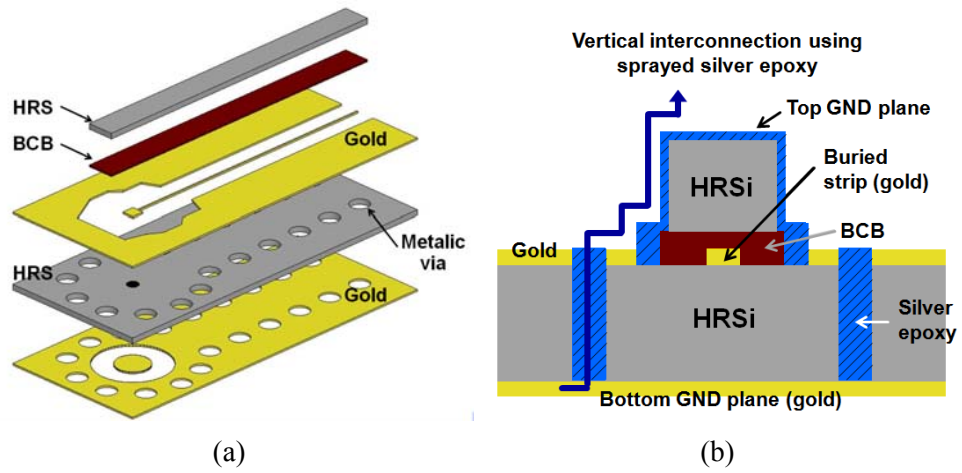
Fig. 3.3 (a) Three-dimensional view of the proposed applicator structure. (b) Cross-sectional view of the applicator structure.
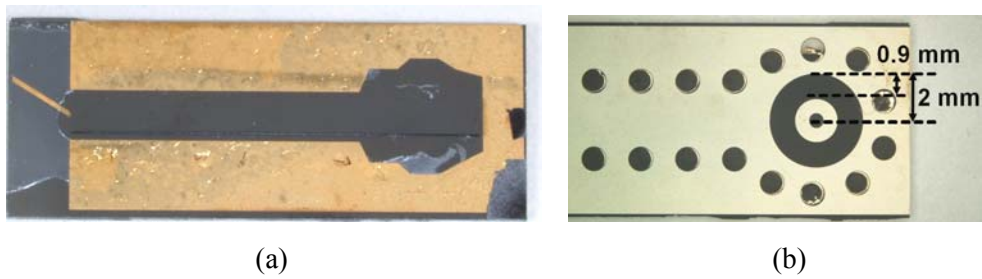


Fig. 3.4 (a) Photograph of the fabricated silicon heat applicator. (b) Enlarged view of the aperture on the backside of the probe.

Fig. 3.5 shows the measured return loss of the applicator. For the measurement, the aperture of the applicator was in contact with 4-mm-thick pork muscle. The return loss is better than 10 dB from 17 to 17.9 GHz. Heating experiment was also conducted on 4-mm-thick pork muscle for further verification of the applicator. As a microwave source, a broadband signal generator (Agilent E8257D) was used together with a wideband power amplifier (Microsemi, L0618-35). The microwave power delivered to the applicator was 2 W at 18 GHz. The temperature profile was monitored for 5 minutes at the surface of muscle using an infrared (IR) camera (FLIR Systems, ThermaCAM E25). As shown in Fig. 3.6, the peak temperature after 5-min heating was higher than 53 °C, high enough for hyperthermia.
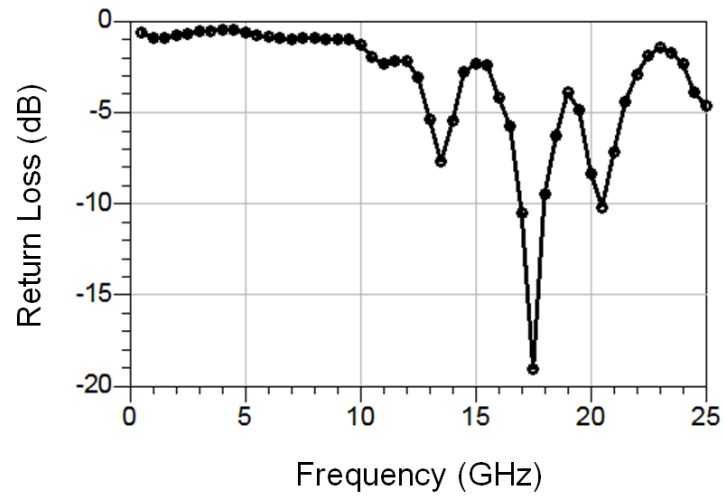
Fig. 3.5 Measured return loss of the applicator in contact with pork muscle.
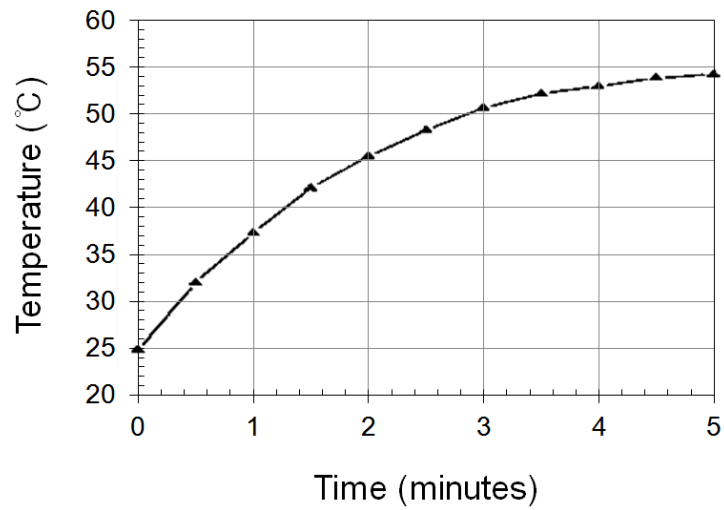


Fig. 3.6 Measured time evolution of surface temperature of the pork muscle.

### 3.2.2 Microwave Source

A *Ku*-band source is a VCO based on a source feedback topology. A buffer amplifier has been integrated after the VCO to obtain sufficient output power as well as to provide isolation from its load. The VCO was fabricated using 0.15-μm GaAs pHEMT commercial foundry. The photograph of the VCO chip is shown in Fig. 3.7. The chip size is 2.6 mm × 1.6 mm. As can be seen in Fig. 3.8, the VCO chip generates CW signal from 16.5 to 17.8 GHz with an output power higher than 11.6 dBm.
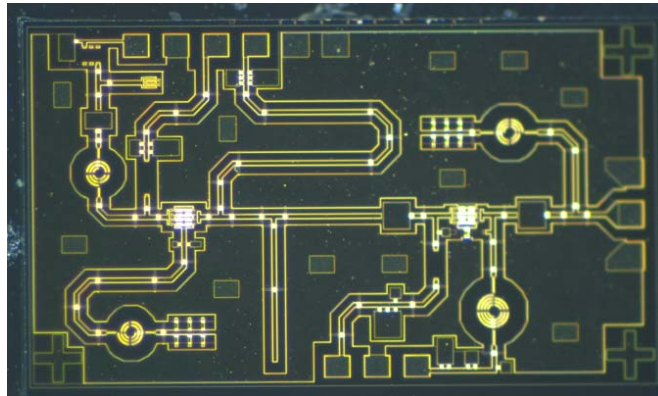


Fig. 3.7 Photograph of fabricated VCO chip with a size of 2.6 mm × 1.6 mm.
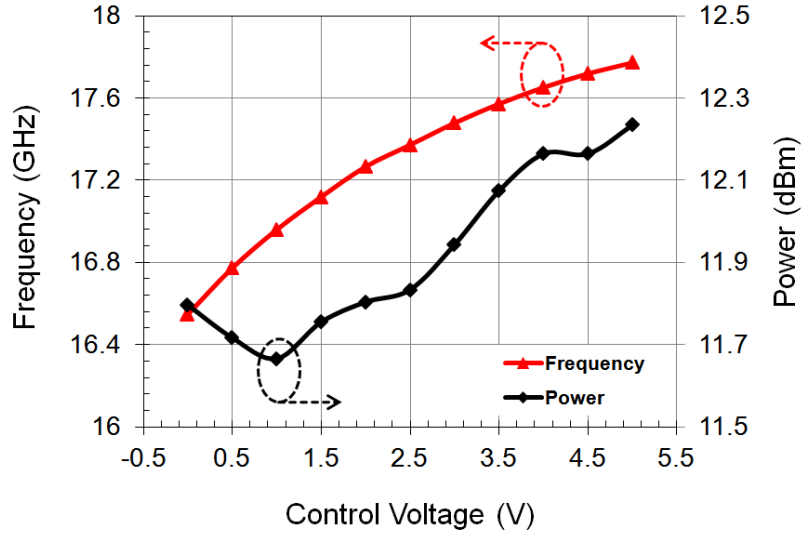
Fig. 3.8 Measured output characteristics of the VCO.

To deliver a watt-level *Ku*-band signal to cancer cells, a multi-watt MMIC PA is required. The amplifiers based on the stacked FET approach are integrated on the applicator [44], [45]. Generally, compared with current combining, voltage combining using the stacked FETs allows the output matching to be realized in the low Q-region and thus offers high output power and efficiency over a wide bandwidth. Fig. 3.9 shows the photograph of the PA chip fabricated using 0.15-μm GaAs pHEMT foundry. The chip size is 3.2 mm × 3.5 mm. As can be seen in Fig. 3.10, the PA provides a saturated output power of 33.7 dBm and an associated power

gain of 12.5 dB at 18 GHz. Preceding the PA, a stacked FET driver amplifier is also employed to boost the gain.

In general, the impedance of biological material is changed according to the temperature rise during hyperthermia. The delivered power from the PA is decreased due to the load-pull effects of the applicator, which results in degradation of heating efficiency. Furthermore, severe load mismatch may lead to self-oscillation or a permanent failure of the PA. To prevent these complications, a commercial circulator (Raditek, RADC-15.2-18.2-MS41-10WR) was added at the output of the PA. The insertion loss and isolation of the circulator are better than 1 dB and 18 dB from 17 to 18 GHz, respectively.
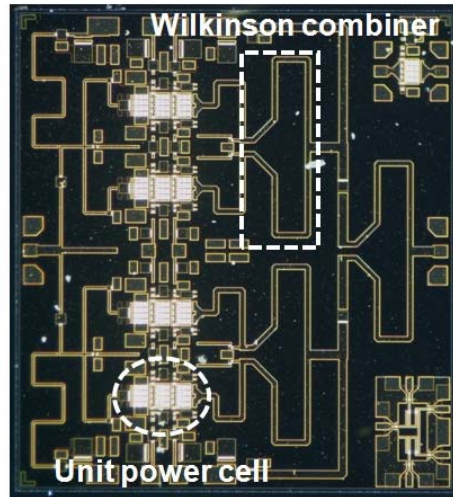
Fig. 3.9 Photograph of the stacked-FET PA chip.
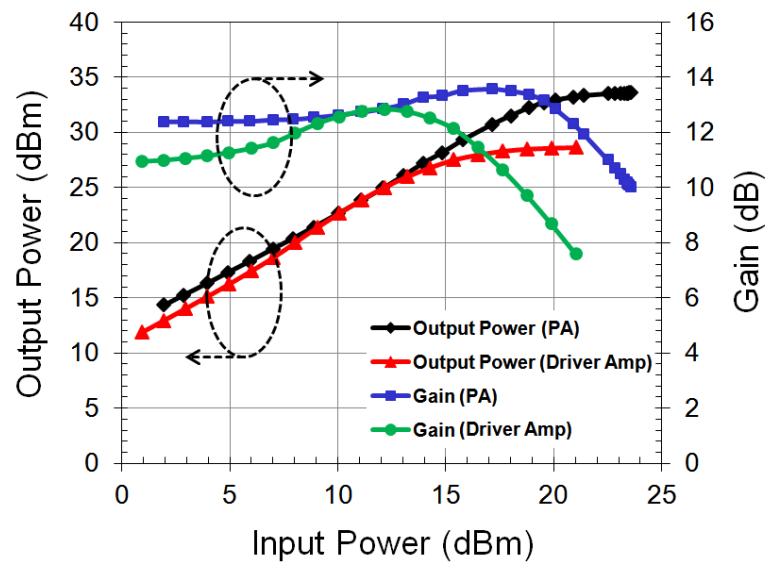


Fig. 3.10 Measured output power and power gain of the PA and driver amplifier at 18 GHz.

### 3.2.3 Power Monitoring Circuits

During hyperthermia, it is important to monitor the delivered and reflected power levels since heating efficiency can be estimated from these values. A directional coupler and two power detectors are employed for this purpose. The coupler has been designed based on a coupled line structure. It has been fabricated on the same silicon substrate as the applicator. The measured coupling is 21.6 dB at 18 GHz. The return loss and isolation are better than 20 dB and 33.4 dB, respectively.

The power detectors are connected to each arm of the directional coupler. They are the same chips as used in the integrated probe for permittivity measurement presented in section 2.3.4. The dynamic range of the power monitoring circuits is more than 40 dB (from -8.4 to 38.1 dBm), which is sufficient to accurately calculate the power delivery efficiency.

### 3.2.4 *Ku*-Band Active Integrated Applicator System

All of the aforementioned circuits are integrated on the micromachined applicator motherboard in a small footprint of 8 mm × 56 mm. The performances of the individual circuit components are summarized in Table 3.1. The chip interconnects were realized using the wire bonds. DC feed lines and the bypass capacitors were placed on the PCB (254-μm-thick RO4350B), on which the applicator motherboard was mounted. Fig 3.11 shows the photographs of the fabricated *Ku*-band integrated

applicator and entire hyperthermia system.

TABLE 3.1

| Circuit | Topology | Technology | Performances |
|---------|----------|------------|--------------|
| Applicator | Planar coaxial | Si MEMS | BW: 17-17.9 GHz<br>(Return loss > 10 dB) |
| VCO | Series feedback | GaAs pHEMT | BW: 16.5-17.8 GHz<br>$P_{sat}$ > 11.6 dBm |
| Driver amplifier | Stacked-FET | GaAs pHEMT | BW: 7.5-20.5 GHz<br>Gain > 14 dB |
| Power amplifier | Stacked-FET | GaAs pHEMT | BW: 9-22 GHz<br>$P_{sat}$ > 33.7 dBm (@ 18 GHz) |
| Power detector | Source-connected FET diode detector | GaAs pHEMT | BW: 2-18 GHz<br>Sensitivity > 0.24 mV/dB<br>(@ -30 dBm) |
| Coupler | Coupled line | Si MEMS | Coupling: 21.6 dB (@ 18 GHz)<br>Isolation > 33.4 dB |

BW: Bandwidth
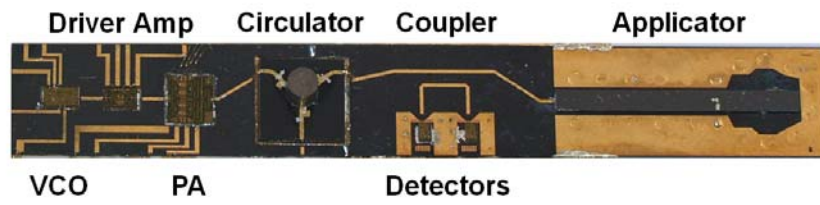
(a)
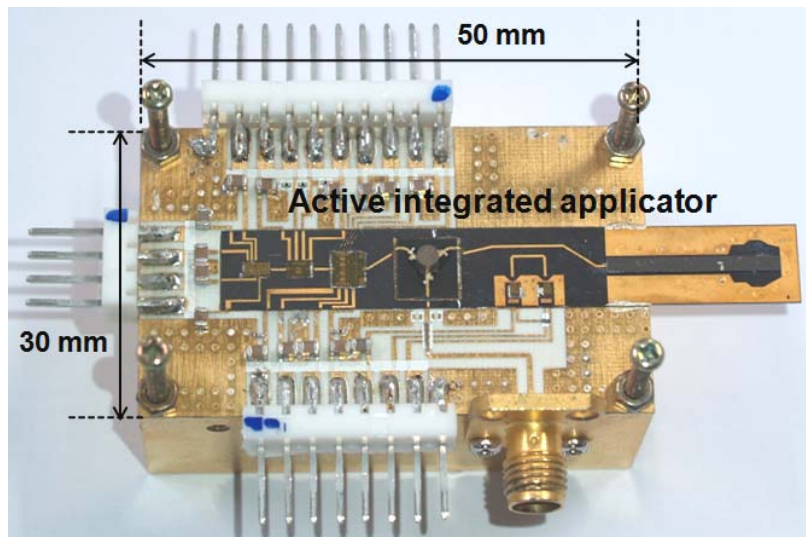


(b)

Fig. 3.11 Photographs of (a) fabricated *Ku*-band integrated applicator and (b) entire hyperthermia system.

## 3.3     Experiment  Results

To evaluate the performance of the proposed integrated hyperthermia system, heating experiments were performed using the experimental setup shown in Fig. 3.12. A Peltier cooler and a cooling fan have been attached to the backside of the hyperthermia module to effectively dissipate the heat generated by the PA, thereby preventing thermal conduction to material under test (MUT) (Fig. 3.13). Microwave ablations were performed on 4-mm-thick pork muscle and fat for 10 minutes. Pork muscle and fat were selected as MUT since they have dielectric characteristics very close to human breast cancer and fat, respectively [14].
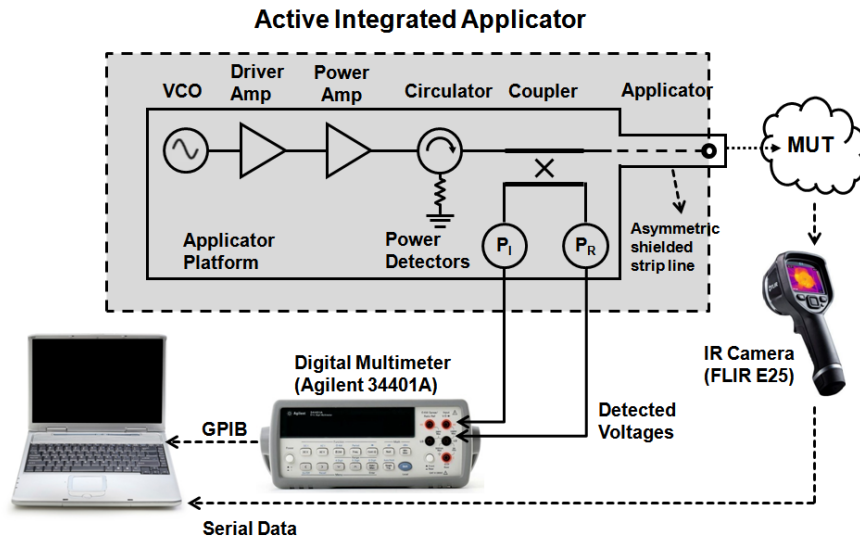


Fig. 3.12 Experimental setup for microwave hyperthermia using the proposed *Ku*-band integrated applicator.

The power delivered to the applicator is more than 1.2 W after the loss of the circulator and coupler. During the heating, the delivered and reflected power levels were monitored using the power detectors. The temperature profiles at the surface of the pork muscle and fat were measured using an IR camera (FLIR Systems, ThermaCAM E25) (Fig. 3.14). The measured surface temperatures of the pork muscle and fat are plotted in Fig. 3.15. After 10 min of heating, the temperature of the pork muscle was increased from 22 to 46 °C, a temperature high enough for hyperthermia. As the IR thermal image was taken at the surface of the pork muscle, the core temperature inside the pork muscle should be much higher than 46 °C. On the other hand, the temperature rise of the fat was only 6.9 °C. These results confirmed material-selective nature of hyperthermia using 15-20 GHz microwaves [6]. Fig. 3.16 shows the delivered and reflected power of pork muscle and fat during heat application. The reflected power for the fat was twice as much as that for the muscle, which was caused by the permittivity change of MUT during hyperthermia.
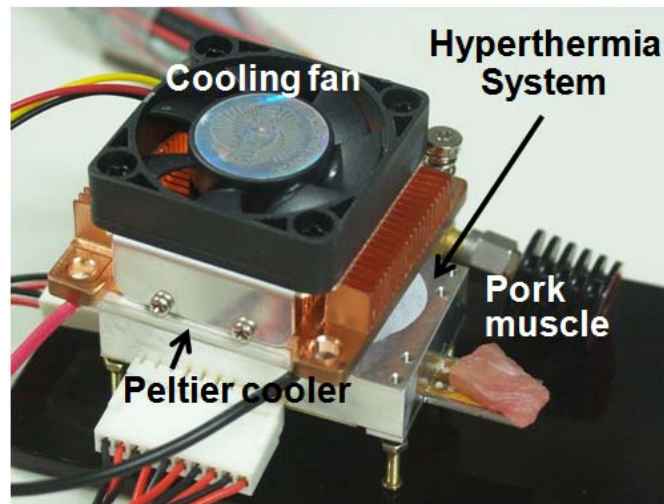
Fig. 3.13 Photograph of the assembled hyperthermia system heating pork muscle.
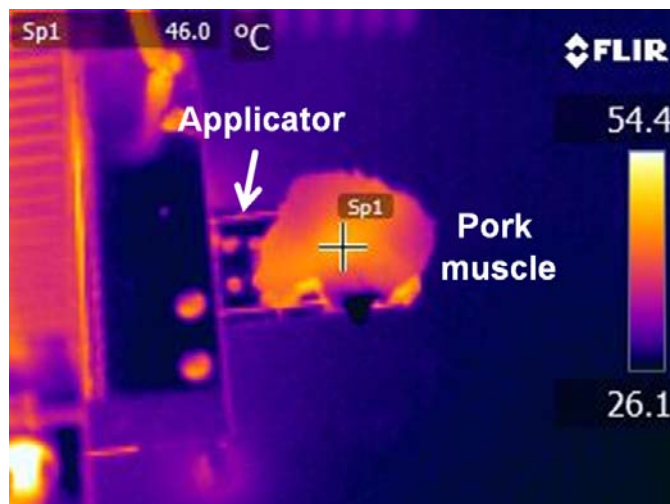


Fig. 3.14 IR image of the pork muscle after 10-min heating using the *Ku*-band integrated applicator.
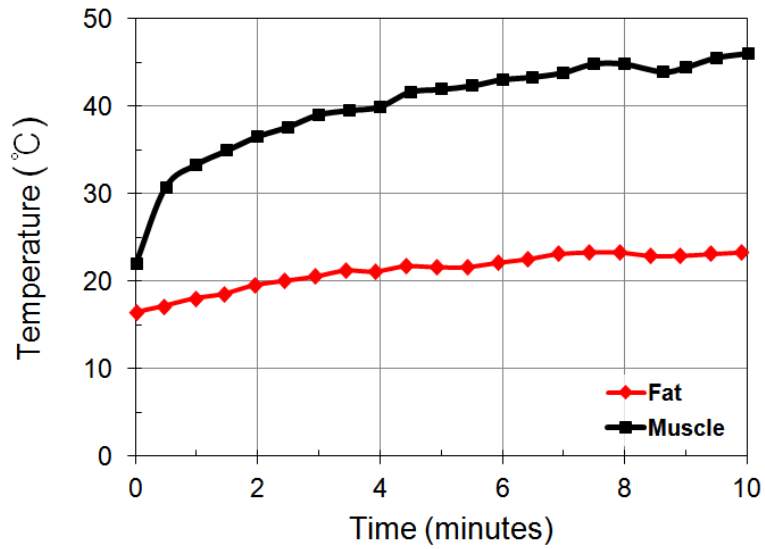
Fig. 3.15 Time evolution of surface temperatures of pork muscle and fat for 10 minutes.
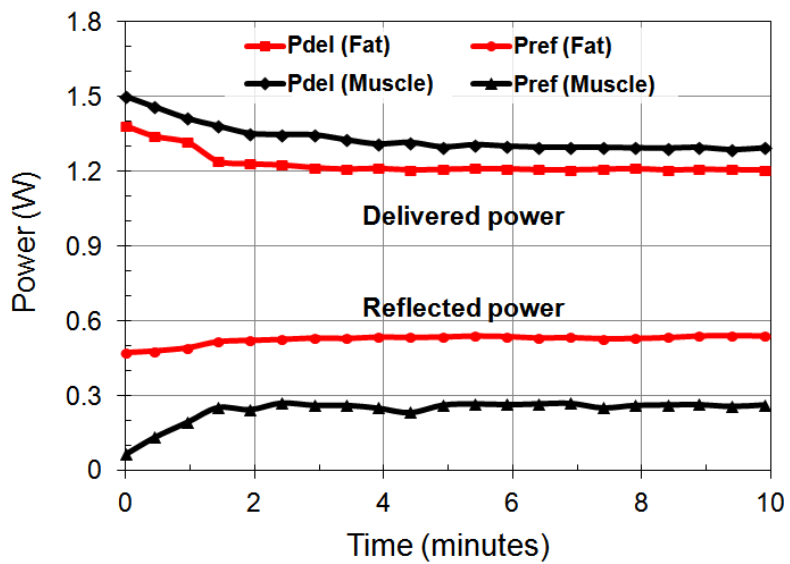


Fig. 3.16 Delivered and reflected power levels of pork muscle and fat during 10-min hyperthermia.

73

For ultimate verification, *in-vivo* thermal ablation was also performed on a nude mouse xenografted with human breast cancer. Using protocols approved by the Institutional Animal Care and Use Committee of Seoul National University, the human cancer cell line MDA MB 231 was used for implantation into the athymic nude mouse. The cell line was maintained in DMEM with 10% fetal bovine serum and 1% antibiotics. Cancer cells at a concentration of $4 \times 10^6$ were suspended in 0.3 mL of culture media and subcutaneously inoculated at the thigh. For the cancer ablation experiment, the integrated applicator was inserted into the cancer tissue after incision as shown in Fig. 3.17. Microwave power (~1.3 W) was applied to the center of the cancer for 21 minutes. The measured temperature profile of the cancer is plotted in Fig. 3.18. Fig. 3.19 shows the delivered power levels during 21-min hyperthermia. The temperature of the cancer rose from 25.8 to 46.5 °C after 21-min heating, which validated the practicality of the proposed integrated applicator system for hyperthermia.
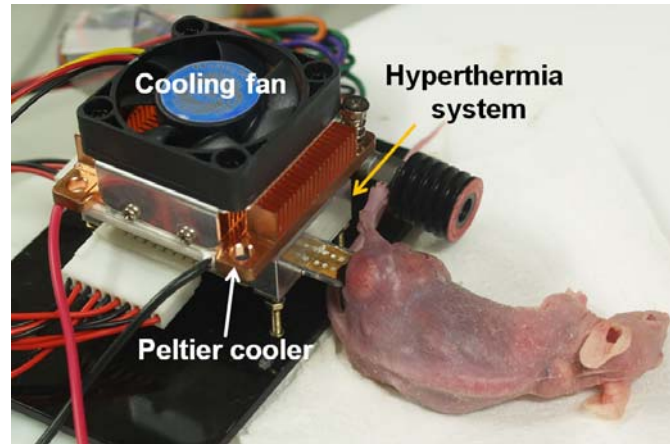
Fig. 3.17 Photograph of the nude mouse under hyperthermia using the proposed *Ku*-band integrated applicator.
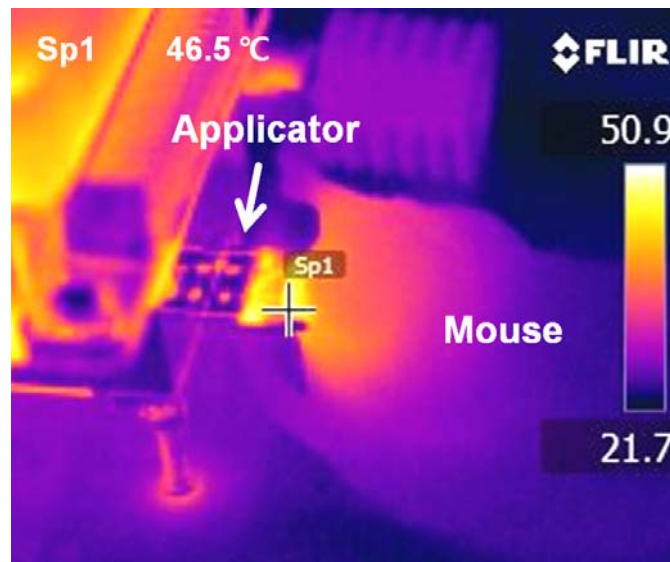


Fig. 3.18 IR image of the nude mouse after 21-min heating using the *Ku*-band integrated applicator.
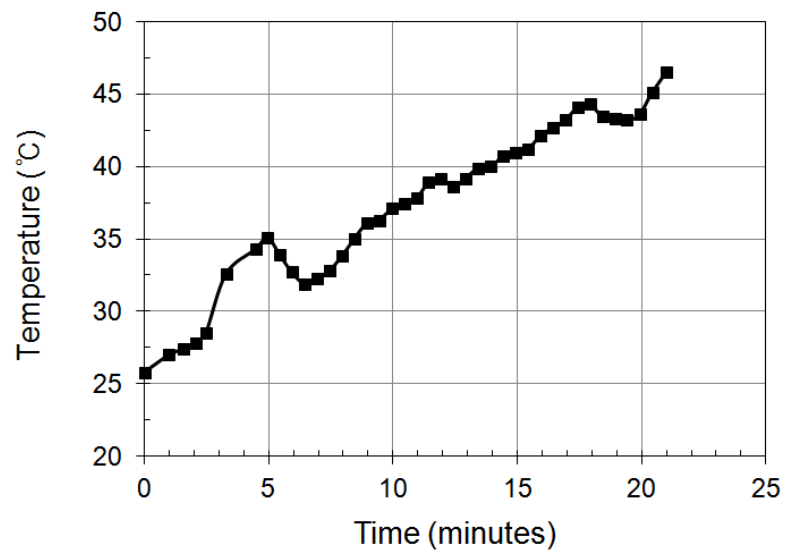
Fig. 3.19 Measured surface temperature of the nude mouse during *Ku*-band hyperthermic heating.
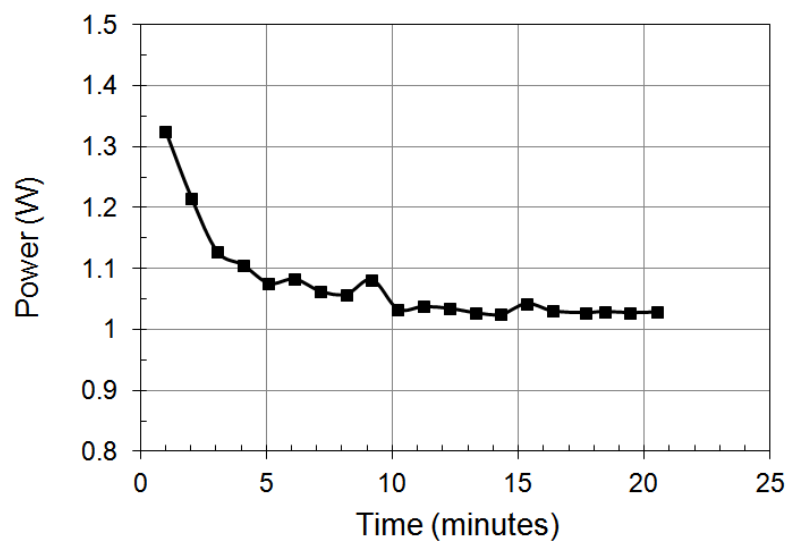


Fig. 3.20 Delivered power level of the nude mouse.

## 3.4    Summary

We have developed a fully integrated *Ku*-band miniaturized microwave hyperthermia system. For system miniaturization, a *Ku*-band microwave source consisting of a VCO, a driver amplifier, and a PA has been implemented in MMIC's, and integrated on a micromachined silicon heat applicator. A SIW-based strip line and a planar coaxial aperture are designed to effectively deliver microwave power in the cancer tissue at *Ku*-band frequencies. Power detectors provide delivered and reflected power levels during hyperthermia together with a directional coupler built into the applicator platform. The fully integrated system is realized in a small form factor of 8 mm × 56 mm × 0.6 mm.

To evaluate the performance of the integrated applicator, hyperthermia experiments were performed. In *in-vitro* experiments on pork muscle and fat, the temperature of the pork muscle was increased up to 46 °C after 10 minutes into microwave application, where as the peak temperature of the pork fat was only 23.3 °C. This clearly shows sufficient heating performance of the integrated applicator for cancer ablation, and also proves the possibility of material-specific hyperthermia using *Ku*-band microwaves. In addition, *in-vivo* cancer ablation experiment on a nude mouse xenografted with human breast cancer demonstrates the feasibility of a low-power hyperthermia for localized treatment using the integrate applicator. It is worthwhile to note that the required source power is much lower (< 2

W) compared with the low-frequency ablation methods at KHz and MHz. Therefore, the low-power microwave hyperthermia at *Ku*-band can offer an effective and safe method for localized cancer treatment by reducing the potential risk to patients and clinicians.

# Chapter 4

# Active Integrated Heat Applicator for Magnetic Nanoparticle - Assisted Hyperthermia

## 4.1    Introduction

Microwave hyperthermia is an effective method for localized cancer ablation since it can offer material-specific responsiveness and sensitivity. It is based on the fact that there is an obvious difference in their electromagnetic properties between cancerous and normal tissues [3]. Therefore, microwave hyperthermia is well suited to the cancer having higher dielectric loss than adjacent normal tissue does, such as breast cancer. As demonstrated in chapter 3, microwave hyperthermia can provide low-power and high-efficiency cancer ablation by using *Ku*-band frequencies to maximize microwave power absorption in the cancer cells.

In general, however, the dielectric properties of the cancer cells are not obviously different from those of surrounding normal tissues in case of liver, kidney, heart, and so on [47]. This is the main reason for material-sensitivity degradation and uncontrolled collateral damage to healthy tissues in microwave hyperthermia. Thus, microwave hyperthermia has not yet established clinical practicality, and still remains mostly as a topic of academic research. To expand its application range, it is necessary to further improve the efficiency and material-sensitivity.

There have been extensive studies to improve microwave power absorption in cancer cells for cancer-specific hyperthermia. Magnetic nanoparticle (MNP) has been emerging as a promising candidate since it can provide local enhancement of contrast and sensitivity without biocompatibility problems [15], [55], [56]. The magnetic loss of MNP's helps to increase the specific absorption rate (SAR) or specific loss power (SLP), thereby generating more heat energy in the tissue [57], [58]. However, high power absorption in the tissue cannot directly guarantee the enhancement of hyperthermia since the effect of hyperthermia is determined not by the absorbed power, but by the thermal dose to the tissue, such as cumulative equivalent minutes at 43 °C (CEM 43 °C). For this reason, a thermal analysis should be performed along with an electromagnetic analysis to evaluate the effect of MNP's on microwave hyperthermia.

In this work, a coupled electromagnetic-thermal analysis is carried out

considering temperature-dependent electromagnetic properties of biological material. The temperature rise of the tissue irradiated by microwave energy is estimated by the coupled analysis. The effect of MNP's is investigated by comparing the temperature rises of tissues with and without MNP's, from which microwave frequency is optimized to improve material selectivity in MNP-assisted hyperthermia.

In order to demonstrate the feasibility of this approach, we have performed heating experiments on agar phantoms and pork muscles using a developed active integrated heat applicator. A microwave source consisting of a voltage controlled oscillator (VCO) and a power amplifier (PA) is implemented in monolithic microwave integrated circuits (MMIC's), and integrated on a heat applicator platform. A CMOS power detector is also employed to monitor power levels of delivered and reflected microwaves. To the best of our knowledge, this is the first study on the optimization of MNP-assisted microwave hyperthermia based on a coupled electromagnetic-thermal analysis.

## 4.2 Magnetic Nanoparticle (MNP)

For microwave hyperthermia using MNP's, we use polyacrylic acid-coated magnetite ($Fe_3O_4$) nanoparticle since it is a nontoxic and biocompatible material with a strong magnetic property [59]. The MNP's are synthesized using a polyol method, which is efficient for preparation of nano-sized metal or oxide particle of various shapes and sizes [60]. The synthesized magnetite MNP's are of a spherical shape with a mean diameter of 63 nm. Fig. 4.1 shows the TEM image of the synthesized magnetite MNP's.
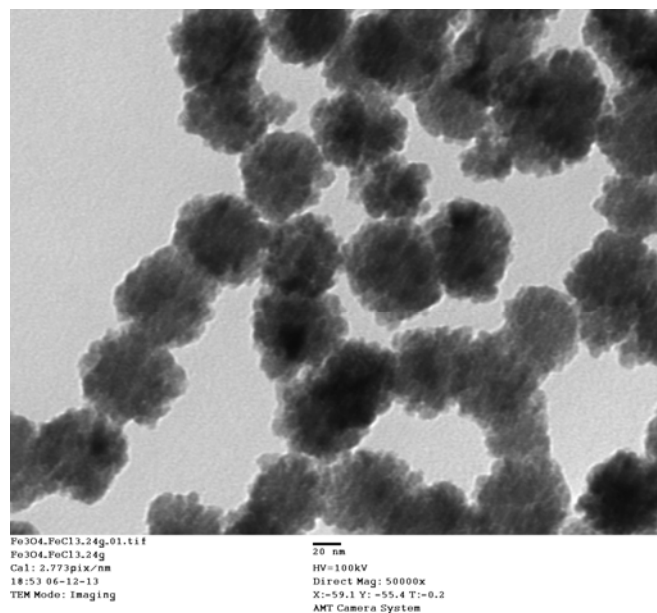


Fig. 4.1 TEM image of synthesized magnetite MNP's with a diameter of 63 nm.

## 4.2.1  Heating mechanism of MNP

The magnetic properties of the MNP's are characterized by three different mechanisms: Néel and Brownian relaxations, and ferromagnetic resonance [61]-[65]. Néel relaxation is caused by reorientation of the magnetic moment inside the MNP against an anisotropy energy barrier. On the other hand, Brownian relaxation is related to mechanical rotation of the MNP itself in the carrier medium. Ferromagnetic resonance is the phenomenon due to precessional motion of the magnetic dipole. In general, the magnetic loss of MNP's at low frequency below 10 MHz is mainly caused by Néel and Brownian relaxations, whereas the loss from the ferromagnetic resonance is dominant at GHz range. The frequency dependence of the magnetic properties is described in terms of the complex susceptibility, $\chi$, whose imaginary part accounts for the overall loss from all the mechanisms. The susceptibility is expressed by the following equation [61]-[65]:

$$\chi(\omega) = \frac{\chi_{\parallel}(\omega) + 2\chi_{\perp}(\omega)}{3} \tag{4.1}$$

where $\chi_{\parallel}(\omega)$ is the longitudinal susceptibility related to the relaxations, and $\chi_{\perp}(\omega)$ is the transverse susceptibility related to the ferromagnetic resonance. The longitudinal susceptibility for mono-dispersed MNP's can be modeled by the Debye

83

equation describing the magnetic dispersion [61], [62]:

$$\chi_\parallel(\omega) = \frac{\chi_{\parallel 0}}{1 + j\omega\tau_{eff}}$$ (4.2)

where $\chi_{\parallel 0}$ is the static longitudinal susceptibility, and $\tau_{eff}$ is the effective relaxation time. The transverse susceptibility is given by

$$\chi_\perp(\omega) = \chi_{\perp 0}\frac{\omega_0^2(1+\alpha^2) + j\alpha\omega\omega_0}{\omega_0^2(1+\alpha^2) - \omega^2 + 2j\alpha\omega\omega_0}$$ (4.3)

where $\chi_{\perp 0}$ is the static transverse susceptibility, $\omega_0$ is the resonance frequency, and $\alpha$ is the effective damping constant of the precession damping [61], [62]. The overall susceptibility $\chi(\omega)$ in equation (4.1) can be obtained from the complex permeability $\mu(\omega)$ using the relation, $\chi(\omega) = \mu(\omega) - 1$.

## 4.2.2  Permeability of MNP

In order to establish the feasibility of the MNP for microwave hyperthermia, we have measured the permeability of aqueous solution of the MNP's with the concentration of 5 mg/mL. A two-port coaxial transmission line probe is used since

it has a simple structure appropriate to measure liquid materials [66]. The two-port probe is a partially unshielded transmission line with attached shielded coaxial lines at both ends as shown in Fig. 4.2(a). The probe has been fabricated using a polytetrafluoroethylene (PTFE) semi-rigid coaxial cable of 50-ohm characteristic impedance. The inner and outer radii of the coaxial conductors are 0.455 mm and 1.53 mm, respectively. The length of the unshielded line is 1.8 mm. Two 1-mm-width slits are cut in the outer ground conductor, which allow the solution of MNP's to flow in and out of the probe. Fig. 4.2(b) shows the photograph of the fabricated two-port coaxial probe. A material container is installed surrounding the probe, and two supporting bars are attached to withstand bending of the probe.

(a)



(b)
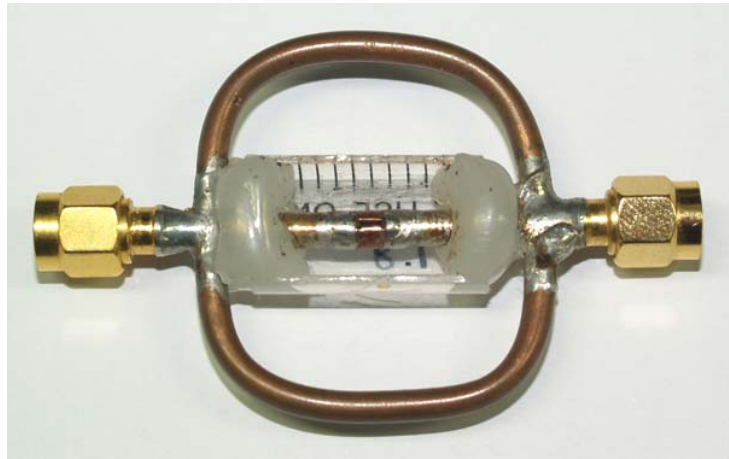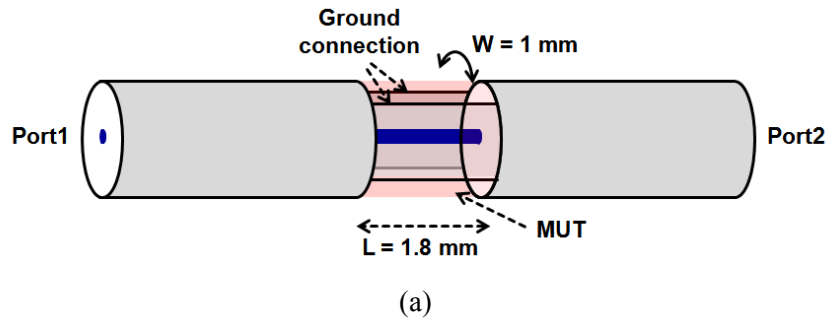
Fig. 4.2 Two-port coaxial probe for permeability measurement: (a) detailed physical structure and (b) photograph of the fabricated coaxial probe.

The S-parameters of the MNP solution with a concentration of 5 mg/mL were measured using an Agilent E8361A vector network analyzer (VNA) from 0.5 to 4 GHz. Unknown networks from the shielded coaxial lines and SMA connectors were deembedded by measuring standard calibration materials (air, methanol, and deionized water). The permeability was obtained by the method presented in [66]. The measured complex permeability of the MNP solution is plotted in Fig. 4.3. Magnetic loss of the MNP's reaches its maximum in the frequency range from 1.7 to 2 GHz, which can be a candidate frequency band to enhance the heating efficiency of MNP-assisted hyperthermia.
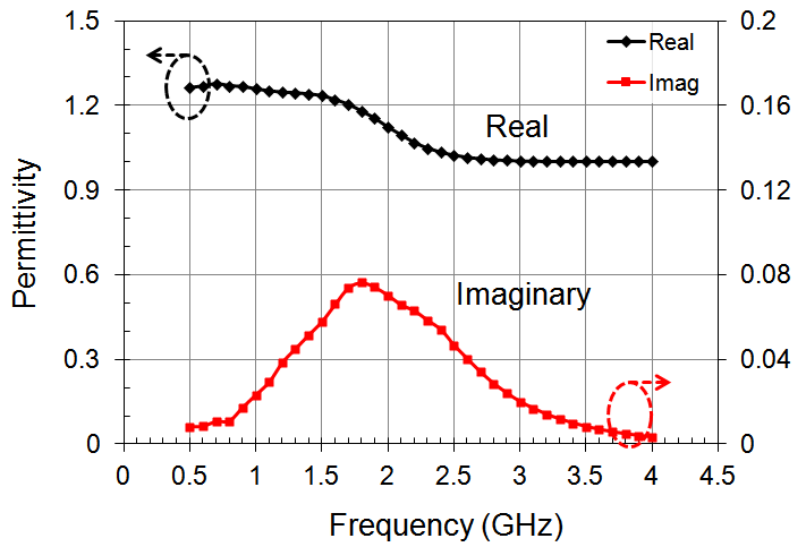


Fig. 4.3 Measured permeability of the 63-nm MNP solution from 0.5 to 4 GHz.

## 4.3　Coupled Electromagnetic-Thermal Analysis

The mechanism of microwave hyperthermia is based on heating by electromagnetic waves absorbed in biological tissues. Heating efficiency depends on the dielectric and magnetic properties of the tissue. Since biological materials have frequency-dependent properties due to the dielectric relaxation, the heating efficiency may vary according to the hyperthermia frequency. There have been various studies to determine the optimum frequency for microwave hyperthermia. Efficient hyperthermia frequencies have been proposed considering the dielectric loss of cancer cells [14], impedance matching between the applicator and tissue [67], and heat generation of MNP [68]. However, most of them cannot guarantee high-efficiency hyperthermia since they are based on a static set of tissue properties, which do not account for their changes due to the temperature variation during hyperthermia. Especially, biological tissues with high water content undergo dehydration and vaporization at high temperature, which cause significant decrease of the permittivity.

### 4.3.1　Coupled Electromagnetic-Thermal Problems

For assessment of the heating performance of the MNP's, we have calculated the transient temperature rise of the tissue with and without MNP's by solving coupled electromagnetic-thermal problems. A one-dimensional layered tissue model is used

to simplify the calculation [69]. In order to analyze nonuniform microwave power absorption and temperature rise in the tissue, the model consists of infinitesimally thin layers as shown in Fig. 4.4. Each layer is assumed to be homogeneous with uniform local properties, such as temperature, permittivity, permeability, and thermal conductivity. The calculation procedure is summarized as the flow chart in Fig. 4.5. First, the distribution of electric and magnetic fields ($E_i$, $H_i$) in the tissue is obtained based on the general solution of the one-dimensional wave in the planarly layered media [70]. Then, the absorbed power deposition profile can be derived, which acts as the distributed heat source inside the tissue. Transient temperature rise during an infinitesimal time interval ($\Delta t$) is estimated by solving the bio-heat transfer equation [71]. Finally, the tissue properties are updated by the corresponding temperature and the iteration for the next time interval is repeated.
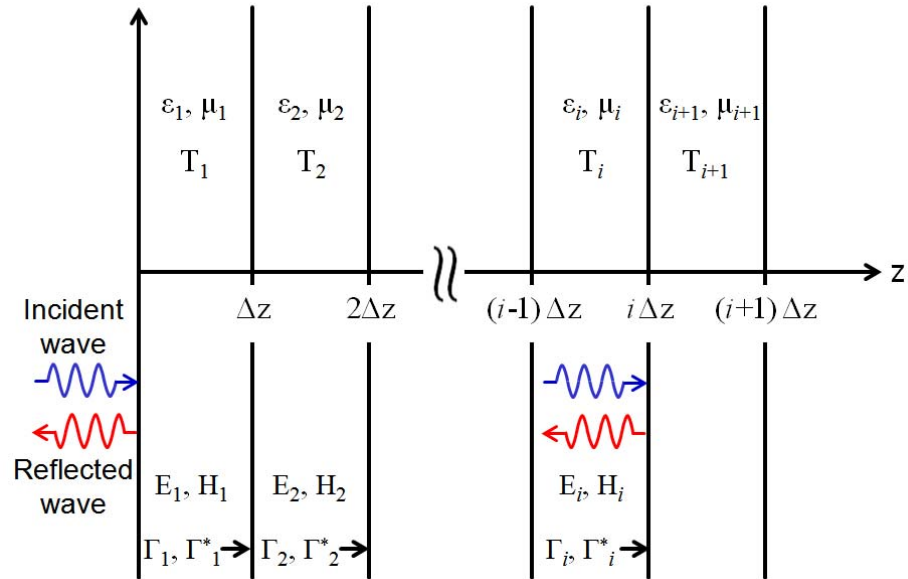
Fig. 4.4 One-dimensional layered tissue model for the coupled electromagnetic-thermal analysis.
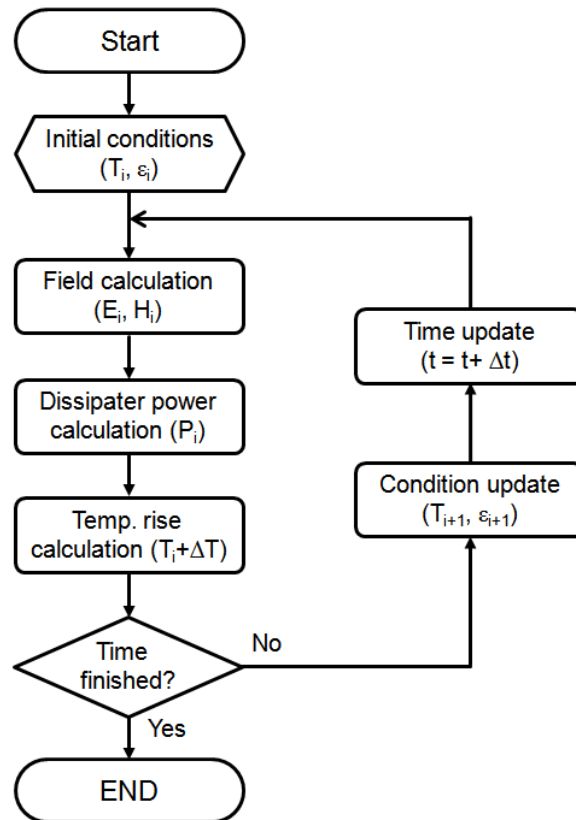
Fig. 4.5 Flow chart of the calculation of coupled electromagnetic-thermal problems.

## 4.3.2 Electromagnetic Analysis

The electromagnetic wave for hyperthermia is applied at $z=0$ and propagates in the $z$ direction as shown in Fig. 4.4. Under the assumption of plane wave propagation, the electric field $E_i$ in the $i^{th}$ layer element with the thickness of $\Delta z$ is described in [70] as

$$E_i = A_i [e^{-jk_i z_i} + \tilde{\Gamma}_i e^{-j(2k_i i\Delta z - k_i z_i)}] \qquad ( i\Delta z < z_i < (i+1)\Delta z ) \quad (4.4)$$

where $A_i$ is the amplitude of the incident wave in the $i^{th}$ layer element, $k_i$ is the wavenumber, and $\tilde{\Gamma}_i$ is the overall reflection coefficient at $z=(i+1)\Delta z$ seen from the $i^{th}$ layer. By imposing continuity conditions at the layer interface, the unknown values of $A_i$ and $\tilde{\Gamma}_i$ can be calculated as following recursive relations:

$$\tilde{\Gamma}_i = \frac{\Gamma_i + \tilde{\Gamma}_{i+1} e^{-2j k_{i+1} \Delta z}}{1 + \Gamma_i \tilde{\Gamma}_{i+1} e^{-2j k_{i+1} \Delta z}}$$

$$A_i = A_{i-1} \frac{1 + \Gamma_{i-1}}{1 + \Gamma_{i-1} \tilde{\Gamma}_i e^{-2j k_i \Delta z}} e^{-j (k_{i-1} - k_i)\Delta z}. \qquad (4.5)$$

Here $\Gamma_i$ is the local reflection coefficient of the $(i+1)^{th}$ layer seen from the $i^{th}$, which is given by

$$\Gamma_i = \frac{\eta_{i+1} - \eta_i}{\eta_{i+1} + \eta_i} = \frac{\sqrt{\mu_{i+1}\varepsilon_i} - \sqrt{\mu_i\varepsilon_{i+1}}}{\sqrt{\mu_{i+1}\varepsilon_i} + \sqrt{\mu_i\varepsilon_{i+1}}} \tag{4.6}$$

where $\eta_i$ is the intrinsic impedance of the $i^{\text{th}}$ layer, and $\varepsilon_i$, $\mu_i$ are the permittivity and permeability, respectively.

Using equations (4.4)-(4.6), the electric and magnetic fields are obtained as follows:

$$E_i = A_i\,(1+\tilde{\Gamma}_i)\,e^{-jk_i\,i\Delta z}$$
$$H_i = \frac{A_i}{\eta_i}\,(1-\tilde{\Gamma}_i)\,e^{-jk_i\,i\Delta z}. \tag{4.7}$$

Therefore, the dissipated microwave power in the $i^{\text{th}}$ layer element is given by

$$Q_i = \frac{1}{2}\omega(\varepsilon_0\varepsilon''_i\,|E_i|^2 + \mu_0\mu''_i\,|H_i|^2) \tag{4.8}$$

which corresponds to the local heat source during a time interval $\Delta t$. The local SAR representing the standard measure of the heating performance in microwave hyperthermia can be expressed as

$$\text{SAR} = \frac{1}{2\rho_i}\omega(\varepsilon_0\varepsilon''_i|E_i|^2 + \mu_0\mu''_i|H_i|^2) = \frac{Q_i}{\rho_i} \qquad (4.9)$$

where $\rho_i$ is the tissue density.

### 4.3.3 Thermal Analysis

Transient temperature rise in the tissue is obtained by the solution of the bio-heat transfer equation [71]:

$$\rho_t c_t \frac{\partial T_i}{\partial t} = k\nabla^2 T_i + \omega_b \rho_b c_b (T_a - T_i) + Q_m + Q_i \qquad (4.10)$$

where $\rho_t$ and $c_t$ are the density and specific heat of the tissue, $T_i$ is the temperature of the $i^{\text{th}}$ tissue layer, $k$ is the thermal conductivity of the tissue, $\omega_b$ is the blood perfusion rate, $\rho_b$ is the density of blood, $c_b$ is the specific heat of blood, $T_a$ is the arterial temperature, and $Q_m$ is the metabolic heat generation. To apply the bio-heat equation to the layered tissue model, we have used one-dimensional bio-heat transfer equation without the metabolic effect, which is given by

$$\rho_t c_t \frac{\partial T_i(z,t)}{\partial t} = k \frac{\partial^2 T_i(z,t)}{\partial z^2} + \omega_b \rho_b c_b (T_a - T_i(z,t)) + Q_i(z,t). \quad (4.11)$$

The solution of equation (4.11) can be expressed using Green's function $G(z',t'; z,t)$ and heat source term $Q_i(z',t')$ as

$$T_i(z,t) = \int_{t'=0}^{t} \int_{z'} \frac{1}{\rho_t c_t} Q_i(z',t') \, G(z',t';z,t) dz' dt'. \quad (4.12)$$

The Green's function $G$ is determined to satisfy the following relation [72]:

$$\frac{\partial G}{\partial t} - \frac{k}{\rho_t c_t} \frac{\partial^2 G}{\partial z^2} + \frac{\omega_b \rho_b c_b}{\rho_t c_t} G = \delta(z-z')\delta(t-t') \quad (4.13)$$

where $\delta$ is the Dirac delta function. By applying the Fourier transform with respect to $z$ on equation (4.13), the Green's function $G$ can be obtained, which is given by

$$G = \frac{H(t-t')}{\sqrt{4\pi(k/\rho_t c_t)(t-t')}} \exp(-\frac{(z-z')^2}{4(k/\rho_t c_t)(t-t')} - \frac{\omega_b \rho_b c_b}{\rho_t c_t}(t-t')) \quad (4.14)$$

where $H(t-t')$ is the unit step function:

$$H(t-t')=\begin{cases}1 & (t\geq t')\\0 & (t<t')\end{cases}.$$ (4.15)

If time is discretized by the time interval $\Delta t$, the temperature profiles in the tissue expressed by equation (4.12) can be rewritten using equation (4.14) as the following summation equation:

$$T_i(z,t=n\Delta t)=T_0+\sum_{h=0}^{n}\sum_{l=0}^{m}\left[\frac{Q_i(l\Delta z,h\Delta t)}{\rho_t c_t}\frac{1}{\sqrt{4\pi(k/\rho_t c_t)(n-h)\Delta t}}\times\right.$$
$$\left.\exp(-\frac{(z-l\Delta z)^2}{4(k/\rho_t c_t)(n-h)\Delta t}-\frac{\omega_b\rho_b c_b}{\rho_t c_t}(n-h)\Delta t)\Delta z\Delta t\right]$$ (4.16)

where $T_0$ is the initial temperature of the $i^{th}$ layer at $t$=0 sec.

## 4.3.4 Analysis Results

We have analyzed the effect of the MNP's on the heating performance using equations (4.8) and (4.16). In the analysis, pork muscle is used for the biological tissue due to the similar electromagnetic and thermal properties to the human cancer. The thermal conductivity $k$, density $\rho_t$, and specific heat $c_t$ are assumed to be constant in the temperature range of interest (20-100 °C). The permeability variation

of the MNP's according to the temperature is not so large as to introduce significant error in temperature estimation since the Curie temperature of magnetite (585 °C) is much higher than the tissue temperature under hyperthermia [73]. Hence, the permeability is also assumed to be equal to the permeability of MNP solution measured at room temperature (25 °C). The permittivity of the tissue is taken into account as the only parameter that is changed with the temperature.

We measured the permittivity of the pork muscle at various temperatures from 25 to 95 °C. The permittivity was obtained using an open-ended coaxial probe and VNA (Agilent E8361A), while heating the pork muscle on a hot plate. The temperature of the pork muscle was monitored using an optic temperature sensor (Luxtron m822) to minimize the interference in the permittivity measurement. Fig. 4.6 shows the measured permittivities of the pork muscle in the frequency range from 0.5 to 10 GHz. As the temperature increases from 25 to 95 °C, the real and imaginary part of the permittivity at 2 GHz decrease from 49.2 and 17.3 to 15.5 and 7.1, respectively. These permittivity changes may reduce the delivered power to the tissue due to the impedance mismatch between the tissue and applicator, resulting in heating efficiency degradation in microwave hyperthermia.
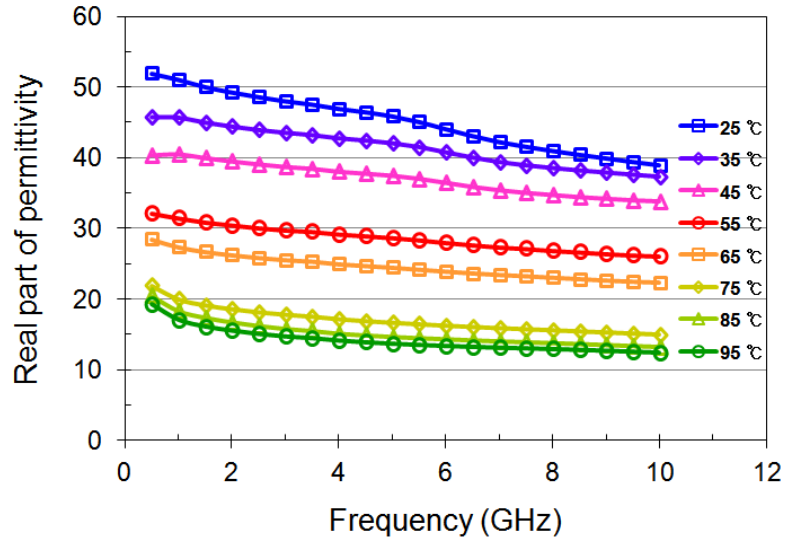
(a) Real part of the permittivities
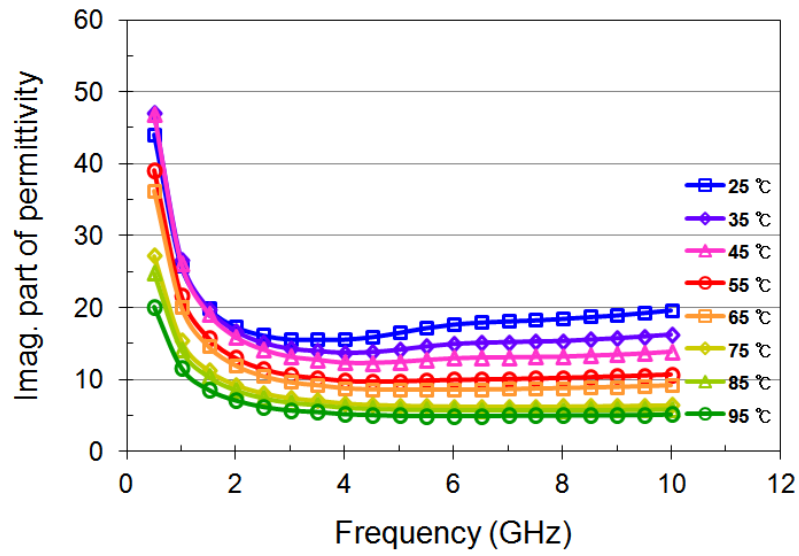


(b) Imaginary part of the permittivities

Fig. 4.6 Measured complex permittivities of pork muscle at various temperatures from 25 to 95 °C.

Based on the temperature-dependent permittivity, the transient temperature profiles in the tissue are simulated following the procedure described above. The material properties of pork muscle are $k = 0.5$ W/(m·°C), $\rho_t = 1100$ kg/m$^3$, and $c_t = 3700$ J/(kg·°C) [74], [75]. The microwave frequency is 2 GHz, and the applied power density is 1.45 W/cm$^2$. The calculated 5-mm temperatures of the tissues with and without MNP's are compared in Fig. 4.7. The temperature of the tissue with MNP's increases from 25 to 47 °C for 5 minutes, whereas the tissue without MNP's shows the temperature rise only up to 42.5 °C. When the applied power density to the tissue without MNP's is increased to 1.65 W/cm$^2$ to deliver the same power as the tissue with MNP's, its 5-min temperature is slightly increased to 44.4 °C. This is attributed to the difference in the absorbed power density inside the tissue as shown in Fig. 4.8. The tissue with MNP's attains high power density near the surface of the tissue.
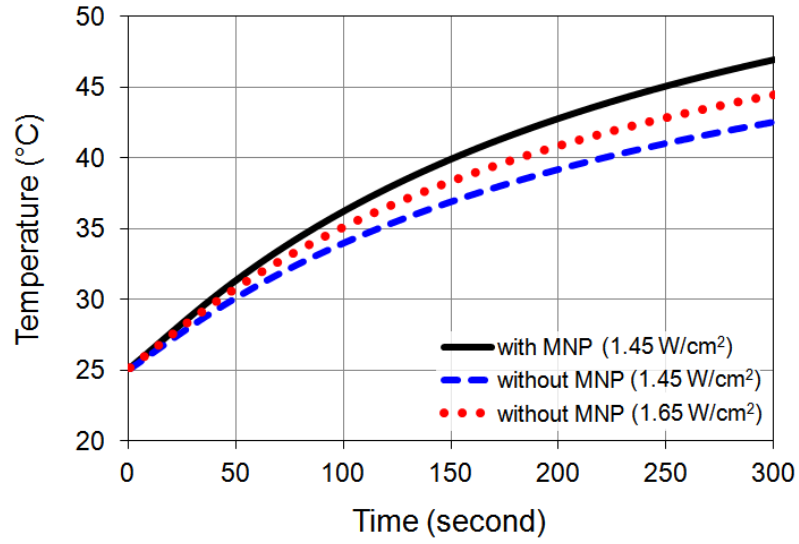
Fig. 4.7 Simulated 5-mm temperatures of tissues with and without MNP's.
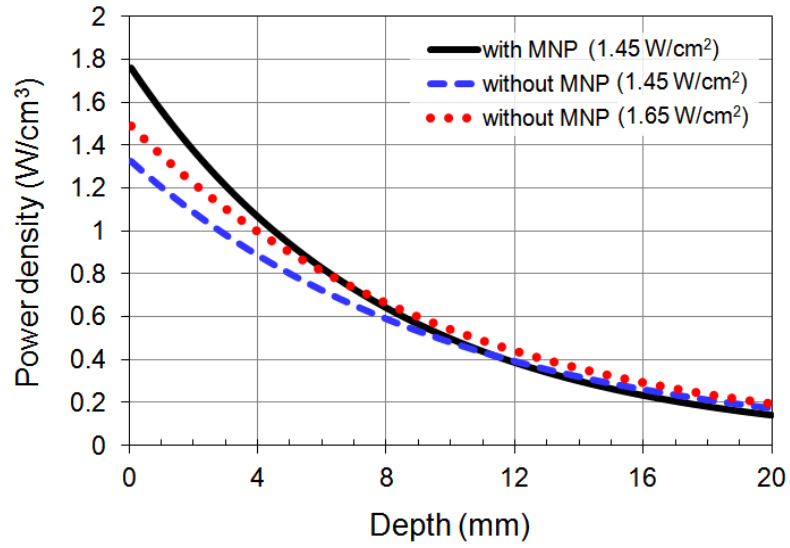


(a) $t = 0$ sec

Fig. 4.8 Simulated absorbed power densities of tissues with and without MNP's according to depth $z$.
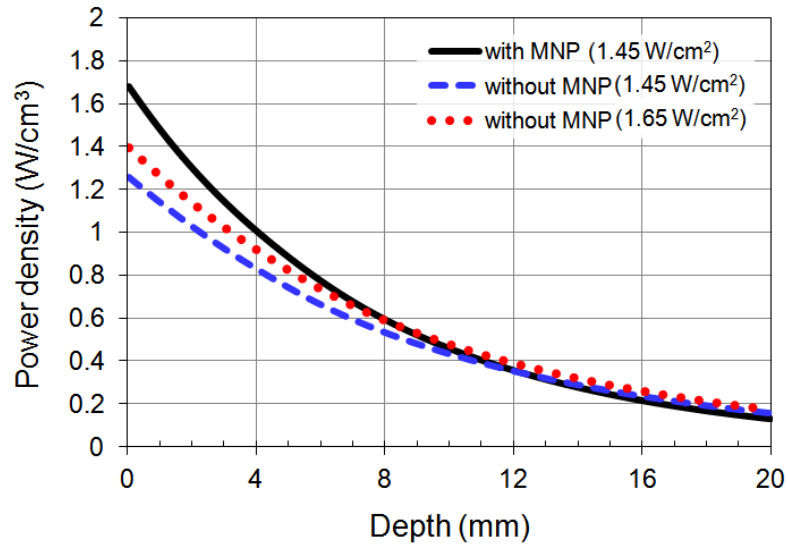
(b) $t$ = 150 sec
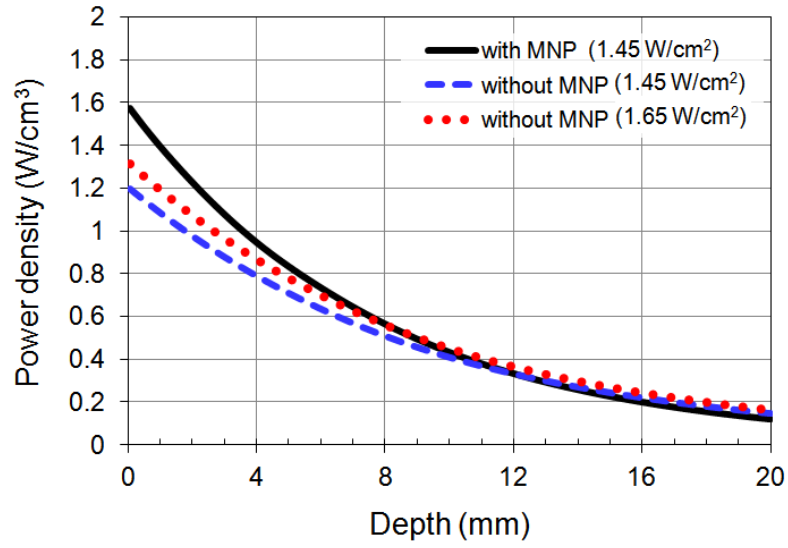


(c) $t$ = 300 sec

Fig. 4.8 Simulated absorbed power densities of tissues with and without MNP's according to depth $z$.

In order to optimize the hyperthermia frequency, we have estimated the tissue temperatures at various frequencies from 1.6 to 3 GHz. For fair comparison, delivered power at each frequency is set to be equal to each other (1.45 W/cm$^2$). The results are summarized in Table. 4.1. Although the temperature rise of the tissue with MNP's is highest at 2.8 GHz, the ratio of temperature rises between the tissues with and without MNP's reaches its peak at 2 GHz. Therefore, we have used 2 GHz as hyperthermia frequency for better material sensitivity.

TABLE 4.1

COMPARISON OF TEMPERATURE RISES AT VARIOUS FREQUENCIES FROM 1.6 TO 3 GHz

| Frequency (GHz) | With MNP's ($T_W$ °C) | Without MNP's ($T_{W/O}$ °C) | Ratio of temperature rise $(\frac{T_W - T_0}{T_{W/O} - T_0})$ |
|---|---|---|---|
| 1.6 | 44.93 | 43.20 | 1.095 |
| 1.8 | 46.96 | 44.68 | 1.116 |
| 2.0 | 46.96 | 44.44 | 1.130 |
| 2.2 | 46.98 | 44.79 | 1.111 |
| 2.4 | 47.31 | 45.42 | 1.093 |
| 2.6 | 46.55 | 45.18 | 1.068 |
| 2.8 | 47.98 | 46.95 | 1.047 |
| 3.0 | 47.04 | 46.29 | 1.035 |

$T_0$ = 25 °C (initial temperature)

## 4.4    Design and Fabrication

In order to demonstrate the feasibility of MNP-assisted microwave hyperthermia, an active integrated applicator system is realized by integrating a VCO, a PA module, power detectors, and a directional coupler on a spiral heat applicator. The block diagram of the integrated applicator is shown in Fig. 4.9. Based on the analysis in section 4.3, all the components have been designed at 2 GHz. For high-level system integration, the PA module is implemented by integrating a PA chip and an external matching network on a daughter board. The VCO and power detectors have been realized in a single chip MMIC. The details of the circuit design are presented in the following subsections.
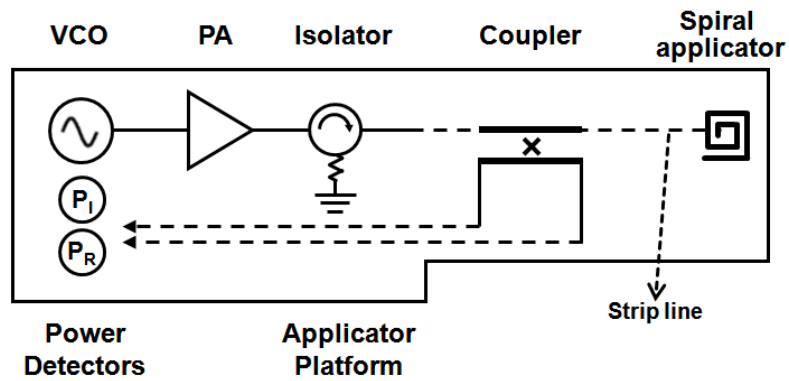


Fig. 4.9 Block diagram of the active integrated applicator system for MNP-assisted hyperthermia.

### 4.4.1　Spiral Applicator

Considering the frequency of operation, the applicator platform is realized using two 254-μm-thick RO4350B substrates. A rectangular spiral inductor is used as a microwave radiator. To enhance the magnetic field around the applicator, the inductor has been designed using a multi-layer structure. Two 1.5-turn inductors with internal area of 1.9 mm × 1.9 mm are implemented on the surface of each substrate, and interconnected through a via hole. Microwave is fed to the applicator through a strip line with 50-ohm impedance. The structure and photograph of the applicator are shown in Fig. 4.10. Its inductance is around 9.5 nH at 2 GHz and provides adequate power matching to the tissue (return loss = 15.6 dB). The simulated and measured return losses of the applicator in contact with pork muscle with and without MNP's are plotted in Fig. 4.11. Better heating performance of the MNP's can be inferred from the simulated SAR distribution as shown in Fig. 4.12.

(a)                                                    (b)
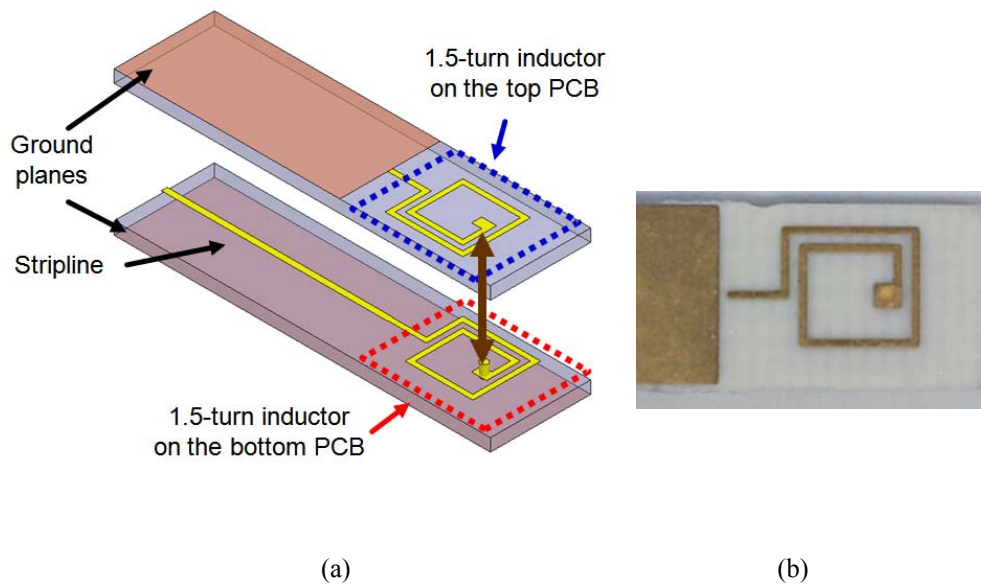
Fig. 4.10 Spiral heat applicator for MNP-assisted hyperthermia: (a) three-dimensional view of the structure and (b) photograph of the applicator.
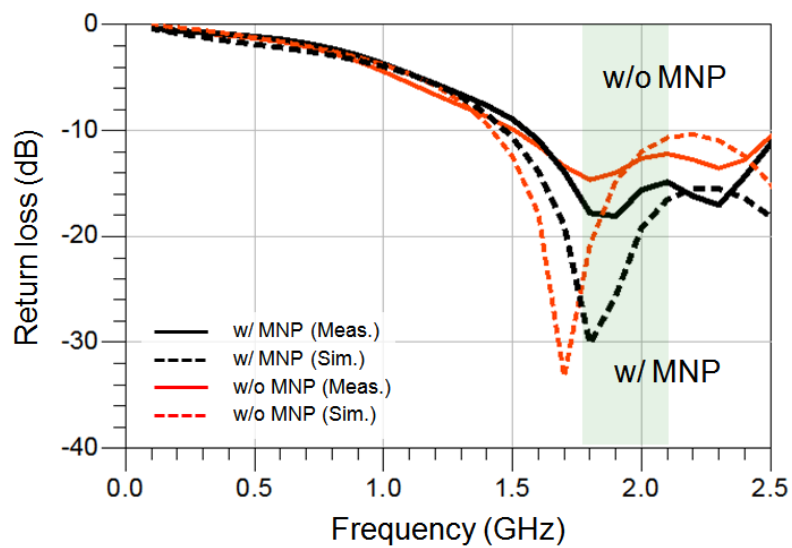


Fig. 4.11 Return loss of the applicator in contact with pork muscle with and without MNP's.
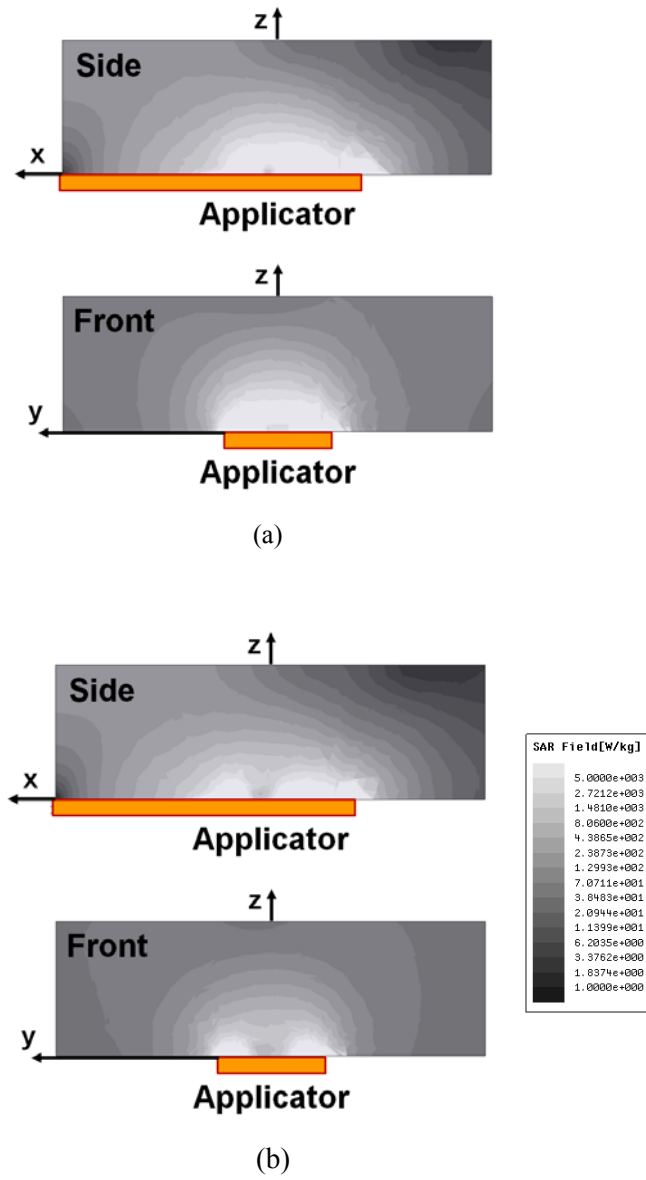
Fig. 4.12 Simulated SAR field distribution in the pork muscle (a) with MNP's and (b) without MNP's.

106

## 4.4.2  Microwave Source

As a microwave source, a VCO has been designed using an NMOS-PMOS cross-coupled structure [76]. The schematic diagram of the VCO is shown in Fig. 4.13. The oscillation frequency is determined by the resonance frequency of the LC tank at the load, which can be controlled by varying the capacitance according to the control voltage. The frequency band can be set by switching the FET switches (SW0, SW1) between on and off, and the frequency is adjusted by the varactor (Cv).

To provide sufficient output power, a two-stage buffer amplifier is employed. The first stage is a common source amplifier with a resistor load (150 $\Omega$), which ensures high voltage gain and isolation between the VCO and PA. The second stage is a class AB push-pull (inverter) amplifier using NMOS and PMOS devices. It offers high output power since both the NMOS and PMOS transistors contribute to the output transconductance. A negative feedback resistor (1 k$\Omega$) is added for unconditional stability of the amplifier and flat output power over a wide bandwidth. Fig. 4.14 shows the schematic diagram of the buffer amplifier.

The VCO has been fabricated using 0.13-µm CMOS process (IBM 8RF-DM). The size of the entire VCO chip is 0.76 mm × 0.6 mm as shown in Fig. 4.15. Figs. 4.16 and 4.17 show the measured characteristics of the VCO. Measured frequency tuning range covers from 1.8 to 3.7 GHz while the output power varies from 4.9 to 6 dBm.
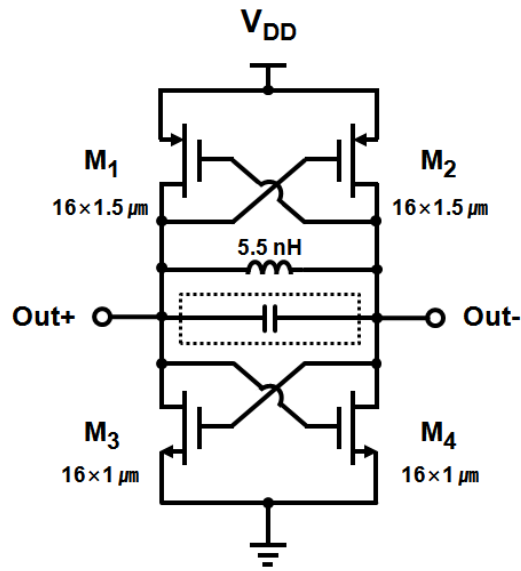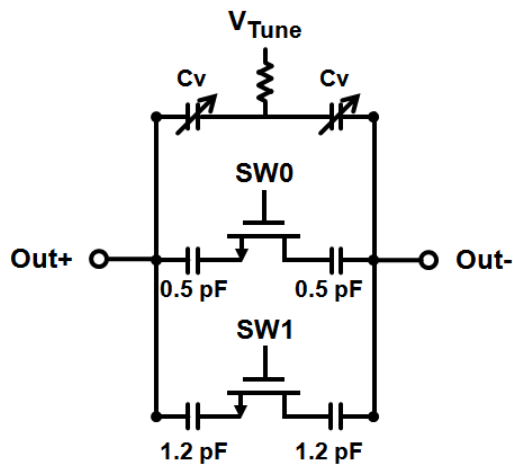
Fig. 4.13 Schematic diagram of the VCO: (a) NMOS-PMOS cross-coupled pair with LC tank and (b) variable capacitor of the LC tank.
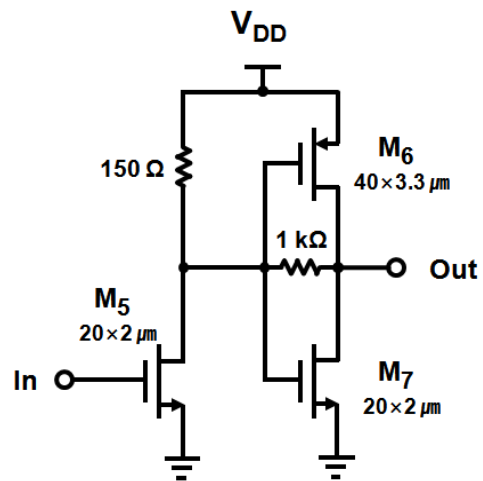
Fig. 4.14 Schematic diagram of the two-stage output buffer amplifier of the VCO.
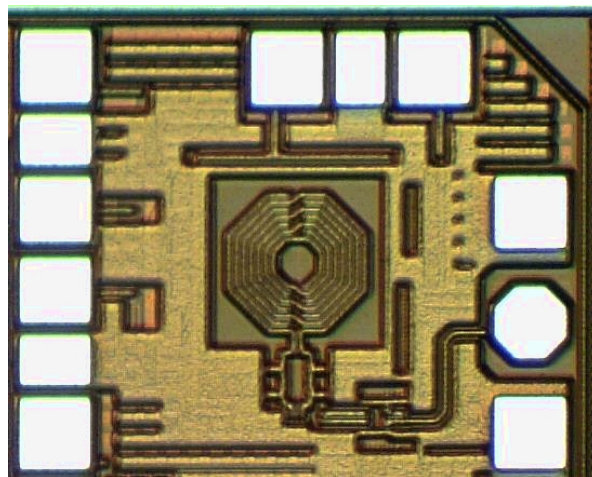


Fig. 4.15 Photograph of the CMOS VCO chip.
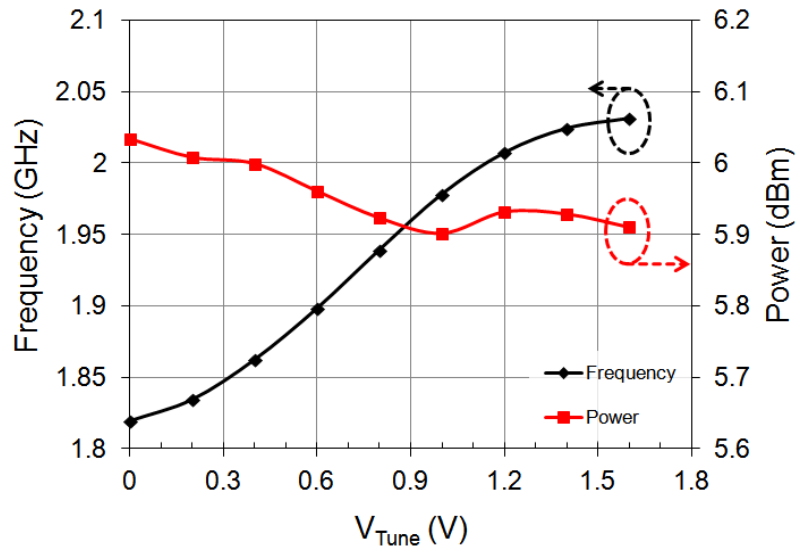
Fig. 4.16 Measured tuning characteristics of the VCO as a function of tuning voltage at SW0=ON, SW1=ON.
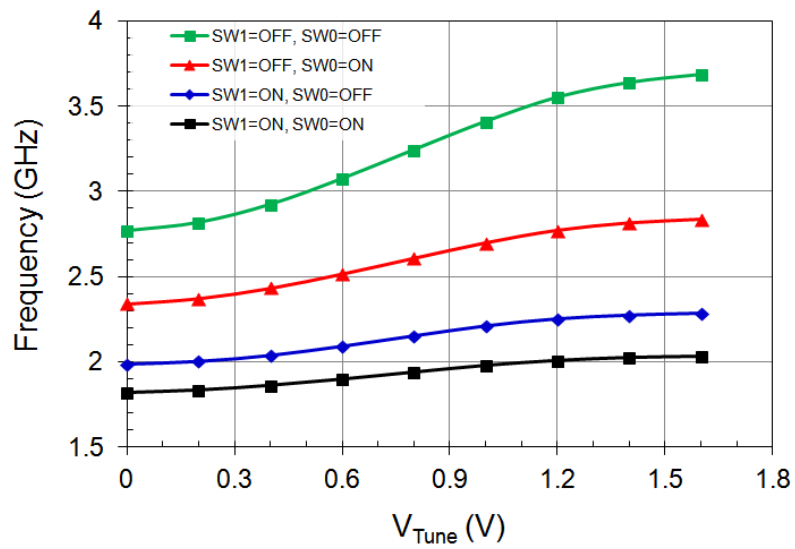


Fig. 4.17 Measured frequency tuning range of the VCO at each state of the switches (SW0, SW1).

The microwave signal from the VCO is amplified by the PA. A quadruple-stacked FET structure has been employed for series power combining to overcome the breakdown voltage limit of CMOS process. The PA has been fabricated in 0.18-μm SOI CMOS, and integrated on a daughter board together with a matching network for ultimate integration. The size of the integrated PA module is 4.5 mm × 5 mm. The PA provides a saturated output power of 32.4 dBm with an associated power gain of 27 dB and 38 % PAE at 2 GHz. At the output of the PA, a commercial isolator (Raditek, RLEI-1930-1990M-5mm-1WR) has been added to prevent the load-pull effects to PA. The insertion loss and isolation of the isolator are better than 0.6 dB and 15 dB, respectively.

### 4.4.3  Power Monitoring Circuits

A dual-channel power detector is integrated on the applicator together with a directional coupler to monitor delivered and reflected power levels. A parallel-summation logarithmic (log) power detector is employed for a wide dynamic range and broad bandwidth [77], [78]. In this subsection, the design of the log detector is described briefly, followed by the directional coupler.

Fig. 4.18 shows the block diagram of the proposed log power detector, which consists of a gain cell, two rectifiers, and a voltage summer. An input signal $V_{in}$ is distributed to two branches in parallel and amplified to different power levels. The

111

subsequent rectifiers generate piecewise linear-in-dB voltages, $V_{DC1}$, $V_{DC2}$, at different input power ranges, which are summed to obtain an approximate log response. To achieve an ideal log response by combining two piecewise linear-in-dB outputs of the rectifiers, the voltage gain ratio between adjacent paths, $A_{V1}/A_{V2}$ should be set equal to the dynamic range of each rectifier.
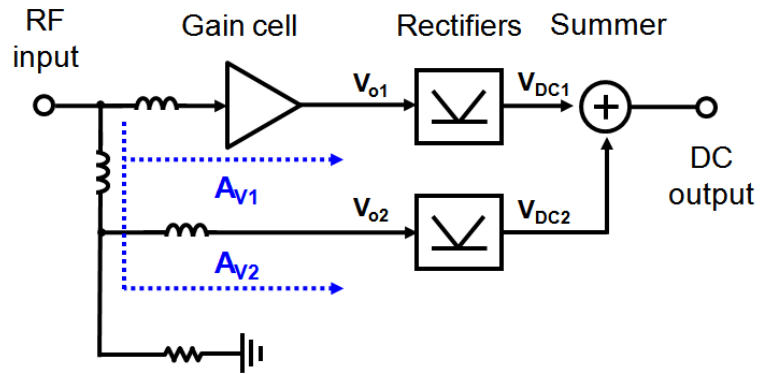


Fig. 4.18 Block diagram of the proposed log power detector.

In order to achieve high dynamic range with small log errors, the rectifier at the end of each branch is designed with a source-degenerated common-source configuration as shown in Fig. 4.19. The common-source transistor ($M_1$) biased in class B performs half-wave rectification in combination with the subsequent RC low pass filter. Since the drain current of $M_1$ ($I_d$) flows only during the positive swing of its gate voltage ($V_g$), the drain voltage ($V_d$) decreases as the input power ($P_{in}$) increases. Without the source degeneration, a relationship between $V_g$ and $V_d$ at the positive peak of the gate voltage can be expressed as follows:

$$V_g = V_{th} + \sqrt{\frac{2(V_{DD}-V_d)}{R_d\, \mu_n C_{ox}(W/L)_1}} + V_s \qquad (4.17)$$

where $\mu_n$, $C_{ox}$, and $V_{th}$ are the electron mobility, gate-oxide capacitance per unit area, and threshold voltage, respectively, while $(W/L)_1$ is the aspect ratio of $M_1$ and $V_S$ is the source voltage of $M_1$. In order to achieve a linear-in-dB characteristic over a wide dynamic range, the slope of $V_d$ vs $V_g$ has to be reduced. For this purpose, negative feedback is provided by $M_S$, which functions as active source degeneration. As the input power rises, $V_d$ gets lower, which increases the drain-source resistance of $M_S$ and thus the source degeneration resistance ($R_{SD}$). Increased resistance in source degeneration results in the reduced drain current of $M_1$ and partially restores

$V_d$ drop. As a result, the rate of $V_d$ reduction with respect to the input power can be reduced. In the presence of the active degeneration, equation (4.17) can be rewritten as

$$V_g = V_{th} + \sqrt{\frac{2\,(V_{DD}-V_d)}{R_d\,\mu_n\,C_{ox}\,(W/L)_1} + \frac{(V_{DD}-V_d)/R_d}{1/R_s + 1/R_{ds}}}. \qquad (4.18)$$

The denominator of the last term in equation (4.18) represents the negative feedback due to the source degeneration.

The gain cell in the first branches (see Fig. 4.18) is implemented using a two-stage cascaded common-source amplifier, which employs a peaking inductor and a parallel feedback loop to cover a wide frequency range up to 16 GHz. The voltage gain $A_{V1}$ is determined to be 13 dB considering the dynamic range of the rectifier. To avoid DC offset errors, AC coupling capacitors are used between the stages. The input matching bandwidth of the overall power detector is extended by adding series inductors between the branches, which helps absorb the input capacitance of each branch and extends the operation bandwidth, as in the case of the traveling wave amplifier.

The DC output voltages ($V_{DC1}$, $V_{DC2}$) of the rectifiers are summed using the summer circuit shown in Fig. 4.20. A common drain resistor, $R_3$ (500 Ω), converts

the sum of the currents from each branch to the output voltage, $V_{out}$. Source degeneration ($R_1$, $R_2$) is employed at each output transistor ($M_1$, $M_2$) to reduce output distortion caused by excessive current hogging of a particular branch.
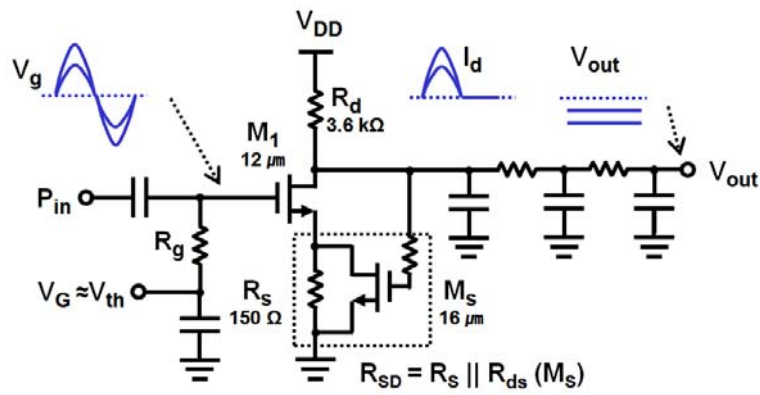


Fig. 4.19 Schematic diagram of the rectifier.
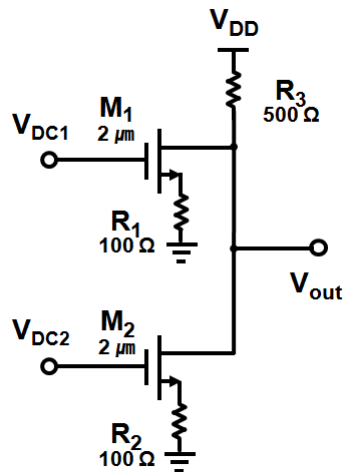


Fig. 4.20 Circuit schematic of the voltage summer.

The proposed power detector has been designed and fabricated using 0.13-μm CMOS process (IBM 8RF-DM). The fabricated dual-channel power detector has a die size of 1.0 mm × 0.96 mm including the probe pads as shown in Fig. 4.21. It operates with a DC power supply of 2 V and the current consumption of each detector is 8 mA. For power detection measurement, the continuous-wave (CW) input signal is injected using an analog signal generator (Agilent E8257D) and the output DC voltage is measured using a digital multimeter (Agilent 34401A).

Fig. 4.22 illustrates the measured DC output voltage versus the input power. The measured dynamic range is larger than 27 dB from 1 to 16 GHz with the log error less than ±1 dB. The minimum log slope is 38 mV/dB at 16 GHz. The log errors referenced to the lines of best-fit are shown in Fig. 4.23. The return loss of the log detector is better than 10 dB up to 20 GHz.
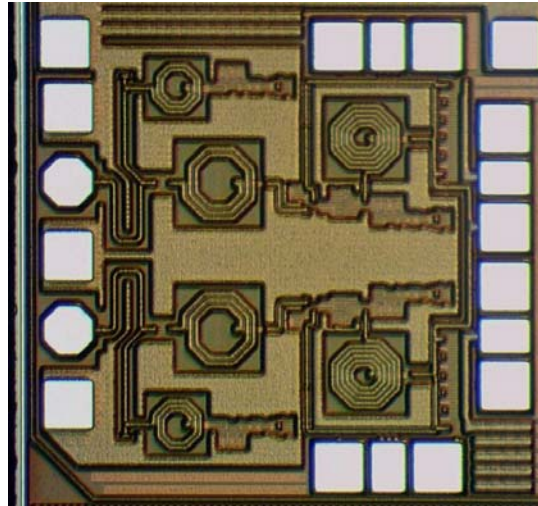


Fig. 4.21 Photograph of the power detector with a die size of 1.0 mm × 0.96 mm.
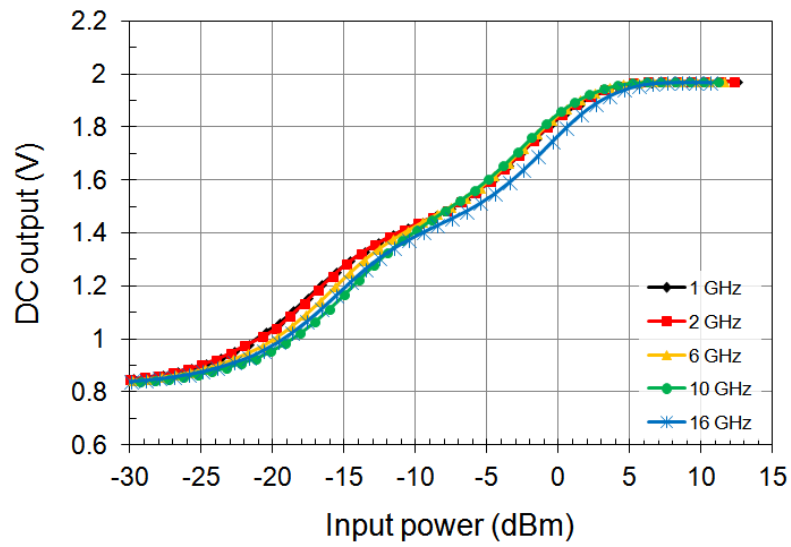
Fig. 4.22 Measured log responses of the power detector at 1-16 GHz.
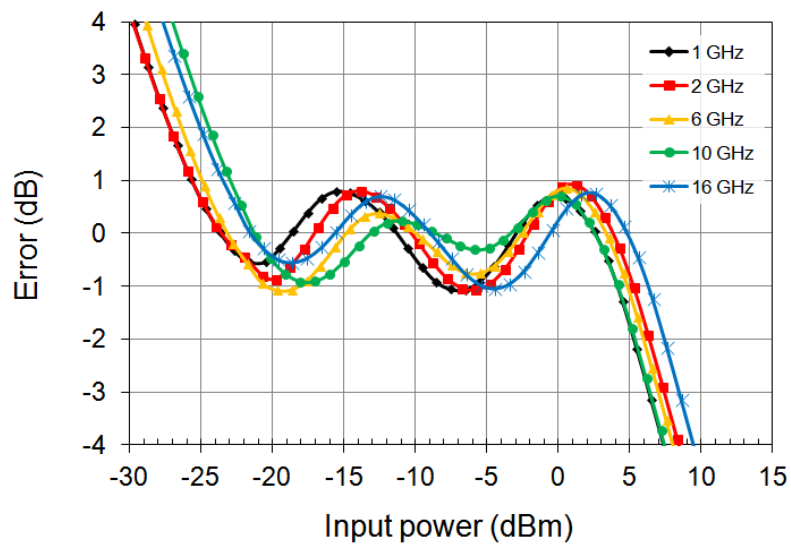


Fig. 4.23 Measured log errors between the output voltage and the linear-in-dB best-fit curve at 1-16 GHz.

A coupled line coupler is built into the strip line of the applicator. Since a strip line supports pure transverse electromagnetic mode (TEM) propagation and thus has same phase velocities for even- and odd-modes, a coupled line coupler in a strip line provides better isolation than a microstrip coupled line coupler. The coupling is determined as around 30 dB at 2 GHz considering the dynamic range of the power detector and output power of the PA. Fig. 4.24 shows the measured S-parameters of the coupler up to 4 GHz. The measured coupling is 28.1 dB at 2 GHz. The return loss and isolation are 22 dB and 49.9 dB, respectively.
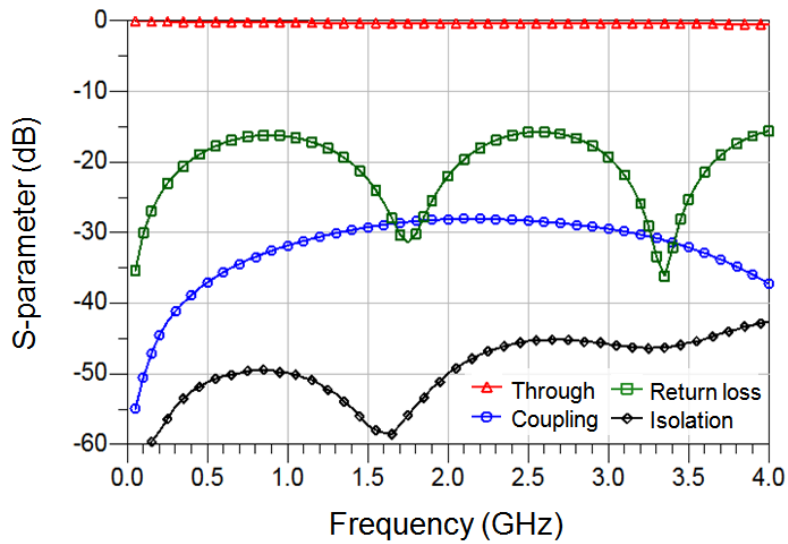


Fig. 4.24 Measured S-parameters of the strip line coupler.

### 4.4.4 Active Integrated Applicator for MNP-Assisted Hyperthermia

The integrated applicator system is implemented by integrating all of the aforementioned circuits with the heat applicator. The performances of the individual circuit components are summarized in Table 4.2. To facilitate the evaluation of the system, the circuits are integrated on a separate daughter board, which is vertically integrated with the applicator. This multi-board configuration has another advantage of flexible routing of signal lines between the IC and applicator. The configuration of the applicator and circuit daughter board is illustrated in Fig. 4.25. The output signal from the PA is transferred to the applicator through via holes and strip line. The coupled signals are routed in the strip line layer to the power detectors on the circuit daughter board. Fig. 4.26 shows the photographs of the fabricated applicator board, circuit board, and the integrated applicator system. The sizes of the applicator and circuit board are 65.8 mm × 4 mm and 26.3 mm × 6 mm, respectively. The chip interconnects have been realized using the wire bonds.

TABLE 4.2

PERFORMANCES OF THE CIRCUIT COMPONENTS FOR THE ACTIVE INTEGRATED

HEAT APPLICATOR FOR MNP-ASSISTED HYPERTHERMIA

| Circuit | Topology | Technology | Performances |
|---------|----------|------------|--------------|
| Applicator | Spiral | PCB | BW: 1.8-2.6 GHz<br>(Return loss > 10 dB) |
| VCO | Cross-coupled with a capacitor bank | 0.13-μm CMOS | BW: 1.8-3.7 GHz<br>$P_{out}$ > 4.9 dBm |
| Power amplifier | Stacked-FET | SOI CMOS | BW: 1.9-2.1 GHz<br>$P_{sat}$ > 32.4 dBm (@ 2 GHz) |
| Power detector | Parallel-summation log detector | 0.13-μm CMOS | BW: 1-16 GHz<br>DR > 27 dB<br>Log slope > 38 mV/dB |
| Coupler | Coupled line | PCB | Coupling: 28.1 dB (@ 2 GHz)<br>Isolation > 49.9 dB |

BW: Bandwidth, DR: Dynamic range,
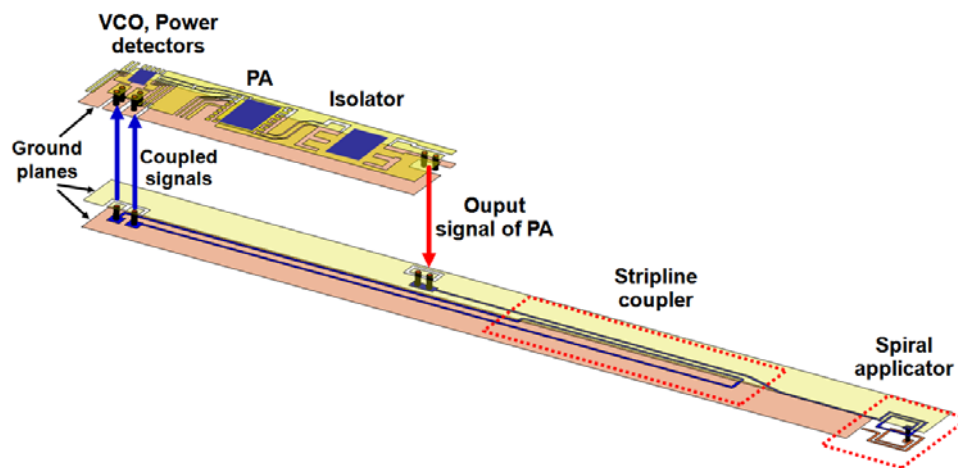
Fig. 4.25 Multi-board configuration of the circuit daughter board and applicator.



(a)
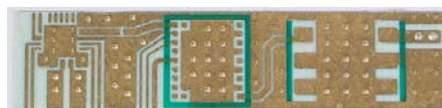


(b)



(c)

Fig. 4.26 Photographs of (a) the applicator, (b) circuit board, and (c) fabricated entire integrated applicator system for MNP-assisted hyperthermia.

## 4.5 Experiment Results

To evaluate the performance of the proposed integrated applicator system, heating experiments were performed using the experimental setup shown in Fig. 4.27. For the experiments, two types of samples were used. Agar phantoms having dielectric properties similar to human breast cancer were constructed and experimented upon since one can easily prepare tissue samples with homogeneous and uniform electromagnetic and thermal properties. Also, we performed microwave hyperthermia on pork muscle.
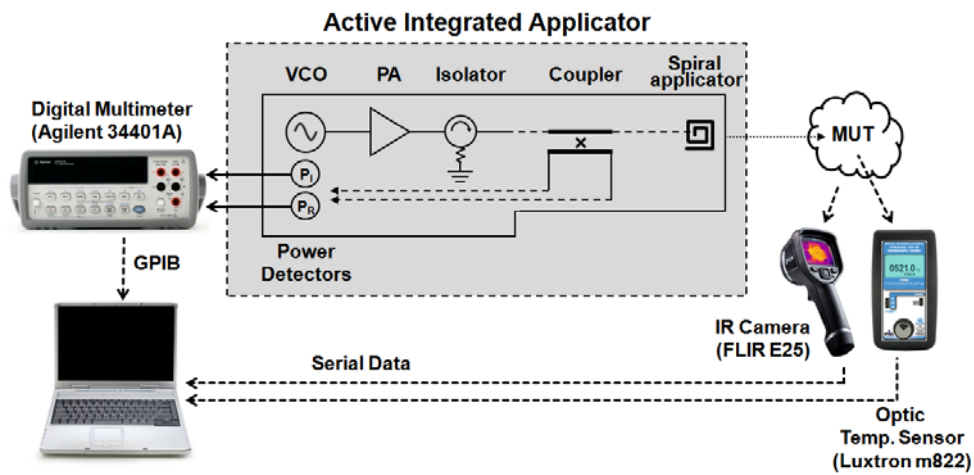


Fig. 4.27 Experimental setup for MNP-assisted microwave hyperthermia.

The cancer-equivalent phantoms were made of Agar (Becton Dickinson and Company), TX-151 (Oil Center Research), sodium chloride, polyethylene powder (Sigma-Aldrich), and deionized water. Agar is used to maintain the shape of the phantom, and TX-151 is for stickiness of the phantom. The dielectric properties of the phantom are controlled by the content of sodium chloride, polyethylene powder, and water. The detailed ingredients and procedure are shown in Fig. 4.28. For the sample with MNP's, the magnetite nanoparticles were mixed with the mixture before filling into the mold, whose concentration in the phantom is approximately 5 mg/mL. The permittivity of the constructed phantom shows good agreement with that of human breast cancer up to 8 GHz as shown in Fig. 4.29.
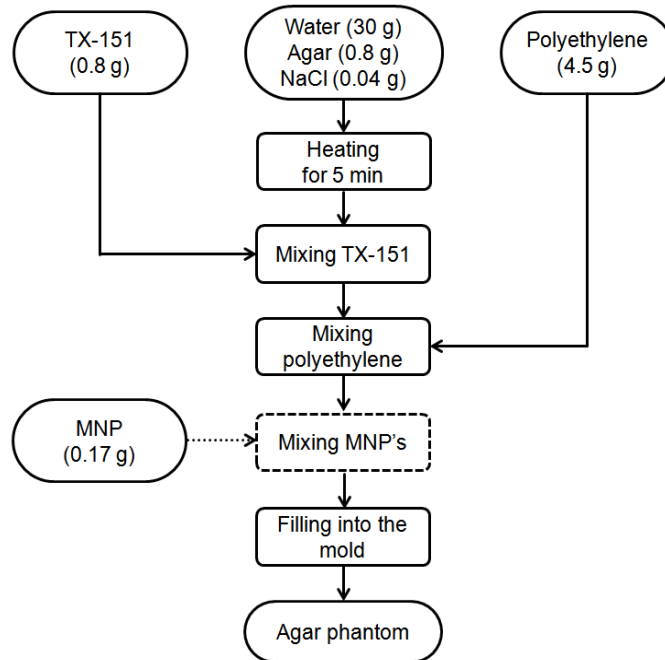
Fig. 4.28 Preparation procedure of agar phantom.
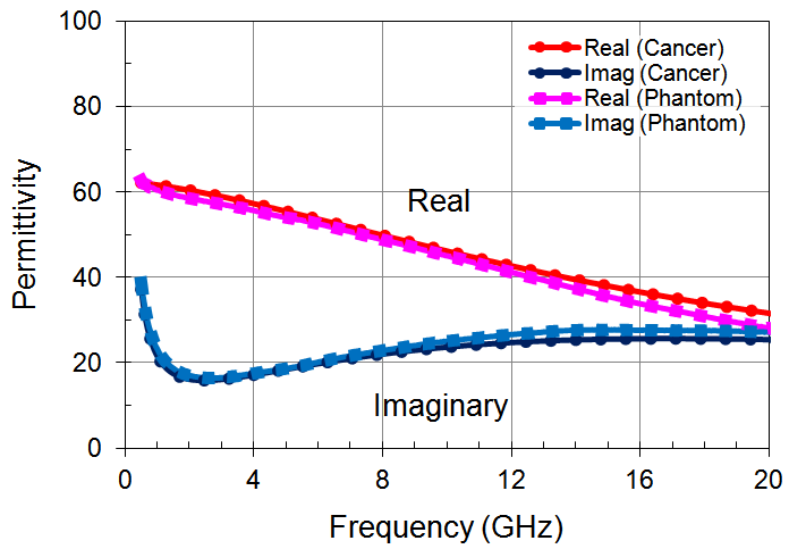


Fig. 4.29 Measured complex permittivity of constructed phantom and human breast cancer.

To see the effect of MNP's for hyperthermia, heating experiments were performed on 10-mm-thick phantoms for 5 minutes. The power delivered to the applicator was around 0.63 W, which corresponds to 1.57 W/cm$^2$. During the heating, the temperature profiles at 5 mm away from the surface of the applicator were measured using an optic temperature sensor (Luxtron, m822), and compared with simulation results. The measured 5-mm temperatures of the phantoms with and without MNP's are plotted in Fig. 4.30. After 5 min of heating, the temperature of the sample with MNP's was increased from 24.0 to 46.6 °C, a temperature high enough for hyperthermia. On the other hand, the sample without MNP's showed the peak temperature of only 40.9 °C. This result clearly demonstrates the feasibility of cancer-specific treatment using MNP's. The measured results show good agreement with the simulated prediction, which validates the coupled electromagnetic-thermal analysis presented in section 4.3. Fig. 4.31 shows the return losses of the phantoms with and without MNP's. Although the simulated return loss is slightly different from the measured one due to the simplified electromagnetic analysis, they show similar trends. The return loss of the sample with MNP's is better than without MNP's, and the return loss increases as the temperature of the tissue rises.
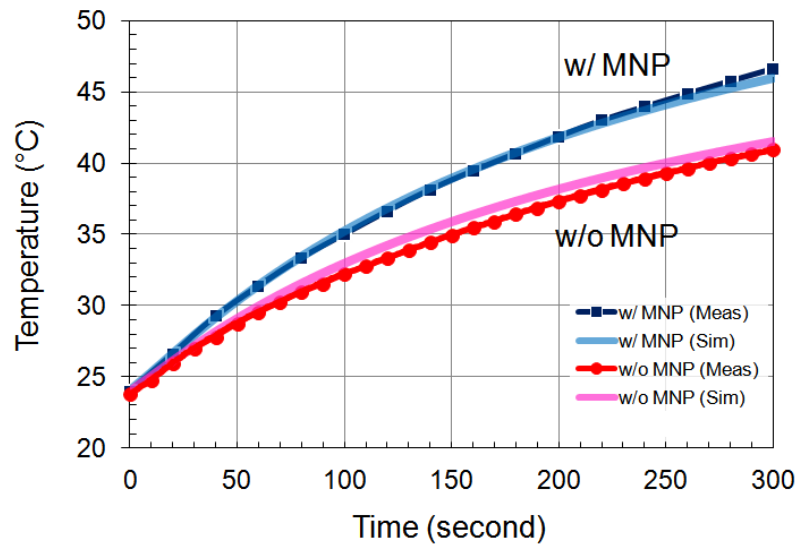
Fig. 4.30 Simulated and measured 5-mm temperatures of the phantoms with and without MNP's.
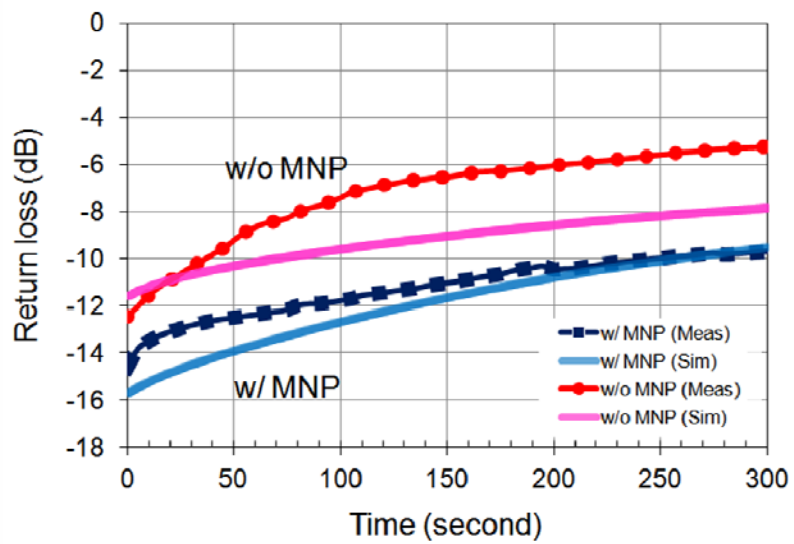


Fig. 4.31 Simulated and measured return losses of the phantoms with and without MNP's.

126

Heating experiments on pork muscle with and without MNP's were also performed using the fabricated integrated heat applicator. Pork muscle was used in this experiment due to the similar dielectric properties between pork muscle and human breast cancer. For the sample with MNP's, 20-µL aqueous solution of $Fe_3O_4$ nanoparticles (5 mg/mL) was applied and smeared into the specimen. The surface temperature of 10-mm-thick muscle was measured using an IR camera for 5 minutes as shown in Fig. 4.32. The measured surface temperatures during 5-min heating are plotted in Fig. 4.33. After 5-min heating with a power of 1 W, the temperature of the muscle with MNP's increased from 22.7 to 49.2 °C while the sample without MNP's showed the temperature rise only up to 39.5 °C. Considering the temperature threshold of 43 °C for effective hyperthermia [9], the proposed method can treat cancerous tissues targeted with MNP's while leaving no damage to the normal tissues. Table 4.3 compares the reported RF and microwave hyperthermia using $Fe_3O_4$ MNP's.
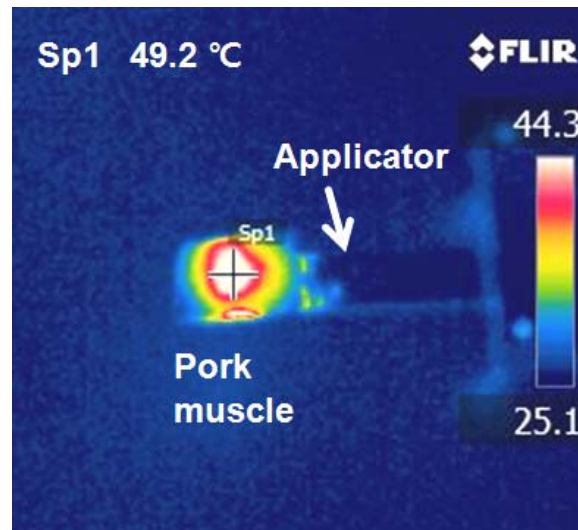
Fig. 4.32 IR image of the pork muscle with MNP's after 5-min heating using the integrated applicator.
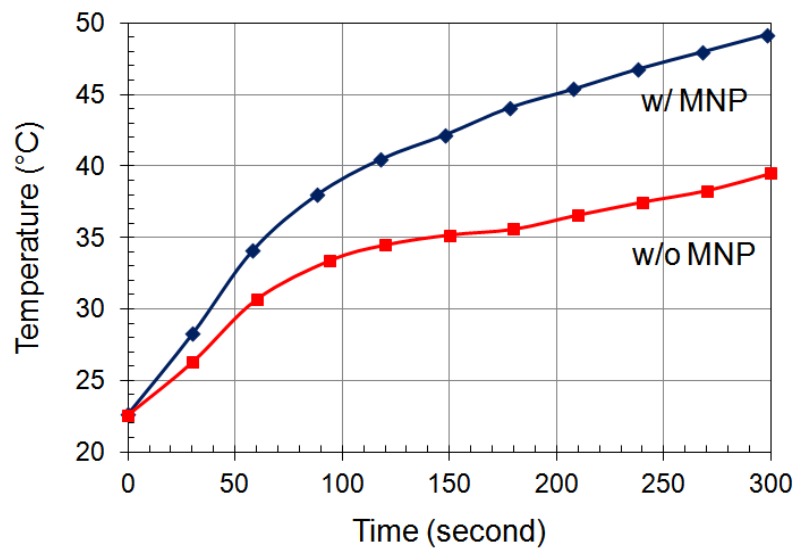


Fig. 4.33 Time evolution of surface temperatures of pork muscle with and without MNP's for 5 minutes.

TABLE 4.3

COMPARISON OF REPORTED RESULTS OF RF AND MICROWAVE HYPERTHERMIA

USING MNP'S

| | [79] | [80] | [81] | This work |
|---|---|---|---|---|
| Applicator | Solenoid coil * | Waveguide * | Coaxial antenna ** | Integrated applicator ** |
| MNP size (Concentration) | 23.8 nm (1.9 mg/mL) | 15 nm (13.3 mg/mL) | 15 nm (13.2 mg/mL) | 63 nm (5 mg/mL) |
| Sample | *In-vivo* tumor (mouse) | Phantom | Phantom | Phantom / pork muscle |
| Signal | 980 kHz, 10 kW | 224 MHz, 66 W | 2.45 GHz, 10 W | 2 GHz 0.63 W / 1 W |
| Time | 5 min | 16 min | 5 min | 5 min |
| ΔT (°C) | 36 | 11.1 | 56.6 | 22.6 / 26.5 |

*: non-invasive, **: minimally invasive.

The frequency dependence of MNP-assisted hyperthermia was investigated by measuring the temperature rises of 10-mm-thick phantoms with and without MNP's at various frequencies from 1.6 to 2.4 GHz. As a microwave source, a signal generator (Agilent E4437B) was used together with a broadband power amplifier (WanTcom WBPA0527A). The microwave power delivered to the applicator was set to 0.63 W for both phantoms with and without MNP's for fair comparison. The temperature profile was monitored for 5 minutes at 5 mm away from the surface of the applicator using an optic temperature sensor (Luxtron, m822). Fig. 4.34 shows measured 5-mm temperatures of the phantoms with and without MNP's after 5-min heating from 1.6 to 2.4 GHz. Each data point in the plot is averaged over four phantom samples and the error bar indicates the standard error in the measurement. The measured ratio of temperature rises between the phantoms with and without MNP's is compared with the simulated one in Fig. 4.35. The measured results show similar trend as those of simulations. The peak value is around 1.11 at 2 GHz, which is consistent with the optimum frequency for MNP-assisted hyperthermia calculated by the coupled electromagnetic-thermal analysis in section 4.3.
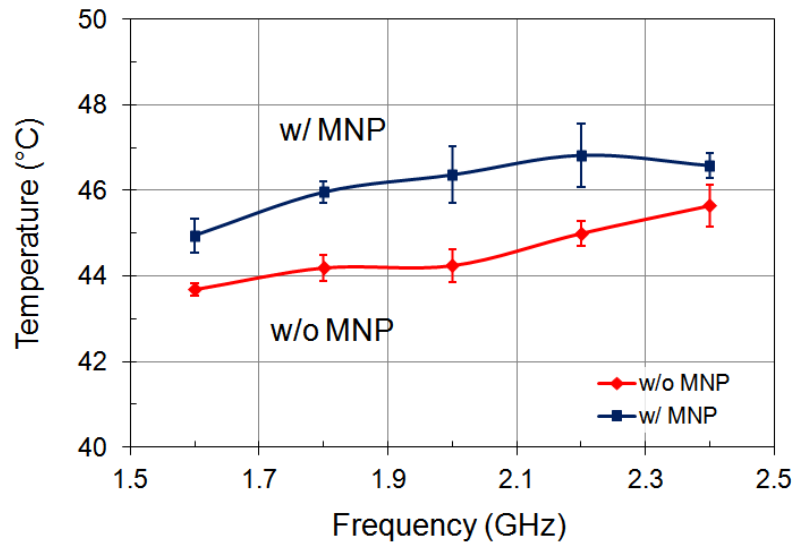
Fig. 4.34 Measured 5-mm temperatures of the phantoms with and without MNP's after 5-min heating from 1.6 to 2.4 GHz.
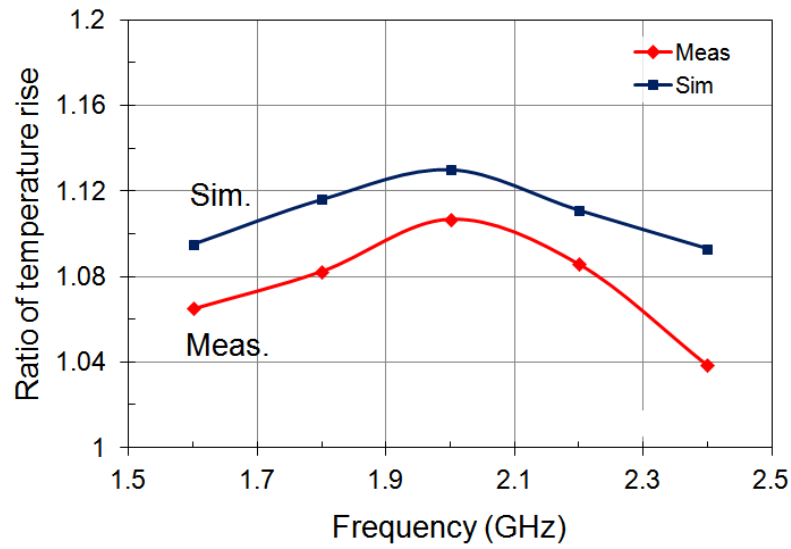


Fig. 4.35 Simulated and measured ratio of temperature rises between the phantoms with and without MNP's after 5-min heating from 1.6 to 2.4 GHz.

131

## 4.6　　Summary

In this work, we have investigated microwave hyperthermia using MNP's to enhance the heating efficiency and material sensitivity. By conducting a coupled electromagnetic-thermal analysis based on a one-dimensional layered tissue model, the solution of the bio-heat transfer equation is derived, from which the temperature rise of the tissue during hyperthermia can be accurately estimated. Also, the optimum frequency for microwave hyperthermia has been determined to be 2 GHz by comparing temperature rises of the tissues with and without MNP's at various frequencies from 1.6 to 3 GHz.

In order to demonstrate the feasibility of microwave hyperthermia using MNP's, we have developed an active integrated heat applicator system. A microwave source consisting a VCO and a PA has been implemented in MMIC's and integrated on a spiral applicator platform. A dual-channel log power detector is employed to monitor the delivered and reflected power levels together with a directional coupler built into the strip line of the applicator. The entire active module has been realized in a small form factor of 26.3 mm × 6 mm, which is integrated on the applicator platform with a size of 65.8 mm × 4 mm.

The effect of MNP's on microwave hyperthermia has been evaluated by heating experiments on agar phantoms and pork muscles. After 5-min of heating, the temperature of the phantom with MNP's was increased from 24.0 to 46.6 °C,

whereas that of the phantom without MNP's rose only up to 40.9 °C. In the experiments on pork muscle, the sample with MNP's showed a high peak temperature of 49.2 °C after 5 minutes into microwave application compared to 39.5 °C of that without MNP's. The heating experiments using microwaves from 1.6 to 2.4 GHz confirmed the validity of the coupled electromagnetic-thermal analysis. These results verified the effectiveness of MNP's for enhanced heating efficiency and material selectivity in hyperthermia. The heating performance of the integrated heat applicator has been also validated, showing that effective heating could be accomplished at low power levels less than 1 W. Combined with cancer cell targeting, MNP-assisted microwave hyperthermia would offer a promising method for high-efficiency and cancer-specific treatment with low collateral damage to healthy tissue.

# Chapter 5

# Conclusion

In this thesis, miniaturized microwave active integrated probe and applicator systems applicable to cancer detection and treatment are presented. In detail, active integrated probe for complex permittivity measurement is proposed and developed by integrating a multi-state reflectometer (MSR) on the probe platform. Two active integrated heat applicators for cancer ablation are also demonstrated. One is for low-power hyperthermia at *Ku*-band. The other is for magnetic nanoparticle (MNP)-assisted hyperthermia at 2 GHz.

For cancer detection application, a complex permittivity measurement technique using an integrated MSR is proposed. The MSR has been designed to cover both 2 and 16 GHz bands, which are most effective frequency bands to represent broadband dielectric properties of cancer cells. The MSR consists of a

dual-band phase-locked loop (PLL), a power amplifier, a directional coupler, an impedance tuner, and two RF power detectors. All the active circuits have been implemented in monolithic microwave integrated circuits (MMIC's), and integrated together with the coupler on a micromachined silicon planar probe with an open-ended coaxial aperture. For dual-band operation, the circuit components have been designed with multi-octave broadband characteristics. The performance of the fabricated integrated probe has been verified by comparing the measured permittivities of 0.9% saline, pork muscle, fat, and xenografted human breast cancer with the reference data. This is the first demonstration of a miniaturized active integrated probe for complex permittivity measurement of biological material.

A *Ku*-band active integrated heat applicator is developed for low-power microwave hyperthermia. The heat applicator has been fabricated using Microelectromechanical Systems (MEMS) technology for miniaturization and integration with the active circuits. A *Ku*-band source module consisting of a voltage controlled oscillator (VCO), a driver amplifier, and a power amplifier (PA) has been implemented in MMIC's and integrated on the applicator platform together with a directional coupler and power detectors for power monitoring. The fully integrated heat applicator has been realized in a small form factor of 8 mm × 56 mm × 0.6 mm. *In-vitro* and *in-vivo* ablation experiments have been performed on pork muscle/fat and human-cancer xenografted nude mouse, respectively. Temperature rise to over

135

46 °C has been achieved using only 1.2 W of on-board source power.

An active integrated heat applicator for MNP-assisted hyperthermia is demonstrated for enhanced heating efficiency and material selectivity in microwave hyperthermia. MNP is employed to improve microwave power absorption in cancer cells. A coupled electromagnetic-thermal analysis is performed to investigate the effect of the MNP on hyperthermia, from which the optimum frequency for hyperthermia is found to be around 2 GHz. A microwave source consisting of a VCO and a PA has been implemented in MMIC's and integrated on the spiral applicator platform. A dual-channel log power detector has been employed to monitor the power levels together with a directional coupler. Experiment results show not only sufficient heating performance of the integrated applicator, but also the effectiveness of MNP for low-power and cancer-specific microwave hyperthermia.

The microwave method has several advantages, not only in terms of high-resolution, accuracy, and material-selectivity, but also in the overall system size, cost, and complexity. The active integrated systems presented in this work demonstrate the feasibility of the microwave method for clinical application. By offering the advantages, the concept of microwave active integrated systems can emerge as a substitute or an auxiliary to the conventional diagnostic and therapeutic methods.

# Bibliography

[1] J. Cho, J. Yoon, S. Cho, K. Kwon, S. Lim, D. Kim, E. Lee, C. Kim, J. Choi, C. Cheon, and Y. Kwon, "*In-vivo* measurements of the dielectric properties of breast carcinoma xenografted on nude mice," *Int. J. Cancer*, vol. 119, no. 3, pp. 593–598, Aug. 2006.

[2] A. Rosen and F. Sterzer, "Applications of Microwave Heating in Medicine," in *IEEE MTT-S Int. Microw. Symp. Digest*, May 1994, pp. 1615-1618.

[3] A. J. Surowiec, S. S. Stuchly, J. R. Barr, and A. S. Warup, "Dielectric properties of breast carcinoma and the surrounding tissues," *IEEE Trans. Biomed. Eng.*, vol. 35, no. 4, pp. 257–263, Apr. 1988.

[4] W. T. Joines, Y. Zhang, C. Li, and R. L. Jirtle, "The measured electrical properties of normal and malignant human tissues from 50 to 900 MHz," *Med. Phys.*, vol. 21, pp. 547–550, 1994.

[5] J.-W. Choi, J. Cho, Y. Lee, J. Yim, B. Kang, K. Oh, W. H. Jung, H. J. Kim,

C. Cheon, H.-D. Lee, and Y. Kwon, "Microwave detection of metastasized breast cancer cells in the lymph node: Potential application for sentinel lymphadenectomy," *Breast Cancer Res. Treatment*, vol.86, pp. 107–115, 2004.

[6] J. Yoon, J. Cho, N. Kim, D.-D. Kim, E. Lee, C. Cheon, and Y. Kwon, "High-frequency microwave ablation method for enhanced cancer treatment with minimized collateral damage," *Int. J. Cancer*, vol. 129, pp. 1970-1978, Oct. 2011.

[7] P. M. Meaney, K. D. Paulsen, and J. T. Chang, "Near-Field Microwave Imaging of Biologically-Based Materials Using a Monopole Transceiver System," *IEEE Trans. Microwave Theory Tech.*, vol. 46, no. 1, pp. 31-45, Jan. 1998.

[8] P. M. Meaney, M. W. Fanning, D. Li, S. P. Poplack, and K. D. Paulsen, "A Clinical Prototype for Active Microwave Imaging of the Breast," *IEEE Trans. Microwave Theory Tech.*, vol. 48, no. 11, pp. 1841-1853, Nov. 2000.

[9] D. E. Thrall, G. L. Rosner, C. Azuma, S. M. Larue, B. C. Case, T. Samulski, and M. W. Dewhirst, "Using units of CEM 43°C $T_{90}$, local hyperthermia thermal dose can be delivered as prescribed," *Int. J. Hyperthermia*, vol. 16, no. 5, pp. 415-428, Sep. 2000.

[10] K. Saito, H. Yoshimura, K. Ito, Y. Aoyagi, and H. Horita, "Clinical trials of interstitial microwave hyperthermia by use of coaxial-slot antenna with two slots," *IEEE Trans. Microwave Theory Tech.*, vol. 52, no. 8, pp. 1987-1991, Aug. 2004.

[11] M. Hiraoka, M. Mitsumori, N. Hiroi, S. Ohno, Y. Tanaka, Y. Kotsuka, and K. Sugimachi, "Development of RF and Microwave Heating Equipment and Clinical Applications to Cancer Treatment in Japan," *IEEE Trans. Microwave Theory Tech.*, vol. 48, no. 11, pp. 1789-1799, Nov. 2000.

[12] W. Hürter, F. Reinbold, and W. J. Lorenz, "A Dipole Antenna for Interstitial Microwave Hyperthermia," *IEEE Trans. Microwave Theory Tech.*, vol. 39, no. 6, pp. 1048-1054, Jun. 1991.

[13] M. F. Iskander and A. M. Tumeh, "Design Optimization of Interstitial Antennas," *IEEE Trans. Biomed. Eng.*, vol. 36, no. 2, pp. 238-246, Feb. 1989.

[14] D. Kim, K. Kim, J. Oh, J. Cho, C. Cheon, and Y. Kwon, "A *K*-Band Planar Active Integrated Bi-Directional Switching Heat Applicator With Uniform Heating Profile," *IEEE Trans. Microw. Theory Tech.*, vol. 57, no. 10, pp. 2581-2587, Oct. 2009.

[15] J. A. Pearce, J. R. Cool, and S. Y. Emelianov, "Ferrimagnetic Nanoparticles

Enhance Microwave Heating for Tumor Hyperthermia Therapy," in *2010 IEEE EMBS Conference Proc*. Oct. 2011, pp. 2751-2754.

[16] S. C. Hagness, A. Taflove, and J. E. Bridge, "Two-dimensional FDTD analysis of a pulsed microwave confocal system for breast cancer detection: Fixed-focus and antenna-array sensors," *IEEE Trans. Biomed. Eng.*, vol. 45, no. 12, pp. 1470–1479, Dec. 1998.

[17] D. N. Krag, D. L.Weaver, J. C. Alex, and J. T. Fairbank, "Surgical resection and radio localization of the sentinel lymph node in breast cancer using a gamma probe," *Surg. Oncol.*, vol. 2, pp. 335–339, 1993.

[18] G. F. Engen, "The Six-Port Reflectometer: An Alternative Network Analyzer," *IEEE Trans. Microw. Theory Tech.*, vol. 25, no. 12, pp. 1075-1080, Dec. 1977.

[19] L. C. Oldfield, J. P. Ide, and E. J. Griffin, "A multistate reflectometer," *IEEE Trans. Instrum. Meas.*, vol. IM-34, pp. 198-201, Jun. 1985.

[20] F. M. Ghannouchi and R. G. Bosisio, "Measurement of Microwave Permittivity Using Six-Port Reflectometer with an Open-Ended Coaxial Line," *IEEE Trans. Instrum. Meas.*, vol. 38, no. 2, pp. 505-508, Apr. 1989.

[21] J. Muñoz, M. Rojo, and J. Margineda, "A Method for Measuring the Permittivity without Ambiguity Using Six-Port Reflectometer," *IEEE Trans.*

*Instrum. Meas.*, vol. 42, no. 2, pp. 222-226, Apr. 1993.

[22] A. L. de Souza Rolim, A. J. Belfort de Oliveira, and M. T. de Melo, "Six-port Complex Permittivity Measurements," in *Proc. 36th European Microwave Conference*, Manchester, UK, 2006, pp. 492-494.

[23] M. K. Choi, M. Zhao, S. C. Hagness, and D. W. van der Weide, "Compact Mixer-Based 1–12 GHz Reflectometer," *IEEE Microw. Wireless Compon. Lett.*, vol. 15, no. 11, pp. 781–783, Nov. 2005.

[24] G. Madonna, A. Ferrero, and M. Pirola, "Design of a Broadband Multiprobe Reflectometer," *IEEE Trans. Instrum. Meas.*, vol. 48, no. 2, pp. 622 –625, Apr. 1999.

[25] C. L. Pournaropoulous, and D. K. Misra, "The coaxial aperture electromagnetic sensor and its application in material characterization," *Meas. Sci. Technol.*, vol. 8, no. 11, pp. 1191-1202, Nov. 1997.

[26] F. Duhamel, I. Huynen, A.V. Vorst, "Measurements of Complex Permittivity of Biological and Organic Liquids up to 110 GHz," in *IEEE MTT-S Int. Microw. Symp. Digest*, 1997, pp. 107-110.

[27] B. Kang, J. Park, J. Cho, K. Kwon, S. Lim, J. Yoon, C. Cheon, Y. Kim, and Y. Kwon, "Novel Low-Cost Planar Probes With Broadside Apertures for Nondestructive Dielectric Measurement of Biological Materials at

Microwave Frequencies," *IEEE Trans. Microwave Theory Tech.*, vol. 53, no. 1, pp.134-143, Jan. 2005.

[28] N. Kim, J. Yoon, S. Cho, J. Cho, C. Cheon, and Y. Kwon, "An Optimum Design Methodology for Planar-Type Coaxial Probes Applicable to Broad Temperature Permittivity Measurements," *IEEE Trans. Microw. Theory Tech.*, vol. 56, no. 3, pp. 684-692, Mar. 2008.

[29] J. Kim, S. Cho, N. Kim, J. Yoon, J. Cho, C. Cheon, Y. Kwon, and Y.-K. Kim, "Planar type micromachined probe with low uncertainty at low frequencies," *Sens. Actuators, A Phys.*, vol. 139, pp. 111-117, Sep. 2007.

[30] D. Misra, M. Chabbra, B. R. Epstein, M. Mirotznik, and K. R. Foster, "Noninvasive Electrical Characterization of Materials at Microwave Frequencies Using an Open-Ended Coaxial Line: Test of an Improved Calibration Technique," *IEEE Trans. Microw. Theory Tech.*, vol. 38, no. 1, pp. 8-14, Jan. 1990.

[31] Y. Z. Wei and S. Sridhar, "Technique for measuring the frequency-dependent complex dielectric constants of liquids up to 20 GHz," *Rev. Sci. Instrum.*, vol. 60, no. 9, pp. 3041–3046, Sep. 1989.

[32] Y. Z. Wei and S. Sridhar, "Radiation-Corrected Open-Ended Coax Line Technique for Dielectric Measurements of Liquids up to 20 GHz," *IEEE*

*Trans. Microw. Theory Tech.*, vol. 39, no. 3, pp. 526–531, Mar. 1991.

[33] K. Kim, N. Kim, S.-H. Hwang, Y.-K. Kim, and Y. Kwon, "A Miniaturized Broadband Multi-State Reflectometer Integrated on a Silicon MEMS Probe for Complex Permittivity Measurement of Biological Material," *IEEE Trans. Microw. Theory Tech.*, vol. 61, no. 5, pp. 2205-2214, May 2013.

[34] J. Lane and J. Saxton, "Dielectric dispersion in pure polar liquids at very high radio frequencies," *Proc, Royal Soc.*, vol. A214, pp. 513-545, Jul. 1952.

[35] N. Kim, Y. Bang, K. Kim, C. Cheon, Y. Kim, and Y.Kwon, "A Substrate Integrated Waveguide Probe Applicable to Broadband Complex Permittivity Measurements," in *IEEE MTT-S Int. Microw. Symp. Digest*, Jun. 2011, pp. 1-4.

[36] Y. Bang, N. Kim, J. Kim, C. Cheon, Y. Kwon, and Y. Kim, "Micromachined Planar Probe using Half-SIW and Half-shielded Stripline Structure for Permittivity Measurement," in *10ᵗʰ IEEE Conference on Nanotechnology*, Aug. 2010, pp. 1121-1124.

[37] A. Nyshadham, C. L. Sibbald, and S. S. Stuchly, "Permittivity Measurements Using Open-Ended Sensors and Reference Liquid Calibration – An Uncertainty Analysis," *IEEE Trans. Microw. Theory Tech.*,

143

vol. 40, no. 2, pp. 305-314, Feb. 1992.

[38] H. Kim, S. Jung, K. Kang, J. Park, Y. Kim, and Y. Kwon, "Low-Loss Analog and Digital Micromachined Impedance Tuners at the *Ka*-Band," *IEEE Trans. Microw. Theory Tech.*, vol. 49, no. 12, pp. 2394-2400, Dec. 2001.

[39] R. Levy, "General Synthesis of Asymmetric Multi-Element Coupled-Transmission-Line Directional Couplers," *IEEE Trans. Microw. Theory Tech.*, vol. 11, no. 4, pp. 226-237, Jul. 1963.

[40] H. J. Riblet, "General Synthesis of Quarter-Wave Impedance Transformers," *IEEE Trans. Microw. Theory Tech.*, vol. 5, no. 1, pp. 36-43, Jan. 1957.

[41] H. Seidel and J. Rosen, "Multiplicity in Cascade Transmission Line Synthesis – Part I," *IEEE Trans. Microw. Theory Tech.*, vol. 13, no. 3, pp. 275-283, May. 1965.

[42] E. G. Cristal and L. Young, "Theory and Tables of Optimum Symmetrical TEM-Mode Coupled-Transmission-Line Directional Couplers," *IEEE Trans. Microw. Theory Tech.*, vol. 13, no. 5, pp. 544-558, Sep. 1965.

[43] M. Dydyk, "Accurate Design of Microstrip Directional Couplers with Capacitive Compensation," in *IEEE MTT-S Int. Microw. Symp. Digest*,

1990, pp. 581-584.

[44] Y. Kim, Y. Koh, J. Kim, S. Lee, J. Jeong, K. Seo, and Y. Kwon, "A 60 GHz Broadband Stacked FET Power Amplifier Using 130 nm Metamorphic HEMTs," *IEEE Microw. Wireless Compon. Lett.*, vol. 21, no. 6, pp. 323-325, Jun. 2011.

[45] Y. Park, Y. Kim, W. Choi, J. Woo, and Y. Kwon, "*X*-to-*K* band Broadband Watt-level Power Amplifier Using Stacked-FET Unit Cells," in *IEEE RFIC Symp. Digest*, Jun. 2011, pp. 1-4.

[46] I. Ju, Y. Kim, S. Lee, S. Song, J. Lee, C. Cheon, K.-S. Seo, and Y. Kwon, "*V*-Band Beam-Steering ASK Transmitter and Receiver Using BCB-Based System-on-Package Technology on Silicon Mother Board," *IEEE Microw. Wireless Compon. Lett.*, vol. 21, no. 11, Nov. 2011.

[47] S. Gabriel, R. W. Lau, and C. Gabriel, "The dielectric properties of biological tissues: II. Measurements in the frequency range 10 Hz to 20 GHz," *Phys. Med. Biol.*, vol. 41, pp. 2251–2269, 1996.

[48] M. A. Stuchly and S. S. Stuchly, "Coaxial Line Reflection Methods for Measuring Dielectric Properties of Biological Substances at Radio and Microwave Frequencies-A Review," *IEEE Trans. Instrum. Meas.*, vol. 29, no. 3, pp. 176-183, Sep. 1980.

[49] T. W. Athey, M. A. Stuchly, and S. S. Stuchly, "Measurement of Radio Frequency Permittivity of Biological Tissues with an Open-Ended Coaxial Line: Part I," *IEEE Trans. Microw. Theory Tech.*, vol. 30, no. 1, pp. 82-86, Jan. 1982.

[50] F. Sterzer, "Microwave Medical Devices," *IEEE Microwave Mag.*, vol. 3, no. 1, pp. 65-70, Mar. 2002

[51] J. C. Lin, "Studies of Microwaves in Medicine and Biology: From Snails to Humans," *Bioelectromagnetics*, vol. 25, no.3, pp. 146-159, Apr. 2004.

[52] G. S. Gazells, S. N. Goldberg, L. Solbiati, and T. Livraghi, "Tumor Ablation with Radio-Frequency Energy," *Radiology*, vol. 217, no. 3, pp. 633-646, Dec. 2000.

[53] Z. Gu, C. M. Rappaport, P. J. Wang, and B. A. VanderBrink, "Development and Experimental Verification of the Wide-Aperture Catheter-Based Microwave Cardiac Ablation Antenna," *IEEE Trans. Microwave Theory & Tech.*, vol. 48, no. 11, pp. 1892-1900, Nov. 2000.

[54] D. Yang, M. C. Converse, D. M. Mahvi, and J. G. Webster, "Measurement and Analysis of Tissue Temperature During Microwave Liver Ablation," *IEEE Trans. Biolmed. Eng.*, vol. 54, no. 1, pp. 150-155, Jul. 2007.

[55] M. Pavel, G. Gradinariu, and A. Stancu, "Study of the Optimum Dose of

Ferromagnetic Nanoparticles Suitable for Cancer Therapy Using MFH," *IEEE Trans. Magn.*, vol. 44, no. 11, pp. 3205-3208, Nov. 2008.

[56] H.-Y. Tseng, G.-B. Lee, C.-Y. Lee, Y.-H. Shin, and X.-Z. Lin, "Localised Heating of Tumors Utilising Injectable Magnetic Nanoparticles for Hyperthermia Cancer Therapy," *IET Nonobiotechnol.*, Vol. 3, no.2, pp. 46-54, Feb. 2009.

[57] L.-Y. Zhang, H.-C. Gu, and X.-M. Wang, "Magnetite ferrofluid with high specific absorption rate for application in hyperthermia," *J. Magn. Magn. Mater.*, vol. 311, no. 1, pp. 228-233, Apr. 2007.

[58] R. Hergt, R. Hiergeist, I. Hilger, W. A. Kaiser, Y. Lapatnikov, S. Margel, and U. Richter, "Maghemite nanoparticles with very high AC-losses for application in RF-magnetic hyperthermia," *J. Magn. Magn. Mater.*, vol. 270, no. 3, pp. 345-357, Apr. 2004.

[59] A. Iannone, R. L. Magin, T. Walczak, M. Federico, H. M. Swartz, A. Tomasi, and V. Vannini, "Blood Clearance of Dextran Magnetite Particles Determined by a Noninvasive *in Vivo* ESR Method," *Magnetic Resonance in Medicine*, vol. 22, pp. 435-442, 1991.

[60] J. Choi, J. Cha, and J.-K. Lee, "Synthesis of various magnetite nanoparticles through simple phase transformation and their shape-

dependent magnetic properties," *RSC Adv.*, vol. 3, pp. 8365-8371, 2013.

[61] Y. L. Raikher and M. I. Shliomis, "The effective field method in the orientational kinetics of magnetic fluids," *Adv. Chem. Phys.*, vol. 87, pp. 595–751, 1994.

[62] G. Bellizzi and O. M. Bucci, "A Novel Measurement Technique for the Broadband Characterization of Diluted Water Ferrofluids for Biomedical Applications," *IEEE Trans. Magn.* vol. 49, no. 6, pp. 2903-2912, Jun. 2013.

[63] Y. P. Kalmykov, W. T. Coffey, and S. V. Titov, "Analytic calculation of the longitudinal dynamic susceptibility of uniaxial superparamagnetic particles in a strong uniform DC magnetic field," *J. Magn. Magn. Mater.*, vol. 265, pp. 44–53, Sep. 2003.

[64] Y. P. Kalmykov and W. T. Coffey, "Transverse complex magnetic susceptibility of single-domain ferromagnetic particles with uniaxial anisotropy subjected to a longitudinal uniform magnetic field," *Phys. Rev. B*, vol. 56, pp. 3325–3337, Aug. 1997.

[65] P. C. Fannin, "Use of ferromagnetic resonance measurements in magnetic fluids," *J. Mol. Liq.*, vol. 114, pp. 79–87, Sep. 2004.

[66] S. Park, Y. Chung, Y. Kwon, and C. Cheon, "A Novel Two-Port Probe for Complex Permittivity and Permeability Measurement of Liquid and

Powder Type Materials," *Microwave and Optical Technology Letters*, vol. 51, no. 12, pp. 2977-2979, Dec. 2009.

[67] W. T. Joines, R. L. Jirtle, M. D. Rafal, and D. J. Schaeffer, "Microwave Power Absorption Differences between Normal and Malignant Tissue," *Radiation Oncol. Biol. Phys.*, vol. 6, pp. 681–687, 1980.

[68] G. Glöckl, R. Hergt, M. Zeisberger, S. Dutz, S. Nagel, and W. Weitschies, "The effect of field parameters, nanoparticle properties and immobilization on the specific heating power in magnetic particle hyperthermia," *J. Phys.: Condens. Matter*, vol. 18, pp. 2935–2949, 2006.

[69] Y. Alpert and E. Jerby, "Coupled Thermal-Electromagnetic Model for Microwave Heating of Temperature-Dependent Dielectric Media," *IEEE Trans. Plasma Science*, vol. 27, no. 2, pp. 555-562, Apr. 1999.

[70] W. C. Chew, *Waves and Fields in Inhomogeneous Media*, IEEE Press, New York, 1995.

[71] H. H. Pennes, "Analysis of tissue and arterial blood temperatures in resting forearm," *J. Appl. Phys.,* vol. 1, pp. 93–122, 1948.

[72] R. Vyas and M. L. Rustgi, "Green's function solution to the tissue bioheat equation," *Med. Phys.*, vol. 19, pp. 1391-1324, 1992.

[73] M. Hotta, M. Hayashi, and K. Nagata, "High Temperature Measurement of Complex Permittivity and Permeability of $Fe_3O_4$ Powders in the Frequency Range of 0.2 to 13.5 GHz," *ISIJ Int.*, vol. 51, no.3, pp. 491-497.

[74] J. E. Hill, J. D. Leitman, and J.E. Sunderland, "Thermal conductivity of various meats", *Food Tech.*, vol. 21, pp. 1143-1148, 1967.

[75] M. S. Rahman, *Food Properties Handbook* , CRC Press, New York, 1995.

[76] D. Ham and A. Hajimiri, "Concepts and Methods in Optimization of Integrated LC VCOs," *IEEE J. Solid-State Circuits*, vol. 36, no. 6, pp. 896-909, Jun. 2001.

[77] K. Kim and Y. Kwon, "A Broadband Logarithmic Power Detector in 0.13-μm CMOS," *IEEE Microw. Wireless Compon. Lett.*, vol. 23, no. 9, pp. 498-500, Sep. 2013.

[78] C. D. Holdenried, J. W. Haslett, J. G. McRory, R.D. Beards, and A. J. Bergsma, "A DC-4GHz True Logarithmic Amplifier: Theory and Implemenation," *IEEE J. Solid-State Circuits*, vol. 37, no. 10, pp. 1290–1299, Oct. 2002.

[79] H. S. Huang and J. F. Hainfeld, "Intravenous magnetic nanoparticle cancer hyperthermia," *Int. J. Nanomedicine*, vol. 8, pp. 2521-2532, 2013.

[80] C. J. Trujillo-Romero, S. García-Jimeno, A. Vera, L. Leija, and J. Estelrich, "Using nanoparticles for enhancing the focusing heating effect of an external waveguide applicator for oncology hyperthermia: evaluation in muscle and tumor phantoms," *Prog. Electromagn. Res.*, vol. 121, pp. 343-363, 2011.

[81] S. García-Jimeno, R. Ortega-Palacios, M. F. J. Cepeda-Rubio, A. Vera, L. Leija, and J. Estelrich, "Improved thermal ablation efficacy using magnetic nanoparticles: a study in tumor phantoms," *Prog. Electromagn. Res.*, vol. 128, pp. 229-248, 2012.

# 초  록

본 논문에서는 암 진단 및 치료에 적용 가능한 초소형 마이크로파 능동 집적 탐침에 대해 기술하였다. 생체 조직의 광대역 측정과 저전력 온열 치료에 적용 하기 위해 유전율 측정 회로를 평면형 동축 탐침에 집적하였고, 마이크로파 발생 회로를 어플리케이터에 집적하였다. MEMS 기술과 MMIC 기술을 적용함으로써 단일 플랫폼에 집적된 시스템으로 구현하여 집적도를 향상 시키고, 시스템을 소형화 하였다.

먼저 multi-state reflectometer를 이용하여 암 진단에 활용 가능한 복소 유전율 측정 기술에 대해 제안하였다. 2, 16 GHz에서 동작하는 광대역 reflectometer는 이중 대역 위상 고정 루프 (PLL), 임피던스 튜너, RF 전력 검출기 등의 MMIC와 MEMS 기반의 방향성 결합기, 평면형 탐침을 집적하여 구현하였다. 제작한 능동 집적 탐침 시스템을 이용하여 생체 조직과 암 조직 등의 유전율을 측정함으로써 유용함을 확인하였고, 측정된 유전율과 표준값을 비교하여 시스템의 측정 정확도를 검증하였다.

또한 저전력 마이크로파 온열 치료 요법을 위한 능동 집적 탐침을 개발하였다. MEMS 공정을 통해 제작한 평면형 실리콘 탐침에 전압 제어 발진기, 구동 증폭기, 전력 증폭기를 집적하여 능동 집적 탐침 시스템을 제작하였다. 치료를 진행하는 동안, 마이크로파의 전력을 측정할 수 있도록 전력 검출기와 방향성 결합기도 함께 집적하였다. 암, 근육 등 다양한

생체 조직을 이용한 실험의 결과로부터 *Ku* 대역의 주파수에서 저전력 마이크로파 온열 치료가 가능함을 확인하였다.

마지막으로 자성 나노입자를 이용한 온열 치료에 적용하기 위해 능동 집적 탐침을 개발하였다. 자성 나노입자가 온열 치료 요법에 미치는 영향을 분석하기 위해 전자기−열 결합 해석을 수행하였고, 이로부터 자성 나노입자의 선택도 향상을 위한 최적의 주파수를 결정하였다. 발진기와 전력 증폭기 MMIC와 이중 채널 로그 전력 검출기, 방향성 결합기를 탐침에 집적하여 시스템을 제작하였다. 이를 이용한 실험 결과로부터 능동 집적 탐침의 성능을 확인하였으며, 자성 나노입자가 저전력 및 암 특이 마이크로파 온열 치료의 효율과 선택도를 향상시키는데 유용함을 검증하였다.